UNIVERSITY OF OKLAHOMA

GRADUATE COLLEGE

MOISTURE SOURCES FOR FLASH FLOODS IN THE UNITED STATES

A DISSERTATION

SUBMITTED TO THE GRADUATE FACULTY

in partial fulfillment of the requirements for the

Degree of

DOCTOR OF PHILOSOPHY

By

JESSICA MARIE ERLINGIS LAMERS
Norman, Oklahoma
2017

MOISTURE SOURCES FOR FLASH FLOODS IN THE UNITED STATES

A DISSERTATION APPROVED FOR THE
SCHOOL OF METEOROLOGY

BY

Dr. Robert Palmer, Chair

Dr. Jonathan J. Gourley, Co-Chair

Dr. Yang Hong, Co-Chair

Dr. Jeffrey Basara

Dr. Steven Cavallo

Dr. Randall Kolar

For Mom and Dad, my first teachers

Acknowledgements

I would like to thank my advisor, Dr. Jonathan J. Gourley for hiring me for my first research assistantship as an undergraduate in 2008 and for his steadfast support and patience throughout my time as a Ph.D. student. I would also like to express my thanks to my co-advisor, Dr. Yang Hong, for always encouraging his students to be ambitious when setting goals. I would like to express my gratitude to other members of the HyDROS lab: Dr. Pierre-Emmanuel Kirstetter, for his wise advice and kindness over the years, Dr. Zac Flamig and Dr. Race Clark for their friendship and willingness to listen to my research ideas, and Dr. Humberto Vergara for the fuel any dissertation needs—COFFEE and BEER.

Thank you also to my other committee members: Dr. Robert Palmer, Dr. Jeffrey Basara, Dr. Steven Cavallo, and Dr. Randall Kolar for their insightful questions and comments that have improved the quality of this work. I'd particularly like to thank Dr. Basara for his feedback on the research design for the work presented in Chapter 4.

Thank you to my family, who has been a constant source of love and support throughout my graduate studies. I would be remiss if I did not thank the wonderful people scattered across the world that I am fortunate enough to call my friends. Thanks to Alex Zwink and Jordan Schleif (and Race and Zac again) for making me laugh, CATSSSSS, and 2for1s and to Jacob Carlin for being a wonderful listener and for his excellent eye for figure design. I'd especially like to thank Dr. Kelsey Mulder for far too many reasons to list here and Jill Hardy and Pat Hyland for opening their home to me as I bounced from elsewhere to Norman and back. I will forever be grateful for their hospitality.

Lastly, thank you to Alex Lamers for seeing me through all the ups and downs of graduate school, including all those times I was “grumpy about my scripts.” I couldn’t have done this without you.

The research in this dissertation was funded under the National Science Foundation Graduate Fellowship Program under Grant No. DGE-1102691 and under the National Oceanic and Atmospheric Administration Office of Oceanic and Atmospheric Research under NOAA-OU Cooperative Agreement #NA11OAR4320072, U.S. Department of Commerce. Some of the computing for this project was performed at the OU Supercomputing Center for Education & Research (OSCER) at OU.

Table of Contents

List of Tables

List of Figures

Abstract

This dissertation uses backward trajectories derived from North American Regional Reanalysis data for 19,253 flash flood reports published by the National Weather Service to assess the nonlocal contribution of the land surface to the moisture budget for flash flood events in the conterminous United States. The impact of land surface interactions was evaluated seasonally and for six regions of interest: the West Coast, Arizona, the Front Range, Flash Flood Alley, the Missouri Valley, and the Appalachians. Parcels were released from flooded locations and traced backward in time for 120 hours. The boundary layer height was used to determine whether moisture increases occurred within the boundary layer or not. For moisture increases occurring within the boundary layer, moisture increases were attributed to evapotranspiration from the land surface. Surface properties were recorded from an offline run of the Noah land surface model.

In general, moisture increases attributed to the land surface were associated with anomalously high surface latent heat fluxes and anomalously low sensible heat fluxes (resulting in a positive anomaly of evaporative fraction) as well as positive anomalies in top layer soil moisture. Over the ocean, uptakes were associated with positive anomalies in sea surface temperatures, the magnitude of which varies both regionally and seasonally. Major surface-based source regions of moisture for flash floods in the United States include the Gulf of Mexico, Gulf of California, and central United States, which are attributable in part to interactions between the land surface and the atmosphere.

While much of this dissertation focuses on the large-scale sources for moisture for flash flood events, storm-scale phenomena are also investigated for a precipitation event during the Integrated Precipitation and Hydrology Experiment. A case of stratiform precipitation impinging on complex terrain was examined for its microphysical properties that could result in enhanced rainfall. The data from a field experiment show coalescence processes dominate within the upslope region, suggesting enhanced updrafts aided by orographic lift sustain convection over the upslope region, leading to larger median drop diameters.

Chapter 1: Introduction

Flash floods are among the deadliest and costliest natural disasters that affect the United States and are especially difficult from a forecasting perspective as they involve both predicting where, when, and how much rainfall will occur as well as the hydrological response to that rainfall. The success of the National Weather Service's (NWS) goal of protecting lives and property also is contingent upon the human preparation for and response to a flash flood event. Seven billion-dollar flash flood events occurred in the United States during water year 2016 (October 2015-September 2016; NCEI 2017). The damages from these events surpassed $30 billion USD, and these disasters killed 173 people (Table 1).

The frequency of heavy rainfall events, one causative factor for flash flooding, has been increasing (Karl and Knight 1998; Groisman et al. 2012). A larger percentage of the conterminous United States experienced a greater-than-normal proportion of heavy one-day precipitation events in the 1990s and 2000s than in previous decades, based on a 90th percentile threshold (Gleason et al. 2008), and although climate models disagree over changes in mean precipitation in some areas, the likelihood of extreme heavy precipitation increases in extratropical regions in all models (Groisman et al. 2005).

With more extreme precipitation forcing expected, it is therefore imperative that we improve our understanding of the processes that affect the formation of flash floods, including the impact of land-surface interactions on flood-producing storms. In the past, much research has focused on the coupling between the land surface and the atmosphere at climate scales and with local grid point to grid point comparisons.

Previous work has also used backward trajectories to assess the differences in precipitation and evaporation along parcel trajectories on a case study basis or seasonally for all rainfall events, but that work has not been focused on flash floods specifically or with thousands of events as is presented in this study.

Table 1. Billion-dollar flooding disasters during water year 2016 (October 2015 – September 2016). Source: NCEI

Event	CPI-Adjusted Estimated Cost (In Billions of 2017 USD)	Deaths
South Carolina and East Coast Flooding (October 2015)	\$2.1	25
Texas Tornadoes and Midwest Flooding (December 2015)	\$2.0	50
Texas and Louisiana Flooding (March 2016)	\$2.3	5
Houston Flooding (April 2016)	\$2.7	8
West Virginia Flooding and Ohio Valley Tornadoes (June 2016)	\$1.0	23
Louisiana Flooding (August 2016)	\$10.1	13
Hurricane Matthew (October 2016)	\$10.1	49
Total	**\$30.3**	**173**

The goal of this work is to diagnose the moisture sources for flash flood events in the conterminous United States and to assess the relative contributions of moisture advection and of the interaction with the land surface. Another goal of this study is to assess the seasonality of moisture source regions and land surface contributions as a function of geographic region. The hypotheses of this dissertation are twofold: 1) if land-atmosphere interactions (specifically, evapotranspiration) have an effect on the water budget, then it is positive contribution for flash flood-producing storms (i.e., the moisture for flood events is not solely advected) and 2) that if the prior hypothesis is true, then importance of the land surface to a flash flood event varies both seasonally and regionally. Furthermore, this dissertation explores another way the land surface can affect heavy rainfall and flash flooding: a case of orographically enhanced precipitation in complex terrain, a scenario that can often trigger natural hazards such as flash flooding, landslides, and debris flows.

This manuscript is organized as follows: Chapter 2 presents an overview of the scientific literature regarding the known atmospheric mechanisms for generating heavy rainfall related to flash flooding, the interaction of the land surface and atmosphere as it relates to precipitation, and the state of flash flood forecasting and reporting in the United States. A review of using a Lagrangian perspective to investigate meteorological phenomena is also presented. Chapter 3 introduces the key datasets and models used for this study. Chapter 4 contains example cases and broader results from the moisture trajectory study, with a special emphasis on the regional and seasonal features of the flash flood climatology. Chapter 5 presents a case study into the microphysical features of a precipitation event in complex terrain, and finally, Chapter 6 presents a synthesis of the results and recommendations for future endeavors to continue this research.

Chapter 2: Literature Review

2.1 What Makes a Flash Flood?

Floods are the second deadliest weather-related hazard in the United States (Ashley and Ashley 2008), surpassed only by heat in the 30-year average from 1986-2015. The NWS Glossary (2009) defines a flash flood as

> A rapid and extreme flow of high water into a normally dry area, or a rapid water level rise in a stream or creek above a predetermined flood level, beginning within six hours of the causative event (e.g., intense rainfall, dam failure, ice jam). However, the actual time threshold may vary in different parts of the country. Ongoing flooding can intensify to flash flooding in cases where intense rainfall results in a rapid surge of rising flood waters.

While dam failures, ice jams, and other non-meteorological events can trigger flash flooding, the following section will discuss those events driven by heavy rainfall and the attendant hydrological response.

The synoptic patterns conducive for heavy rainfall are outlined in several studies. Maddox et al. (1979) examine 151 flash flood cases from 1973-1977 and classified them according to four types based on surface weather patterns: synoptic, frontal, mesohigh, and western. They identify the common characteristics of flash flood events as follows: 1) association with convective storms, 2) high surface dewpoint temperatures, 3) relatively high moisture content throughout a deep tropospheric layer, 4) weak to moderate vertical wind shear, 5) training of convective storms, 6) a weak, mid-tropospheric meso-α scale trough to trigger and focus convection, 7) proximity to a mid-tropospheric large-scale ridge, and 8) nocturnal storms. Because of the dearth of cases in the western United States in their original climatology, Maddox et al. (1980) further investigate 61 flash flood events west of 104°W, grouping them into four 500 hPa flow patterns. Expanding this analysis further, Doswell et al. (1996) present an ingredients-based methodology for forecasting heavy rainfall with the potential to produce flash flooding. Quoting C.F. Chappell, they distill forecasting heavy precipitation to the simplest concept of "the heaviest precipitation occurs where rainfall rate is the highest for the longest time." Doswell et al. (1996) explain several ingredients necessary for heavy precipitation, including those for deep moist convection: a conditionally unstable environmental lapse rate, sufficient moisture so that a level of free convection (LFC) exists, and a process to lift a parcel to its LFC. They also note that storm motion plays an important role in flash flood producing storms, with long duration systems having one or both the qualities of slow storm movement or a large area of high rainfall rates along the storm motion vector.

Brooks and Stensrud (2000) develop a climatology of heavy rainfall (≥ 25.4 mm hr^{-1}) events for the CONUS. The monthly distribution of heavy rainfall events for the CONUS is symmetric and peaks in July. Spatially, heavy rainfall events are confined to the Gulf Coast region from October through March, but extend into the areas east of the Rockies from April through September. While the analysis does show a small frequency of events in southern Arizona in July and August, there are fewer than 0.1 events per year from the Rocky Mountains westward. The authors attribute this to the sparse network of rain gauges and shorter periods of record in the western United States. Schumacher and Johnson (2006; SJ06) examine 382 rainfall events of 125 mm $(24\ h)^{-1}$ from 1999-2003 by region and also apply a varying rainfall frequency threshold to several regions east of the Rockies. By analyzing radar data for the 184 events selected by a spatially varying rainfall frequency threshold (90% of which had a corresponding flash flood report), they find that mesoscale convective systems (MCSs) are the most common producer of extreme rainfall in every region but the Southeast, where tropical cyclones or their remnants are the cause of the most extreme rainfall. SJ06 find that the onset time for heavy precipitation was after 1800 LST, peaked between 2100 and 2300 LST and dissipated by 0300 LST. Schroeder et al. (2016b) further emphasize locally anomalous precipitable water (at least 2 standard deviations above the mean) as a key ingredient for 40 summertime urban flash flood events from 1977-2014.

A contributing factor to flash flood events is the rainfall rate, which can be enhanced when precipitation processes are efficient. Doswell et al. (1996) discuss the efficiency of precipitation as one possible ingredient to forecast heavy rainfall leading to flash flooding. Formally, precipitation efficiency is defined as the ratio of the mass of water falling as precipitation to the influx of water vapor into the cloud. The precipitation efficiency can be affected by dry air entrainment, loss of small cloud particles due to wind shear, and evaporation of condensate. Collision-coalescence processes occurring below the freezing level, or warm rain processes, can be efficient producers of heavy rainfall. These processes often pose challenges to conventional observing systems (Baeck and Smith 1998, Vitale and Ryan 2013, Grams et al. 2014, Carr et al. 2016) because of underestimation of rainfall when using a convective radar-rainfall relationship. Collision-coalescence processes have been observed in flood events across the country (Pontrelli et al. 1999, Smith et al. 2000, Smith et al. 2010, Friedrich et al. 2016).

Flash flooding, however, is not solely an atmospheric phenomenon. Other definitions of flash floods exist as a function of the hydrological response of a basin. Gaume et al. (2009) develop a database of the top flash flood events for seven European regions over a 60-year time period based on the reduced peak discharge (ranging from 0.5 to 40 m^3 s^{-1} km^{-2} for their database) for basins with an area of less than 500 km^2. They define flash floods as being caused by storms that "lead to local rainfall accumulations exceeding 100 mm over a few hours and affect limited areas," although they also include storms with durations of less than 24 hours. Braud et al. (2014) use a slightly different definition based on the time to rise of the hydrograph, with flood peaks occurring in a few hours for catchments of 1-100 km^2 and within 24 hours for basins with areas greater than 1000 km^2. They apply the criterion that flash floods have a minimum specific peak discharge of 0.5 m^3 s^{-1} km^{-2}. Gourley et al. (2012) and Clark et al. (2014) use basins with a drainage area of less than 260 km^2 for flash floods in the conterminous U.S., a basin area with a nominal concentration time of 6 hours. The USGS and NWS define flood stages at gauged locations based on the impacts received (minor, moderate, major, and record) as well as an action stage when mitigation action needs to be taken (NWS 2012).

The morphologic and physiographic factors of a basin and the properties of the land surface also control a basin's response to rainfall. Costa (1987) analyzes the 12 largest floods in small basins (< 368 km^2) within the United States, all of which occurred in arid or semiarid basins, meanwhile detailing the importance of basin morphology and physiography on the hydrologic response of a basin. Exposed bedrock, thin regolith, sparse vegetation contribute to higher runoff production as there is less subsurface flow and minimal surface saturation. Basins which are short (high elongation ratios), steep (large relief), and rugged (product of relief and drainage density) are favorable for large runoff values given heavy rainfall (Costa 1987). In the study of twelve small basins, elongation ratios (ratio of basin width to length) were found to be large, but drainage densities and the number of first-order streams were less than in other flood-prone basins, leading to the conclusion that rain intensity and basin characteristics must interact favorably to produce these floods of a historic nature. Vergara et al. (2016) expand upon this work by using the basin geomorphological characteristics, precipitation, and soil properties to derive *a priori* estimates of kinematic wave routing parameters for a hydrologic model. Saharia et al. (2017) emphasize that the "flashiest" basins are characterized by small basin size and a large slope index (a measure of steepness along the main channel). The measure of basin "flashiness" described in their work will be discussed in more depth in subsequent sections.

Other characteristics that can affect runoff production are land use, soil texture, and antecedent soil moisture. In regions with a large amount of impervious area, such as cities, rainfall cannot infiltrate and becomes almost exclusively runoff. Similarly, regions where soils are saturated or nearly saturated are unable to absorb much more rainfall. The infiltration rate of a soil is a function of the soil texture. In sandy soils, water is able to infiltrate quickly, whereas that is not the case with soils with a high clay content, smaller particles, and smaller pore spaces (Hillel 1982). The depth of soil above bedrock also is a factor in the soil's total infiltration capacity, how much water can be held by the soil.

2.2 Regional Mechanisms for Heavy Rainfall and Flash Floods

In Chapter 4, the moisture sources for regions identified by Saharia et al. (2017) will be discussed. They delineate regions from 78 years of USGS streamflow observations via on a variable called *flashiness*, ϕ, defined for a given stream gauge i and a given event j as

$$\phi_{ij} = \frac{Q_{ij}^{(p)} - Q_{ij}^{(a)}}{A_i T_{ij}} \tag{1}$$

where $Q^{(p)}$ denotes peak (maximum) discharge, $Q^{(a)}$ denotes action stage discharge (as defined by the NWS), A is the basin area, and T is the flooding rise time (time between action stage discharge and peak discharge). The flashiness variable is then scaled based on the cumulative distribution function and summarized at the basin level by its median value. In addition to being similar in values of the flashiness variable developed by Saharia et al. (2017), these regions have observed climatological features that contribute to their precipitation patterns. While contributing factors to flash flood producing storms were discussed broadly in the previous section, this section discusses mechanisms specific to the flashiness regions defined in Saharia et al. (2017): the West Coast, Arizona, the Front Range, Flash Flood Alley, the Missouri Valley, and the Appalachians.

Over the West Coast of the United States, heavy rainfall and flooding occur during the cool season, and are often associated with the so-called “atmospheric river” (AR) phenomenon, a term coined by Zhu and Newell (1998) to describe long, narrow filaments of meridional water vapor transport, often with their origin in the tropics. These features account for 90% of poleward vapor transport (Ralph et al. 2004), and when the water vapor transport originates near Hawaii, this is colloquially known as a “Pineapple Express.” Ralph et al. (2004) formalize the AR characterization to describe regions of integrated water vapor (IWV) of greater than 2 cm in a plume, with a length of greater than 2000 km and a width of less than 1000 km. Moisture transport occurs within the lowest 2.25 km of the atmosphere (Ralph et al. 2006) Using Special Sensor Microwave Imager (SSM/I) data, Neiman et al. (2008) show that climatologically this phenomenon affects the southern portion of the West Coast most frequently during the winter and the northern portion of the West Coast most frequently during the summer, though both regions have their maximum rainfall totals in the cool season. During the winter, storms associated with this enhanced water vapor transport produce twice as much rain as other storms (Neiman et al. 2008) and are responsible for severe flooding. Flash flooding can occur with heavy rainfall when the plumes of high IWV impinge on both the Coastal Range and Sierra Nevada (Galewsky and Sobel 2005, Ralph et al. 2006, Smith et al. 2010).

The North American Monsoon (NAMS; also called the Mexican Monsoon) is a synoptic-scale pattern that is present over southwestern North America, and is the primary driver for much of the warm season rainfall received in Arizona (Adams and Comrie 1997). The shift of the prevailing westerlies poleward begins the development phase of the NAMS in May-June, and a mid-to-upper tropospheric anticyclone develops over North America, reaching its mature phase from July-September (Maddox 1995). The largest height increases over the Southwest are due to atmospheric heating over elevated terrain (Higgins 1997), though the height increase during the NAMS is not as large as its South Asian counterpart. While the sources of moisture for the monsoon region were once a source of debate (Rasmusson 1967, among others) NCEP-NCAR Reanalysis shows that most of the moisture below 850 hPa has its origins in the Gulf of California, and the source of moisture at 850 hPa and above is the Gulf of Mexico (Higgins 1997). Sea surface temperatures (SSTs) of greater than 29.5°C over the Gulf of California are required to simulate the NAMS (Stensrud 1995), and Mitchell (2002) show that 75% of rainfall in New Mexico and Arizona occurred with Gulf of California SSTs greater than 29°C.

Some of the most infamous flash floods have occurred along the Front Range of the Rockies: the Big Thompson Canyon flash flood (Maddox et al. 1978; Caracena et al. 1979), the Fort Collins flash flood (Petersen et al. 1999; Ogden et al. 2000), and the Great Colorado Flood of 2013 (Gochis et al. 2015). In a study of more than 300 rainfall events, Petersen et al. (1999) describe a bimodal distribution of heavy rainfall. One peak occurs in late May - early June associated with moderately intense synoptic-scale precipitation with embedded convection, and another peak occurs later in the summer from late July - early September associated with localized thunderstorms, often in the eastern foothills of the Rockies.

The region in central Texas, including the major cities of New Braunfels, San Antonio, Austin, Waco, and Dallas is colloquially known as "Flash Flood Alley." This region's proximity to moisture-rich air from the Gulf of Mexico has resulted in favorable environments for extremes in precipitation. Along the Balcones Escarpment, a region of sloping terrain that separates the coastal plains from the Edwards Plateau (Texas Hill Country), there are several physiographic features that lead to enhanced runoff production: sparse vegetation, narrow valleys, and a shallow soil depth to limestone bedrock (Baker 1975; Caran and Baker 1986). It has also been proposed that the topography leads to a slight enhancement in precipitation (Nielsen et al. 2016). Additionally, the rapid urbanization has increased the impervious surface area in the region and more people are now at risk in a region prone to some of the deadliest flooding in the United States.

The seasonal maximum in rainfall occurs over the central United States in May-June (Wang and Chen 2009). Carbone and Tuttle (2008) show that propagating precipitation episodes that originate along the Continental Divide account for 60% or all JJA rainfall in the Central United States. Self-sustaining organized convection, the mountain-plains circulation (ascending branch), and Great Plains Low Level Jet (GPLLJ) contribute to a nocturnal maximum in precipitation. Mo et al. (1997) describe enhancements in westerlies in the Eastern Pacific and western North America from 30-40°N for wet events in the Central US, with a strengthening and more northern extent of the GPLLJ. Schumacher and Johnson (2005, 2006) emphasize the importance of back-building and quasi-stationary MCSs to heavy rainfall in this region. Notable floods in the Central United States and Missouri Valley include the flooding of 1993 and the Iowa floods of 2008. Lavers and Villarini (2013) perform a hydrometeorlogical analysis of flood events from 1979-2011 and show that 50% of their study basins' annual maximum floods were associated with high Integrated Vapor Transport (IVT). Vapor transport often has origins further than the GPLLJ, and is associated with transport from the Caribbean as well, via the Caribbean LLJ (Cook and Vizy 2010). Sea surface salinity anomalies in the subtropical North Atlantic, indicating enhanced evaporation and vapor flux away from the region, significantly correlate with precipitation over the Midwest (Li at al. 2016) This region has also been identified as a region where non-local soil moisture anomalies (DeAngelis et al. 2010, Kustu et al. 2011) and anomalous evaporative moisture in the Caribbean Sea (Dirmeyer and Kinter 2010) are correlated with heavy rainfall and flood events.

Along the Appalachian Mountains, there is a seasonal maximum of thunderstorms in mid-July. A local minimum in lightning activity (a proxy for convective activity) occurs over the highest terrain in the Appalachians but local maxima occur on both the western and eastern slopes (Smith et al. 2011). Smith et al. (2011) also note that some of the most historic peaks in discharge values occurred with terrain-locked thunderstorms. Orographic enhancement of precipitation (Hicks et al. 2005) is also a factor when considering flood producing storms in the region. This region is also somewhat unique in the role that tropical cyclones play in its water budget. The stretch along the Appalachians from North Carolina to Vermont boasts the highest ratio of tropical cyclone events to flood peaks (Villarini et al. 2014), and tropical cyclones have the largest effect on the tails of flood peak distributions (Villarini and Smith 2010). Tropical cyclones impinging on the Appalachian Mountains have produced hazards such as flooding and landslides in Fran (Sturdevant-Rees et al. 2001), Fay (Tao and Barros 2013), Frances, and Ivan (Wooten et al 2008) among others.

2.3 Land-Atmosphere Interactions and Precipitation

The land surface is linked to the atmosphere through exchanges of energy, carbon, and moisture that occur within the planetary boundary layer (PBL), and such linkages have been studied from scales ranging from the microscale to the climate scale. At climate scales, modeling studies delineate regions where feedback mechanisms between soil moisture availability and precipitation occur (Koster et al. 2004; Luo et al. 2007), one of which is the Southern Great Plains (SGP) of the United States. Such studies, however, oftentimes limit their focus to precipitation recycling at the grid point scale.

Surface fluxes can affect precipitation patterns by modulating boundary layer temperature and moisture profiles (Ek and Mahrt 1994; Findell and Eltahir 2003). Such interactions have varying effects and can induce positive and negative feedback loops. For example, evaporation can moisten the boundary layer sufficiently, lowering the lifting condensation level (LCL) so that clouds form, precipitation occurs, and the cycle repeats itself. Another possibility is that large sensible heat fluxes from dry soils can cause an increase in parcel buoyancy, allowing parcels to rise sufficiently to reach their level of free convection (LFC).

Heterogeneities in land cover type and attendant surface properties can induce dynamic circulations at the mesoscale and microscale, leading to preferential areas for cloud formation (Segal and Arritt 1992; Mahrt et al. 1994; Lynn et al. 1998; Ek and Holtslag 2004; Pielke 2001). Furthermore, land surface cover and/or states can have an effect on the properties of downstream precipitation (Mo et al. 1997; Erlingis and Barros 2014) by modifying an air mass through energy and moisture exchanges with the surface.

2.4 Using Trajectories to Study Atmospheric Phenomena

Previous studies have used trajectories to investigate atmospheric phenomena at both climate and event scales. The following section will describe some of the methods used for water budget studies, specifically. At the climate scale, Stohl and James (2004, 2005) use the Lagrangian particle dispersion model FLEXPART to study the global distribution of annual mean freshwater surface flux by assessing residual of evapotranspiration and precipitation. Nieto et al. (2006) adopt their methodology and use European Center for Medium Range Forecasts (ECMWF) data and the FLEXPART model (Stohl and James 2004, 2005) to diagnose moisture sources for the Sahel region. Drumond et al. (2008) apply the same methodology for Central Brazil and the La Plata basin. Sun and Wang (2014) also use this methodology to identify moisture sources for grasslands in China. Sorí (2015) applies this method to assessing the contribution of the Atlantic warm pool to the hydrological budget of Central and North America. Arnault et al. (2016) and Wei et al. (2016) use a tracer method (called e-tagging) in a forward model to assess the precipitation recycling ratio and the atmospheric water vapor residence time, respectively.

If liquid water and ice are ignored, then the water budget in an atmospheric column is expressed in an Eulerian framework as (Trenberth and Guillemot 1998)

$$\frac{\partial w}{\partial t} + \nabla \cdot \frac{1}{g} \int_0^{p_s} q\mathbf{v}\, dp = E - P \tag{2}$$

where E and P are evaporation and precipitation rates per unit area, E-P is the surface freshwater flux, t is time, g is gravitational acceleration, $\boldsymbol{v}$ is the horizontal wind, q is specific humidity, p_{s} is the surface pressure, and w is the precipitable water defined as

$$w = \frac{1}{g} \int_0^{p_s} q\, dp \tag{3}$$

Following this framework, the aforementioned studies follow a parcel's trajectory (Stohl and James 2004)

$$\frac{d\mathbf{x}}{dt} = \mathbf{U}\left[\mathbf{x}(t)\right] \tag{4}$$

where ***x*** is the particle's position and ***U[x(t)]*** is the particle's three-dimensional velocity. If specific humidity, *q*, is interpolated to the parcel's trajectory, then the net rate of change of the water vapor content of the particle (in a Lagrangian framework) is

$$e - p = m\frac{dq}{dt} \tag{5}$$

where the *e* and *p* are rates of moisture increase and decrease along the trajectory and m is the mass of the air parcel. By summing the net changes of each parcel at each grid point, the total surface freshwater flux is approximated over an area *A* as

$$E - P \approx \frac{\sum_{k=1}^{K}(e-p)}{A} \tag{6}$$

where *K* is the total number of particles in *A*. The quantity *E-P* can then be averaged over time to avoid effects of cloud formation, which would affect the estimates of averages of *E* or *P* individually (Stohl and James 2004).

Dirmeyer and Brubaker (1999), Brubaker et al. (2001), and Dirmeyer and Kinter (2010) apply a different method to analyzing water budgets using hourly observed precipitation data, reanalysis data, and a quasi-isentropic backward trajectory algorithm. The parcel's height is determined by its potential temperature, and winds are used for advection. They launch parcels backward in time from grid boxes where precipitation occurred at a rate proportional to the precipitation rate and distribute the parcels vertically based on a water-mass-weighted random sample. When tracing a parcel backwards in time, a fraction of the water vapor in the parcel is assumed to have evaporated from the grid box at the parcel's position, according to

$$R_{i,k}(x,y,t)=\frac{E(x,y,t)}{PW_i} \tag{7}$$

where $R_{i,k}(x,y)$ is the contribution of the grid box (x,y) to the precipitable water (PW) at time t for the precipitation event at a grid box i for a given parcel k. For a grid area A composed of n grid squares, and with m parcels launched from area A, the water mass contribution of evaporation of grid box (x,y) to precipitation in area A is

$$E_A(x,y)=\sum_{i=1}^{n}\sum_{k=1}^{m}\sum_{t=0}^{t=t_f}R_{i,k}(x,y,t) \tag{8}$$

the recycling ratio, S, can then be computed as

$$S=\frac{\sum_{B}E_A(x,y)}{P_A} \tag{9}$$

provided areas A and B are equal. Dirmeyer and Brubaker (1999) examine the evaporative moisture sources for the drought of 1988 and the flood of 1993 for the Mississippi-Missouri basin. Brubaker et al. (2001) extend this work by developing a 36-year climatology of evaporative moisture sources for the Mississippi River Basin. Dirmeyer and Kinter (2010) apply this method to flooding over the U.S. Midwest by pentads from 16 April – 3 August in years 1979-2004, with a focus on MMJ.

Noting that the works by Dirmeyer and Brubaker do not use kinematic trajectories, Sodemann et al. (2008) expand upon the work by Stohl and James (2004, 2005) in order to assess the moisture sources for precipitation in Greenland under different phases of the North Atlantic Oscillation, not only by their geographical locations, but by their locations within an atmospheric column. They seek to ascribe the increases in parcel moisture to the PBL or to outside of the PBL. The application of this methodology is discussed further in Chapter 4.

In a review paper, Stohl (1998) summarizes various sources of error that occur when using trajectories to study atmospheric phenomena. The main sources of errors that are covered include 1) truncation errors due to the finite difference schemes in computing the trajectories, 2) interpolation errors in both space and time, 3) errors resulting from assumptions regarding the nature of the vertical wind (e.g. using the continuity equation to compute w, turbulent mixing in the PBL), 4) wind field errors in the form of analysis or forecast errors and 5) errors in starting position and amplification errors. The error in trajectories can be as much as 20-30% of the total travel distance. Draxler (2003) seeks to quantify test the sensitivity of the Hybrid Single-Particle Lagrangian Integrated Trajectory (HYSPLIT) model (Stein et al. 2015) to perturbations in particle positions by perturbing members +/- one grid point in the horizontal, and +/- 250 m in the vertical, where each member was assumed to have equal probability. The trajectory ensemble approach accounts for 41-47% of the variance in the measurement data.

Additional uses of trajectories to study atmospheric phenomena are wide-ranging and include the study of snow events (Fuhrmann and Konrad 2013), supercells, and tornadoes (Wakimoto et al. 1998, Marquis et al. 2016, Betten et al. 2017), etc.

Chapter 3: Data and Model Descriptions

3.1 North American Regional Reanalysis (NARR)

North American Regional Reanalysis (NARR; Mesinger et al. 2006) data are produced at 3-hourly intervals at 32 km grid spacing with 45 vertical levels. NARR is produced using the NCEP-DOE Global Reanalysis and the NCEP Eta Model and its data assimilation system. It is available from 1979-present at the National Center for Atmospheric Research (NCAR; http://rda.ucar.edu/datasets/ds608.0/). NARR uses lateral boundary conditions from NCEP-DOE GR2, the Noah land surface model, and a 3D-VAR data assimilation system (EDAS; Rogers et al. 2001), including the assimilation of observed precipitation.

3.2 High-Resolution Land Data Assimilation System (HRLDAS)

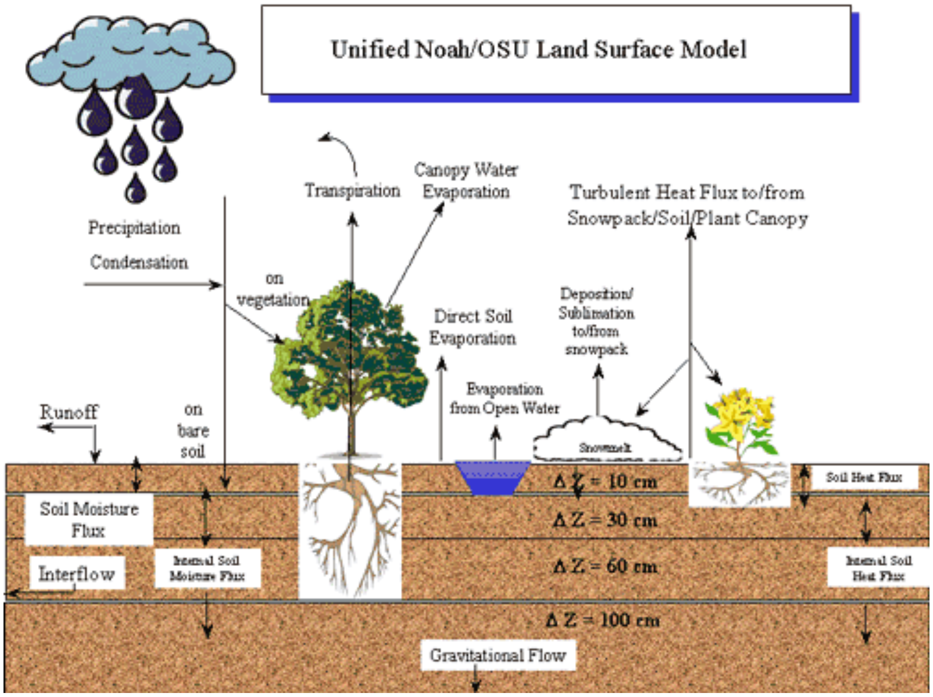

Figure 1. Schematic of processes in the Noah LSM. Source: http://www.ral.ucar.edu/research/land/technology/lsm/mm5_1-500.gif

The High-Resolution Land Data Assimilation System (HRLDAS; Chen et al. 2007) was developed at the National Center for Atmospheric Research (NCAR) to run the Noah Land Surface Model (Noah LSM), which evolved from the Oregon State University model (Pan and Mahrt 1987, Chen and Dudhia 2001, Ek et al. 2003) separately, or uncoupled, from the atmospheric component of the Weather Research and Forecasting Model (WRF; Skamarock et al. 2008). Oftentimes, the purpose of this is to spin up the soil state variables (temperature, moisture, etc.) at the same grid spacing as a pending WRF simulation. The WRF model input file is used in HRLDAS initialization to ensure that the HRLDAS run and the WRF runs share the same grid spacing, nesting, and land and soil physical properties. The result of the HRLDAS simulation can then be used to overwrite the WRF initialization file generated by the WRF preprocessor. HRLDAS output fields are shown in Table 2. A schematic of the Noah LSM is shown in Figure 1. A brief description of the relevant model physics for surface energy exchanges and soil moisture and temperature in Noah follows. More detail is provided for other processes in the publications referenced throughout this section.

Table 2. HRLDAS output fields

Variable Name	Units	Variable Name	Units	Variable Name	Units	Variable Name	Units
Dominant Vegetation Category	Category	Accumulated Interflow Runoff	mm	Accumulated Evaporation of Snow	mm	Downward Longwave Radiation Flux	Wm^{-2}
Dominant Soil Category	Category	Accumulated Evaporation from Surface	mm	Accumulated Canopy Drip	mm	Radiation Forcing at the Surface	Wm^{-2}
Skin Temperature	K	Evapotranspiration	mm	Accumulated Dewfall	mm	Leaf Area Index	--
Canopy Water Content	mm	Accumulated Canopy Evaporation	mm	Snow Depth	m	Snow Age	s
Soil Temperature	K	Accumulated Direct Soil Evaporation	mm	Green Vegetation Fraction	Fraction	Background Emissivity	--
Volumetric Soil Moisture	m^3m^{-3}	Accumulated Plant Transpiration	mm	Roughness Length	m	Maximum Albedo Over Deep Snow	Fraction
Liquid Volumetric Soil Moisture	m^3m^{-3}	Albedo	Fraction	Upward Surface Sensible Heat Flux	Wm^{-2}	Residual of Surface Energy Balance	Wm^{-2}
Total Column Soil Moisture	mm	Water Equivalent Snow Depth	m	Upward Surface Latent Heat Flux	Wm^{-2}	Heat Exchange Coefficient	--
Accumulated Surface Runoff	mm	Accumulated Precipitation	mm	Ground Heat Flux at Surface	Wm^{-2}		
Accumulated Underground Runoff	mm	Accumulated Snow Melt	mm	Downward Shortwave Radiation Flux	Wm^{-2}		

3.2.1 Soil Temperature

The diffusion equation for soil temperature is given by

$$C(\Theta)\frac{\partial T}{\partial t}=\frac{\partial}{\partial z}\left[K_T(\Theta)\frac{\partial T}{\partial z}\right] \tag{10}$$

where C is the volumetric heat capacity (J m^{-3} K^{-1}), and K_t is thermal conductivity (W m^{-1} K^{-1}). Both are functions of volumetric soil water content, Θ (Pan and Mahrt 1987). The heat capacity of the composite soil is defined as (Chen and Dudhia 2001)

$$C=\Theta C_{water}+(1-\Theta_s)C_{soil}+(\Theta_s-\Theta)C_{air} \tag{11}$$

where Θ_s is the maximum soil water, or the porosity. The volumetric heat capacities are C_{water} = 4.2 x 10^6 J m^{-3} K^{-1}, C_{soil}=1.26 x 10^6 J m^{-3} K^{-1}, and C_{air} = 1004 J m^{-3} K^{-1}. At the *i*th soil layer, the layer integrated form of Equation 11 is

$$\Delta z_i C_i\frac{\partial T_i}{\partial t}=\left(K_t\frac{\partial T}{\partial z}\right)_{z_{i+1}}-\left(K_t\frac{\partial T}{\partial z}\right)_{z_i} \tag{12}$$

3.2.2 Soil Moisture

The prognostic equation function for volumetric soil moisture content (Θ) is given by the diffusive form of Richard's equation (Chen et al. 1996)

$$\frac{\partial\Theta}{\partial t}=\frac{\partial}{\partial z}\left(D\frac{\partial\Theta}{\partial z}\right)+\frac{\partial K}{\partial z}+F_\Theta \tag{13}$$

where both the soil water diffusivity, D, and the hydraulic conductivity, K, are functions of Θ. The equation is derived from Darcy's law for a rigid, isotropic, homogeneous, and one-dimensional vertical flow domain (Hanks and Ashcroft 1986). The F_Θ term represents sources and sinks for soil water (precipitation and evaporation, etc.). Soil water diffusivity, D is given by

$$D = K(\Theta)\frac{\partial \Psi}{\partial \Theta} \tag{14}$$

where Ψ is the soil water tension function given by (Cosby et al. 1984)

$$\Psi(\Theta) = \Psi_s / (\Theta / \Theta_s)^b \tag{15}$$

and K is given by

$$K(\Theta) = K_s(\Theta / \Theta_s)^{2b+3} \tag{16}$$

The parameter b is a curve fitting parameter, and K_s, Ψ_s, Θ_s, and b all depend on soil type. It should be noted that hydraulic conductivity and soil water diffusivity can vary by several orders of magnitude, even with just a small change in soil moisture.

3.2.3 Energy Balance

In order to obtain surface temperature and moisture and calculate the surface fluxes, the surface energy balance must be solved first. The surface energy balance is given by (Ek and Mahrt 1991)

$$(1-\alpha)S\downarrow + L\downarrow - \varepsilon\sigma T_s^4 = H' + L_v E_p + G \tag{17}$$

where α is the surface albedo, $S\downarrow$ is the incoming solar radiation at the surface. $L\downarrow$ is the downward longwave radiation, $\varepsilon\sigma T_s^4$ is the upward terrestrial radiation, and T_s is the surface temperature. On the right-hand side of the equation, H' is the sensible heat flux L_vE_p is the potential evaporation, and G is the soil heat flux. The surface emissivity ε is assumed to be 1. $\sigma = 5.67\text{x}10^{-8}$ W m^{-2} K^{-4} is the Stefan-Boltzmann constant, and $L_v = 2.5 \times 10^6$ J kg^{-1} is the latent heat of vaporization. In the model, the outward longwave radiation is linearized as (Ek 2005)

$$\sigma T_s^4 \approx \sigma T_a^4\left[1 + 4\left(\frac{T_s - T_a}{T_a}\right)\right] \tag{18}$$

where T_a is the temperature at the first model level in the atmosphere.

T_s and H' in the Equation 17 are for a saturated surface, and the sensible heat flux, based on the potential evaporation, is given by (Ek and Mahrt 1991)

$$\begin{aligned} H' &= \rho c_p C_h U(\theta_s - \theta_a) \\ &= \rho c_p C_h U[(\theta_s - T_a) - (\theta_a - T_a)] \end{aligned} \tag{19}$$

where ρ is the air density, c_p is specific heat C_h is the exchange coefficient θ_s is the surface potential temperature, and θ_a, T_a, and U are the potential temperature, temperature, and wind speed at the first model level. To compute potential evaporation, H' is calculated using values from the previous model time step.

Defining F_n as (Ek 2005)

$$F_n = (1-\alpha)S\downarrow + L\downarrow - \varepsilon\sigma T_a^4 - G \tag{20}$$

and substituting into Equation 17 yields

$$F_n - 4\sigma T_a^4 \left(\frac{T_s - T_a}{T_a} \right) = H' + L_v E_p \tag{21}$$

Further substituting Equation 19 into Equation 21 and assuming $\theta_s = T_s$ gives

$$F_n - 4\sigma T_a^4 \left(\frac{T_s - T_a}{T_a} \right) = \rho c_p C_h U[(T_s - T_a) - (\theta_a - T_a)] + L_v E_p \tag{22}$$

Potential evapotranspiration is given by (Ek 2005)

$$\begin{aligned} L_v E_p &= \rho c_p C_q U(q_{s,sat} - q_a) \\ &= \rho c_p C_h U\left[\frac{dq_s}{dT}(T_s - T_a) + (q_{a,sat} - q_a) \right] \end{aligned} \tag{23}$$

It is assumed here that the exchange coefficients for heat C_h and moisture C_q are equal. $\frac{dq_s}{dT}$ is the slope of the saturation specific humidity with temperature, $q_{s,sat}$ is the surface saturation specific humidity $q_{a,sat}$, q_a are the saturation specific humidity and the actual specific humidity at the first model level. Rearranging to solve for the temperatures gives

$$T_s - T_a = \left[\frac{L_v E_p}{\rho L_v C_h} - (q_{a,sat} - q_a) \right] \left(\frac{dq_s}{dT} \right)^{-1} \tag{24}$$

that when substituted into Equation 23 in order to solve for potential evaporation, yields

$$L_v E_p = \rho c_p C_h U \left(\frac{\Delta \left[\frac{F_n}{\rho c_p C_h U} + (\theta_a - T_a) \right] + A(r+1)}{\Delta + r + 1} \right) \tag{25}$$

where

$$\Delta = \frac{dq_s}{dT} \frac{L_v}{c_p} \tag{26}$$

$$A = \frac{L_v}{c_p} (q_{a,sat} - q_a) \tag{27}$$

$$r = \frac{4 \sigma T_a^4 R_d}{p_s c_p C_h U} \tag{28}$$

The above are for cases where $\theta_s = T_s$. The more general form of Equation 25 is (Ek 2005)

$$L_v E_p = \rho c_p C_h U \left(\frac{\Delta \left[\frac{F_n}{\rho c_p C_h U} + (\theta_a - T_a) \right] + A(r+1) + (A - \Delta T_a)\delta_\theta}{\Delta + r + 1 + \delta_\theta} \right) \tag{29}$$

where

$$\delta_\theta = \left(\frac{p_{00}}{p_s} \right)^\kappa - 1 \tag{30}$$

and p_{00}=1000 hPa, p_s is surface pressure, and $\kappa=R_d/c_p$.

3.2.4 Soil Heat Flux

Soil heat flux G is given by (Ek 2005)

$$G = -\lambda_T \frac{\partial T_{s_1}}{\partial z} \tag{31}$$

where λ_T is the soil thermal conductivity and $\frac{\partial T_{s_1}}{\partial z}$ is the soil temperature gradient in the topmost soil layer.

3.2.5 Evaporation

Total evaporation is given by (Pan and Mahrt 1987)

$$E = E_{dir} + E_c + E_t \tag{32}$$

where E_{dir} is direct soil evaporation, E_c is evaporation of precipitation intercepted by the canopy, and E_t is transpiration. E cannot exceed potential evaporation.

Direct evaporation from the soil is given by Chen and Dudhia (2001)

$$E_{dir} = (1 - \sigma_f)\beta E_p \tag{33}$$

where E_p is the potential evapotranspiration, σ_f is the green vegetation fraction, and β is given by

$$\beta = \frac{\Theta_1 - \Theta_w}{\Theta_{ref} - \Theta_w} \tag{34}$$

where Θ_w is the wilting point and Θ_{ref} is the field capacity. Ek at al. (2003) modifies this further by the exponentiation of the β parameter a nonlinear function to account for large gradients in near surface soil moisture.

The canopy evaporation is given by Chen and Dudhia (2001)

$$E_c = \sigma_f E_p \left(\frac{W_c}{S} \right)^n \tag{35}$$

where W_c is the intercepted canopy water content, S is the maximum canopy capacity (chosen to be 0.5 in the model), and n=0.5. The water budget for the canopy is

$$\frac{\partial W_c}{\partial t} = \sigma_f P - D - E_c \tag{36}$$

where P is the total precipitation. If $W_c > S$, then the excess precipitation reaches the ground as drip, D. Canopy evapotranspiration is then given by

$$E_t = \sigma_f E_p B_c \left[1 - \left(\frac{W_c}{S} \right)^n \right] \tag{37}$$

where B is a function of canopy resistance given by

$$B_c = \frac{1 + \frac{\Delta}{R_r}}{1 + R_c C_h + \frac{\Delta}{R_r}} \tag{38}$$

where C_h is the heat exchange coefficient, Δ depends on the slope of relative humidity (Equation 26); R_r is defined as (Mahrt and Ek 1991)

$$R_r = \frac{4\sigma T_0^4 R_d}{p_{sfc} C_h c_p} + 1 \tag{39}$$

R_c is the canopy resistance, calculated as

$$R_c = \frac{R_{c\min}}{LAI F_1 F_2 F_3 F_4} \tag{40}$$

$$F_1 = \frac{R_{c\min} / R_{c\max} + f}{1 + f} \tag{41}$$

$$f = 0.55\frac{R_g}{R_{g1}}\frac{2}{LAI} \tag{42}$$

$$F_2 = \frac{1}{1 + h_s[q_s(T_a) - q_a]} \tag{43}$$

$$F_3 = 1 - 0.0016(T_{ref} - T_a)^2 \tag{44}$$

$$F_4 = \sum_{i=1}^{3} \frac{\left(\Theta_i - \Theta_w\right)d_{z_1}}{(\Theta_{ref} - \Theta_w)(d_{z_1} + d_{z_2})} \tag{45}$$

The F functions are bounded by 0 and 1 and represent the effects of solar radiation, vapor pressure deficit, air temperature, and soil moisture, respectively (Chen and Dudhia 2001). R_{cmin} is the minimum stomatal resistance, and R_{cmax} is the cuticular resistance of the leaves, set to 5000 s m^{-1} (Dickinson et al. 1993). LAI is the leaf area index). T_{ref} = 298K as in (Noilhan and Planton 1989).

3.2.6 Surface Temperature

In order to define the surface skin temperature the surface energy balance (Equation 17) is used. Now, actual evaporation is used instead of potential evaporation, where β is a multiplicative factor to account for the difference between potential and actual evaporation. The surface energy balance is then (Ek and Mahrt 1991 and Ek 2005)

$$(1-\alpha)S\downarrow + L\downarrow - \varepsilon\sigma T_s^4 = G + H + \beta L_v E_p \tag{46}$$

Using the linearized surface energy balance as before

$$(1-\alpha)S\downarrow + L\downarrow - 4\sigma T_a^4 - 4\sigma T_a^4\left(\frac{T_s - T_a}{T_a}\right) = G + \rho c_p C_h U[(T_s - T_a) - (\theta_a - T_a)] + \beta L_v E_p \tag{47}$$

Using the equation for soil heat flux and solving for T_s

$$T_s = \frac{\Delta z \rho c_p C_h U[T_a(r+1) + (\Theta_a - T_a)] + \Delta z(F - \sigma T_a^4 - \beta L_v E_p) + \lambda_T T_{s_1}}{\Delta z \rho c_p C_h U(r+1) + \lambda_T} \tag{48}$$

where F is defined as, and *r* is defined in Equation 28 The above equation applies for cases where $\theta_s = T_s$. When $\theta_s \neq T_s$, Equation 48 becomes

$$T_s = \frac{\Delta z \rho c_p C_h U[T_a(r+1) + (\Theta_a - T_a)] + \Delta z(F - \sigma T_a^4 - \beta L_v E_p) + \lambda_T T_{s_1}}{\Delta z \rho c_p C_h U(r+1+\delta_0) + \lambda_T} \tag{49}$$

where δ_0 is given by Equation 30. After updating the soil moisture content, and soil and surface temperatures, the soil heat flux and sensible heat fluxes are then updated.

3.2.7 Surface Exchange Coefficients

The surface exchange coefficient for heat and moisture is given by Ek and Mahrt (1991)

$$C_h = \frac{k^2}{R} |\mathbf{v}_0| \frac{F_2}{\ln\left(\frac{z}{z_0}\right) \ln\left(\frac{z}{z_{0H}}\right)} \tag{50}$$

where *k* is the nondimensional von Kármán constant (0.4). *R*, the ratio of the drag coefficients for momentum and heat in the neutral limit, is estimated to be 1.0. $|\boldsymbol{v}_0|$ is the wind speed at the first model level, *z* is the height of the first model level above the surface, and z_{0H} is the roughness length for heat. F_2 is defined as

$$F_2 = \begin{cases} e^{-aRi_B} & \textit{stable} \\ 1 - \dfrac{15 Ri_B}{1 + 7.5\left[10 \dfrac{k^2}{\ln\left(\frac{z}{z_{0M}}\right)\ln\left(\frac{z}{z_{0H}}\right)}\right]\left(-Ri_B \dfrac{z}{z_{0M}}\right)^{1/2}} & \textit{unstable} \end{cases} \tag{51}$$

where a = 1.0, z_{0M} is the roughness length for momentum, and Ri_B is the bulk Richardson number for the surface layer, defined as

$$Ri_B = \frac{gz(\theta_{0v} - \theta_{sv})}{\theta_{0v}\left|\mathbf{v}_0\right|^2} \tag{52}$$

θ_{0v} is the virtual potential temperature of the air at the first model level and θ_{sv} is the surface temperature from the surface energy balance.

3.2.8 Surface Hydrology

Surface runoff and infiltration is calculated by the Simple Water Balance (SWB) model (Schaake et al. 1996). The SWB is a two-reservoir hydrological model, with the top layer consisting of the vegetation canopy and the soil surface and the lower layer containing the root zone and the groundwater system. Runoff R is defined as the excess precipitation P_d not infiltrated into the soil (Chen and Dudhia 2001).

$$R = P_d - I_{\max} \tag{53}$$

where the maximum infiltration I_{max} is given by

$$I_{\max} = P_d \frac{D_x[1 - \exp(-kdt\delta_i)]}{P_d + D_x[1 - \exp(-kdt\delta_i)]} \tag{54}$$

$$D_x = \sum_{i=1}^{4} \Delta Z_i(\Theta_s - \Theta_i) \tag{55}$$

$$kdt = kdt_{ref} \frac{K_s}{K_{ref}} \tag{56}$$

where δ_i is the conversion of the current time step from seconds into daily values, K_s is the saturated hydraulic conductivity, and kdt_{ref} = 3.0 and K_{ref}=2 x 10^{-6} m s^{-1}.

Chapter 4: Moisture Trajectories for Flash Flood Events

4.1 Methodology

Because there are multiple sources of flash flood information spread across agencies in the United States, Gourley et al. (2013) developed a unified flash flood database, which includes reports from NWS *Storm Data,* USGS reports based on streamflow data that exceed the NWS defined action stage for each gauge, and reports solicited from the public during the Severe Hazards Analysis and Verification Experiment (SHAVE) during the summers of 2008-2010. The *Storm Data* flash flood reports from the 2007-2013 archive were used in this study because of the change in the reporting process that went into effect in 2007. After October 2007, the NWS began issuing flash flooding reports as polygons of affected areas, while previously, reports had been recorded by county. Each polygon was distilled to its centroid for the purposes of this study.

Because of the challenge in producing a NWP forecast (let alone a multi-day forecast) with accuracy in terms of the spatial location, magnitude, and timing of rainfall (Wernli et al. 2008, Roberts et al. 2009, Vincendon et al. 2011, Hardy et al. 2016), which is essential when assessing the local and nonlocal impacts of the land surface, reanalysis data were used instead of modeling individual events. The model domain is a subset of the NARR domain. The grid is 1126 x 699 pixels with 6 km horizontal grid spacing, chosen based on computational constraints. Land use, topography, and soil texture are shown in Figure 2, Figure 3, and Figure 4, respectively.

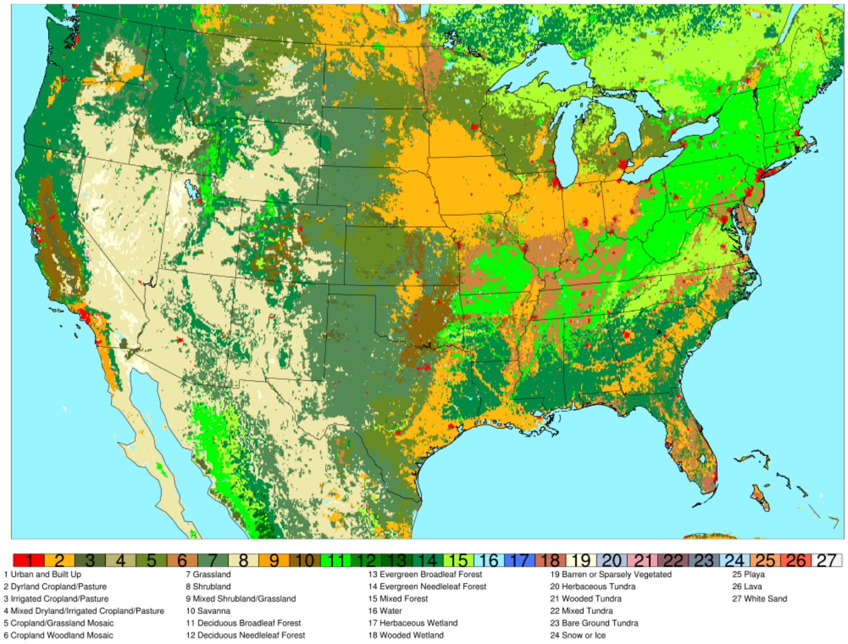

Figure 2. Domain dominant land cover.

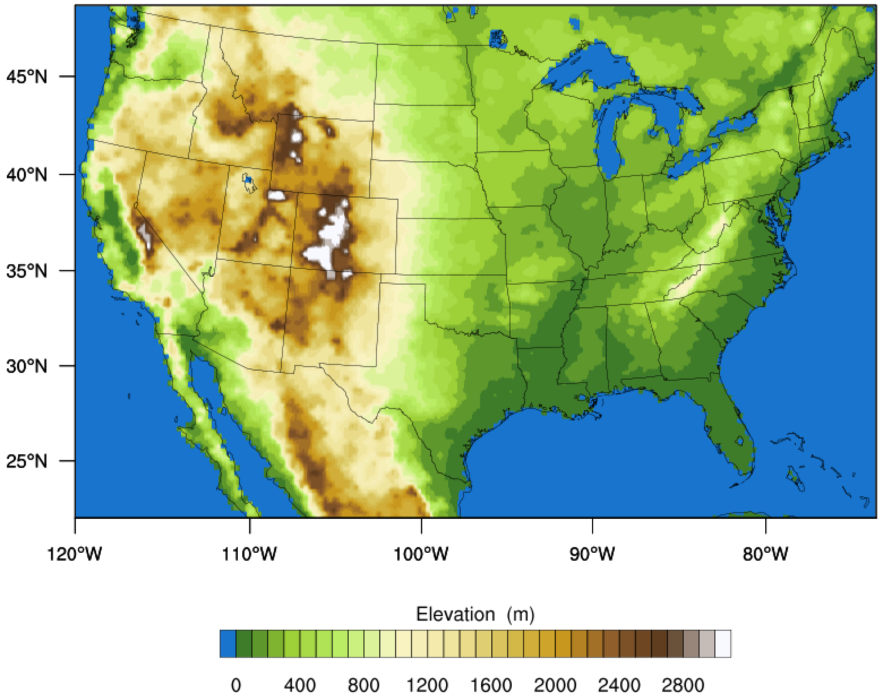

Figure 3. Domain topography.

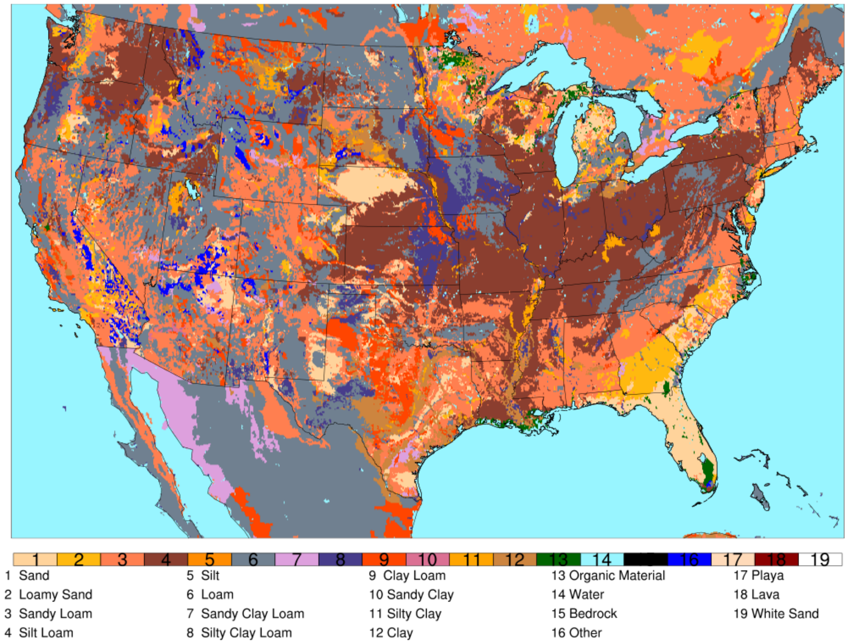

Figure 4. Domain dominant soil texture.

Land surface properties were initialized with USGS land use data and STATSGO soil texture data, and four soil layers were used: 0-10 cm, 10-40 cm, 40-100 cm, and 100-200 cm below ground. A 12-year retrospective run (2002-2013) was conducted using HRLDAS forced by NARR data on the model domain shown, so that flash flood reports in 2007 and beyond had a minimum of ~5 years of soil state spin up. Nemunaitis (2014) showed that five years of spin up was necessary to reach a rough equilibrium state in soil moisture near Oklahoma City, though soil temperature spun up in about two years. An example of the difference in soil states between using NARR data alone (cold start) and using the HRLDAS simulation is shown in Figure 5. NARR forcing data were interpolated to hourly time steps, and the integration time step used was 30 minutes. Model fields were output every 3 hours at 00, 03, 06, 09, 12, 15, 18, and 21 Universal Time Coordinated (UTC) from 2007-2013. NARR gridded binary

(GRIB) data were interpolated to the same grid as the HRLDAS simulation by using the WRF Preprocessing System version 3.4.1 (WPS; Skamarock et al. 2008).

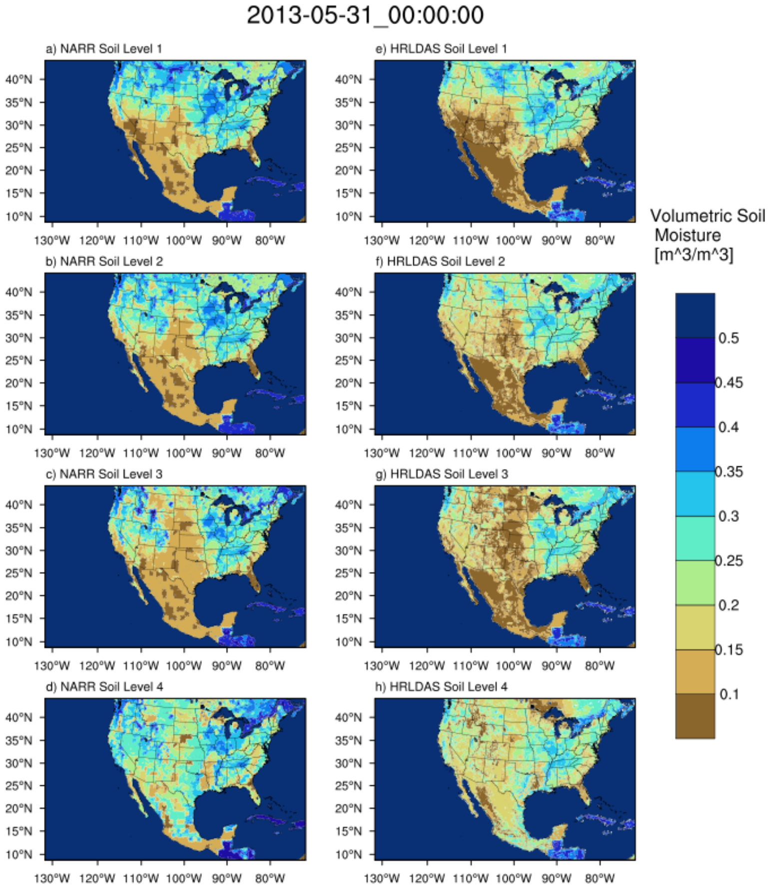

Figure 5. Volumetric soil moisture (m^3/m^3) for 00:00 UTC on 31 May 2013 for NARR (left) and HRLDAS (right). Layer 1 is the 0-10 cm below ground; Layer 2 is 10-40 cm below ground; Layer 3 is 40 -100 cm below ground, and Layer 4 is 100 - 200 cm below ground.

For each event, in order to account for spatial uncertainty in the trajectory calculations, a box of 11 x 11 grid cells was generated with the centroid of the flash flood report at the center of the grid. The nearest 3-hour time step was used to initialize the parcels. Parcels were spaced every 30 hPa in the vertical from 950 hPa to 470 hPa, and backward trajectories were computed for 120 hours with an integration time step of 30 minutes. The aforementioned spacing was chosen so as to concentrate parcels in the levels of the atmosphere with the bulk of the moisture content. The parcel positions were recorded every 3 hours to coincide with NARR and HRLDAS availability. A map of the domain and schematic of the setup for each event is shown in Figure 6. Trajectory calculations were performed using the Read/Interpolate/Plot (RIP; Stoelinga 2009) software program also developed at National Center for Atmospheric Research (NCAR) and the University of Washington. RIP trajectories have recently been used for a variety of applications (e.g. Beck and Weiss 2013, Smart and Browning 2014; Tilev-Tanriover and Kahraman 2015; Slater et al. 2015; Hardy et al. 2017). Although the atmospheric forcing data were only available at 3-hour intervals, parcel positions were computed every 30 minutes to improve accuracy, as recommended by the RIP developers.

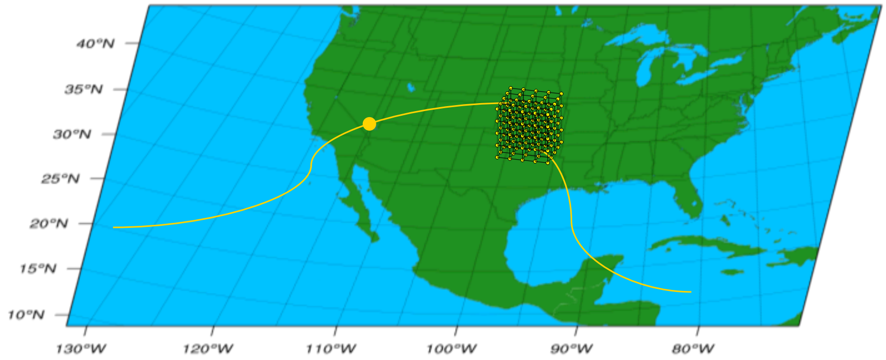

Figure 6. Schematic showing the grid of particles initialized over a flash flood report with sample backward trajectories.

This study seeks to describe the moisture uptake patterns for flash flood events in terms of seasonality, region, and diurnal cycle. Events were summarized by season as follows: spring [March, April, and May (MAM)], summer [June, July, and August (JJA)], autumn [September, October, and November (SON)], and winter [December, January, and February (DJF)]. Events were also categorized by region based on Saharia et al. (2017) and are shown in Figure 7, defined as 1) West Coast, 2) Arizona, 3) Front Range, 4) Flash Flood Alley, 5) Missouri Valley, and 6) Appalachians.

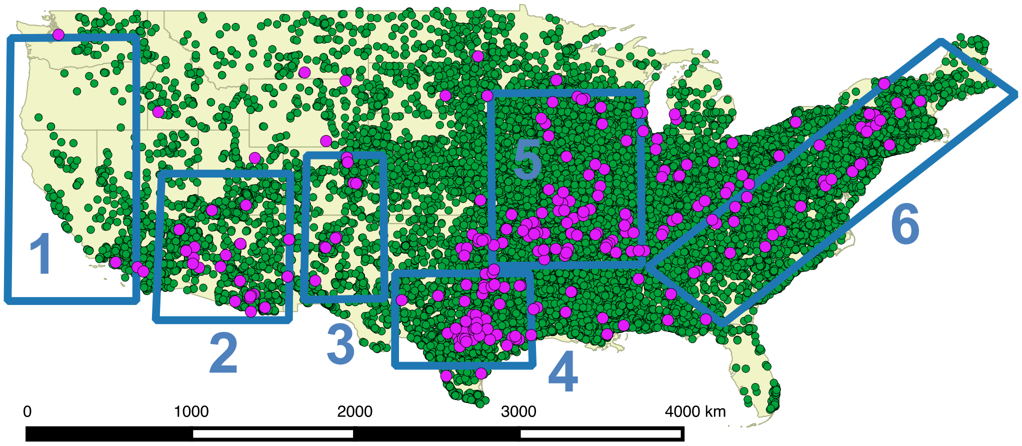

Figure 7. Flash flood events from *Storm Data* (green) and direct fatality events (pink) with flashiness regions overlaid. The regions are defined as follows: 1) West Coast, 2) Arizona, 3) Front Range, 4) Flash Flood Alley, 5) Missouri Valley, and 6) Appalachians.

The framework for analyzing each event is largely based on the work of Sodemann et al. (2008) who performed an analysis of moisture sources for Greenland based on seasonality and phase of the North Atlantic Oscillation (NAO). An example diagram is shown in Figure 8. Following Sodemann et al. (2008) the change is specific humidity q along an air parcel's trajectory is given by

$$\Delta q^0(t) = q(\mathbf{x}(t)) - q(\mathbf{x}(t-3h)) \tag{57}$$

where $\mathbf{x}(t)$ refers to the parcel's position at time t. A moisture increase, for example at t = -72h results in $\Delta q^0(t) > 0$, while a moisture decrease (t = -60 h) results in $\Delta q^0(t) < 0$. If the moisture increase occurs when the parcel's height is less than that of the PBL top (for example, at t = -72 h), then the source of the increase is diagnosed as within the boundary layer and ascribed to processes happening at the land surface, such as evapotranspiration. (It is conceivable, however, that local low-level advection from regions other than along the parcels' track could contribute to increases in moisture within the PBL. For the purposes of this study, this effect is not considered directly but is an area of future research.) If the moisture increase happens when the parcel's height is greater than that of the PBL top (at t = -36 h) the source is designated as non-boundary layer. Non-boundary layer sources of moisture include, but are not limited to, evaporation into the column from precipitation or vertical transport from convection. To mitigate these effects, the three hours preceding the flood were not used in calculating the total moisture uptakes at a given location.

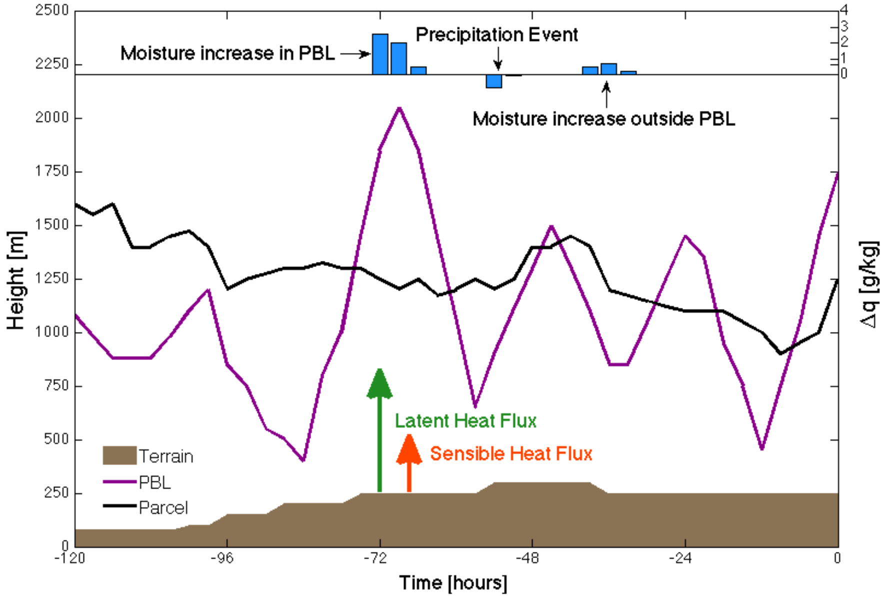

Figure 8. Sample parcel trajectory. Change in parcel water vapor mixing ratio (blue), terrain (brown), planetary boundary layer height (purple), and parcel height (black) along the trajectory. Adapted from Sodemann et al. (2008).

Beginning at the point at t = -120 h and proceeding forward in time, the fractional contribution f_n of an uptake at location n occurring within the boundary layer is given by

$$f_n = \frac{\Delta q_n}{q_n} \tag{58}$$

where Δq_n is the change in specific humidity and q_n is the specific humidity of the air parcel. Each moisture uptake reduces the importance of previous uptake, q_m, so the fractional uptakes are adjusted according to

$$f_m = \frac{\Delta q_m}{q_n} \quad m > n \tag{59}$$

When a precipitation event occurs, all previous uptakes are adjusted according to the amount of the moisture decrease (Δq^0_n) as

$$\Delta q_m^{'} = \Delta q_m + \Delta q_n^0 \cdot f_m \qquad m > n \tag{60}$$

At the end of the parcel's trajectory, the total fractions f_m are summed as to the parcel's location in or above the boundary layer. This produces values of f_{tot}, the total fraction of the final moisture due to boundary layer uptakes, e_{tot}, the total fraction of the final moisture due to non-boundary layer uptakes, and d_{tot}, the total fraction of the final moisture due to uptakes which cannot be classified by this method and are attributed to a variety of causes, such as being pre-existing moisture within the parcel (the contribution of moisture advection) or being uptakes smaller than a specified threshold.

In total, 19,253 flash flood events from NWS *Storm Data* within the CONUS were analyzed. There is no operational measure of flash flood severity, though Schroeder et al. (2016a) establish the groundwork for a classification of flash flood events based on impacts. Of those, 231 contained at least one fatality in *Storm Data* and were considered as severe events for the purposes of this study. A summary of events by region and season is shown in Table 3.

Table 3. Number of flash flood events by region and by season. Direct fatality events are parenthesized.

	DJF	**MAM**	**JJA**	**SON**	**Total**
Region 1 *West Coast*	31	11	68	50	160
Region 2 *Arizona*	40	7	753 (13)	227 (3)	1027 (16)
Region 3 *Front Range*	0	23	361 (3)	111 (5)	495 (8)
Region 4 *Flash Flood Alley*	67 (2)	666 (18)	652 (9)	359 (10)	1744 (39)
Region 5 *Missouri Valley*	242 (3)	1696 (20)	2629 (16)	594 (4)	5161 (43)
Region 6 *Appalachians*	267 (1)	799 (1)	2093 (7)	743 (6)	3902 (15)

4.2 Results

4.2.1 Seasonal and Temporal Distribution of Flood Reports

The *Storm Data* flash flood reports were first examined for seasonality and diurnal cycle by region. Figure 9 shows the distribution of events by season for each region.

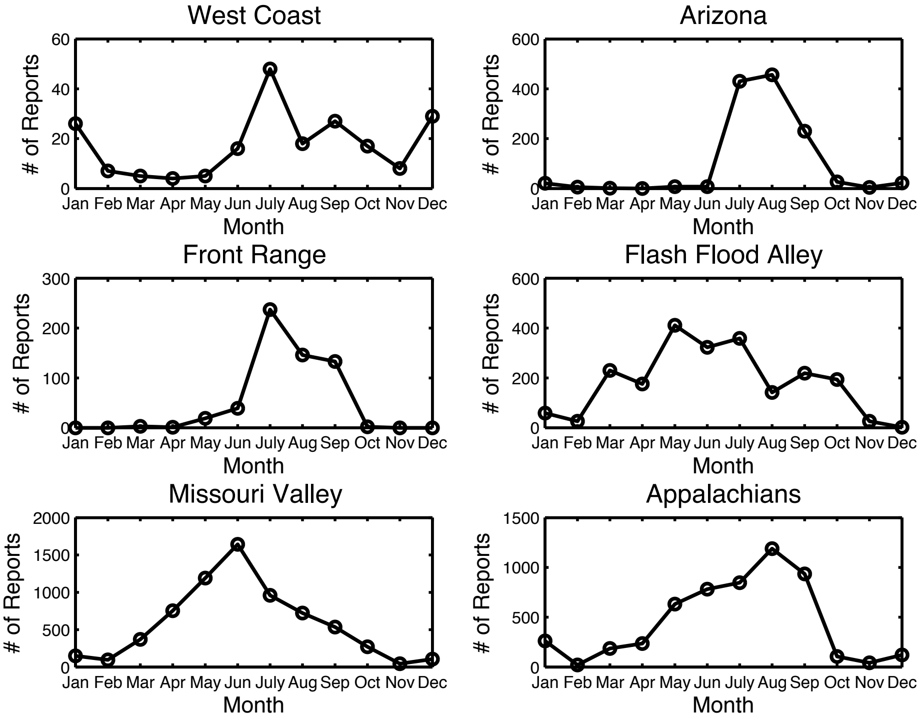

Figure 9. Distribution of *Storm Data* flash flood reports by month for the region indicated. The scale varies in each subplot based on the number of reports in the region.

Many of the regions have a distinct monthly climatological maximum for flash floods. The West Coast of the United States (Region 1) has the maximum number of flood events in July with secondary peaks in December and January. The summer and fall events for the West Coast occur in the eastern and southeastern portions of the domain as an extension of the NAMS. [While the bounding box for this region is the same as in Saharia et al. (2017), they include primarily events in the western portion of this subdomain, and this accounts for the difference in observed seasonality of floods. Other regions discussed here more or less agree with their results.] The maximum number of floods occurs in August in Arizona (Region 2) during the NAMS. Along the Front Range (Region 3), the maximum number of floods occurs from July-September. In Flash Flood Alley (Region 4), events are most likely to occur in May-July, but there is a secondary peak in the early fall, while in the Missouri Valley (Region 5), the number of floods increase until a peak in June and decrease thereafter. Lastly, along the spine of the Appalachians (Region 6), The number of floods increases until a maximum in August, with the fewest floods occurring in the late fall and winter. The seasonality of *Storm Data* observations of flash flooding agrees well with the climatologies of heavy rainfall discussed in Chapter 2.

In Figure 10, the distribution of *Storm Data* floods is shown for each region as a function of local time in order to assess the diurnal cycle of flash flooding in each region.

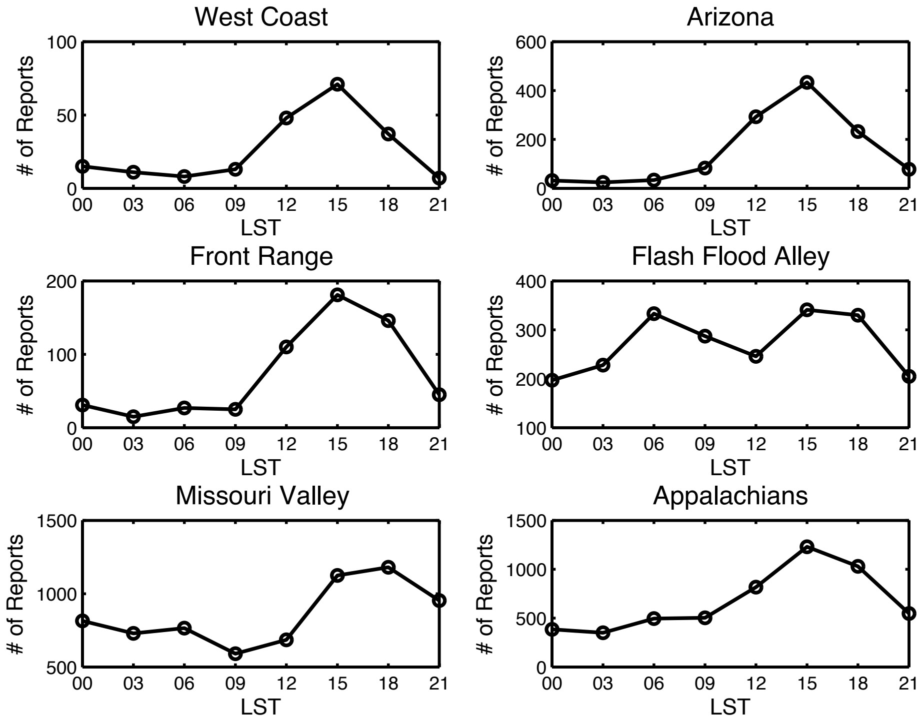

Figure 10. Distribution of *Storm Data* floods by local standard time for each region (LST=UTC-8 for Regions 1 and 2; LST=UTC-7 for Region 3; LST=UTC-6 for Regions 4 and 5, and LST=UTC-5 for Region 6). Totals are reported at the beginning of each 3-hour window (i.e. floods occurring between 03-06 UTC are marked at the 03 UTC point). The scale varies in each subplot based on the number of reports in the region.

For the West Coast, Arizona, and the Front Range there is a peak in floods occurring during the late afternoon, between 3 PM and 6 PM LST due to afternoon thunderstorms. For Flash Flood Alley, there is a similar afternoon peak due to daytime convection, but the distribution is bimodal with a maximum nearly equal in magnitude occurring between 6 AM and 9 AM LST, illustrative of the nocturnal maximum of convection as MCSs propagate from the Rockies. In the Missouri Valley, most floods occur between 3 PM and midnight LST, but there are also some floods occurring in the early morning hours, with a minimum from 9 AM until noon LST, again due to the well-documented cycle of convection in the central US. The Appalachians also have a maximum in the late afternoon hours.

While *Storm Data* is intended to capture all events that occur within a forecast office's area of responsibility, the number of reports does depend on the availability of citizens or spotters to report the storm. Therefore, it is possible that events that occur overnight or in remote regions may be underreported.

4.2.2 Case Studies

Most of this chapter will focus on the properties of the land surface in aggregate. However, in order to illustrate the utility of using trajectories to delineate moisture sources for flash flooding, example cases are presented for flash floods that occurred in June 2008 in Iowa and May 2010 in Nashville, TN. The first case exemplifies a situation in which parcel moisture is increased by interactions with the land surface. In the second case, this methodology reveals that advection plays a larger role. The Iowa Floods of 2008, which occurred from 1-15 June, followed a cool and snowy winter. Following a late melt of the winter snowpack, soils were abnormally moist (NWS 2009, Coleman and Budikova 2010). In total, the Midwest floods of 2008 caused $11.3 billion of damage across several states and were responsible for 24 deaths (NCEI 2017).

The backward trajectories for parcels that arrive at 950 hPa, ~850 hPa, ~700 hPa, and 500 hPa are shown in Figure 11. The approximation notation will be dropped throughout this chapter, but because of the 30 hPa grid spacing in the vertical, parcels actually end at 860 hPa and 710 hPa.

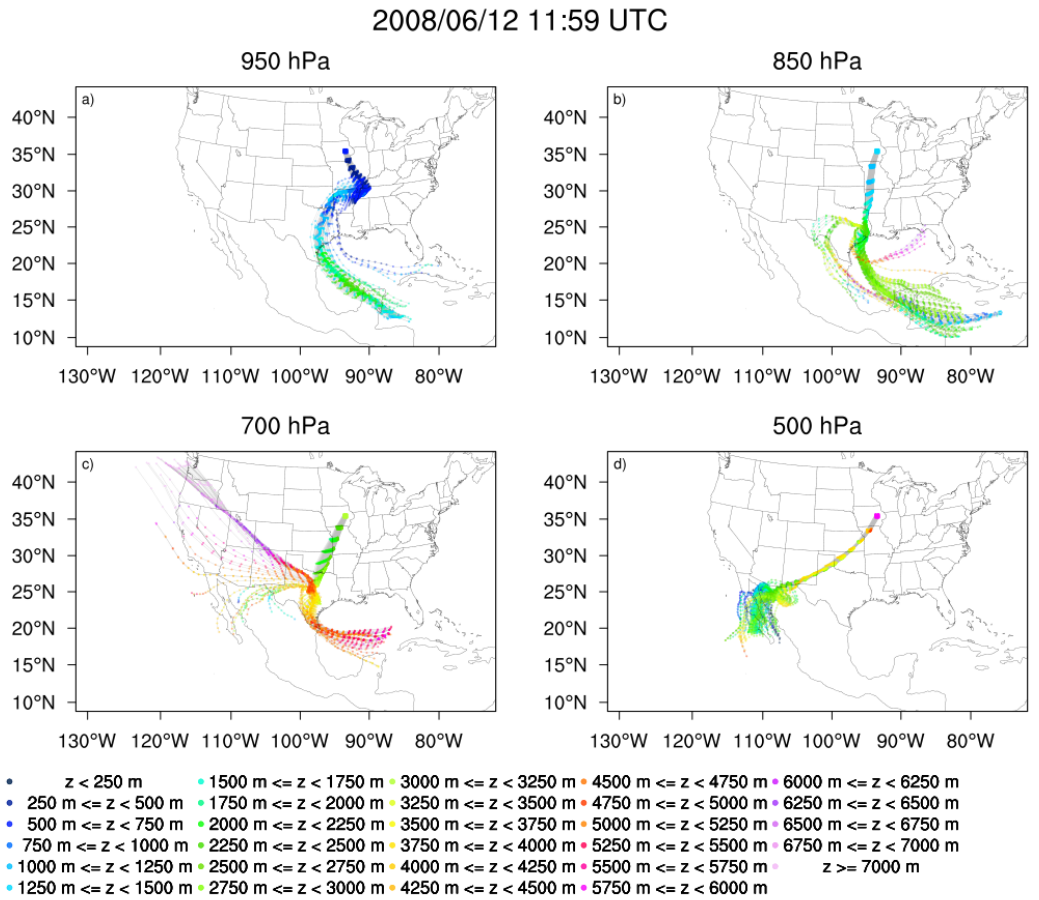

Figure 11. 5-day backward trajectories colored by parcel height for a flash flood report occurring at 11:59 UTC on 12 June 2008, part of the Iowa flooding of 2008. Parcels ending at a) 950 hPa, b) 850 (860) hPa, c) 700 (710) hPa, and d) 500 hPa are shown.

There are 121 parcels per level (11x11 grid). At low-to-mid levels, most parcels have an origin over the Gulf of Mexico or the Caribbean Sea. Parcels that end at 950 hPa originate near the Yucatan Peninsula and traverse the western Gulf of Mexico before descending over Arkansas and western Tennessee. Most parcels ending at 850 hPa originate at mid-to-low levels in the Caribbean Sea, and, although they pass briefly over the Yucatan Peninsula, remain over the Gulf of Mexico before beginning a descent from eastern Texas to Iowa. Parcels ending at 700 hPa originate in one of two places: over the Pacific coast, where they descend toward central Texas, or in the central Gulf of Mexico, where they also descend in central Texas before arriving in Iowa at ~2500-

2750 MASL. Parcels which end at 500 hPa in Iowa begin as low level parcels over Baja California and the Gulf of California, and ascend across the Southern Great Plains.

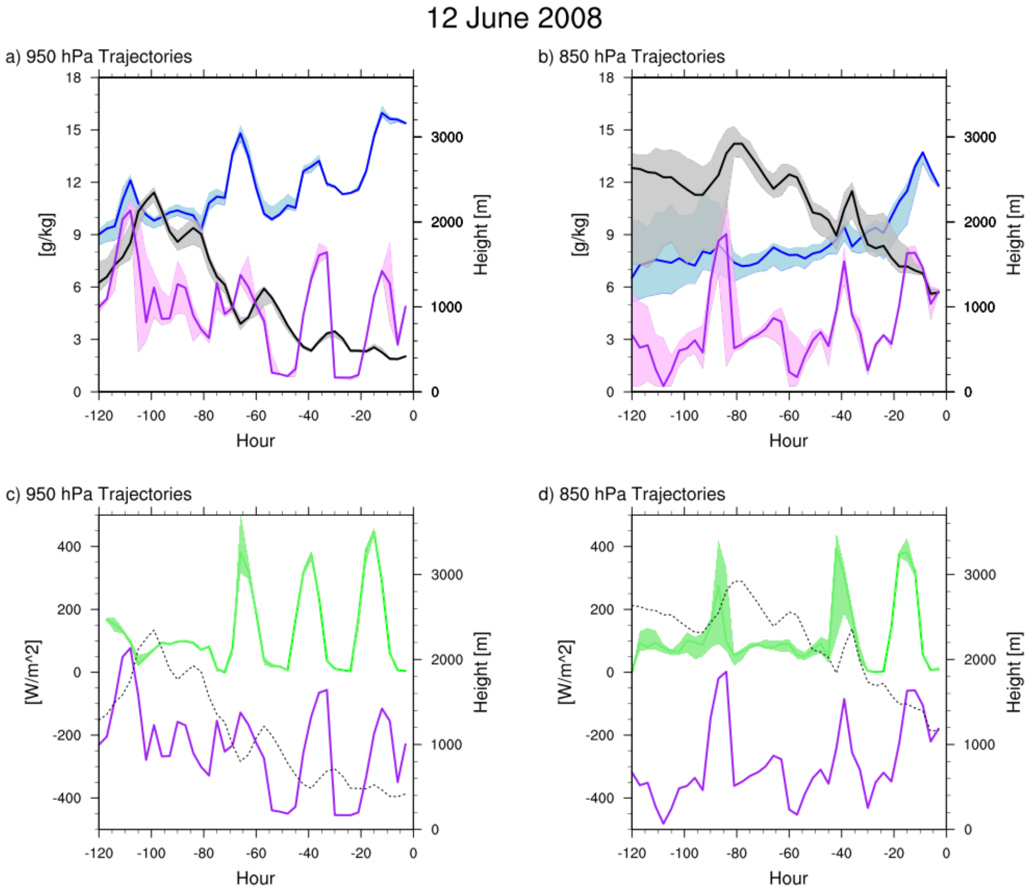

Figure 12. Median parcel specific humidity (blue), height (black, solid in a-b, dashed in c-d), surface latent heat flux below parcel (green) and PBL height at parcel location (purple) for parcels ending at 950 hPa (panels a) and c)) and 850 hPa [panels b) and d)] for the Iowa flood event occurring at 11:59 UTC on 12 June 2008. Shading indicates interquartile range (25th to 75th percentiles) for all parcels at a time step.

The distributions for the specific humidity, height ASL, surface latent heat flux and PBL height for the plume of 121 parcels are shown in Figure 12. Here, surface evapotranspiration plays the primary role in the increase in water vapor of the air parcels, as median latent heat flux values at the surface are in excess of 400 Wm^{-2} when the parcel resides in the boundary layer. Specific humidity of parcels ending at 850 hPa (panel b) exhibits a marked increase as parcels descend into the boundary layer prior to the flood start time, though specific humidity had been increasing slowly as the parcels descended.

The Nashville flood of 1-2 May 2010 was the result of two quasi-stationary MCSs, which resulted in total rainfall of 344.7 mm at Nashville International Airport and an observation of 493 mm in Camden, TN. There were widespread weekend rainfall totals in excess of 200 mm and flooding causing 26 fatalities and $2 billion in damage (NWS 2011). At upper levels, there were negative height anomalies in the western United States and a closed upper low in the Gulf of St. Lawrence, with a ridge in the eastern United States (Durkee et al. 2012). The atmospheric conditions at 850 hPa prior to this event were characterized by a lee trough off the eastern coast of Mexico and a stronger subtropical ridge over the western Atlantic as well as abnormally high values of IWV and IVT generated by the anomalously strong poleward flow caused by this height gradient (Moore 2012). PW anomalies were greater than 2 standard deviations above the mean, and the axis of highest PW was oriented the same as the surface boundary (Durkee et al. 2012).

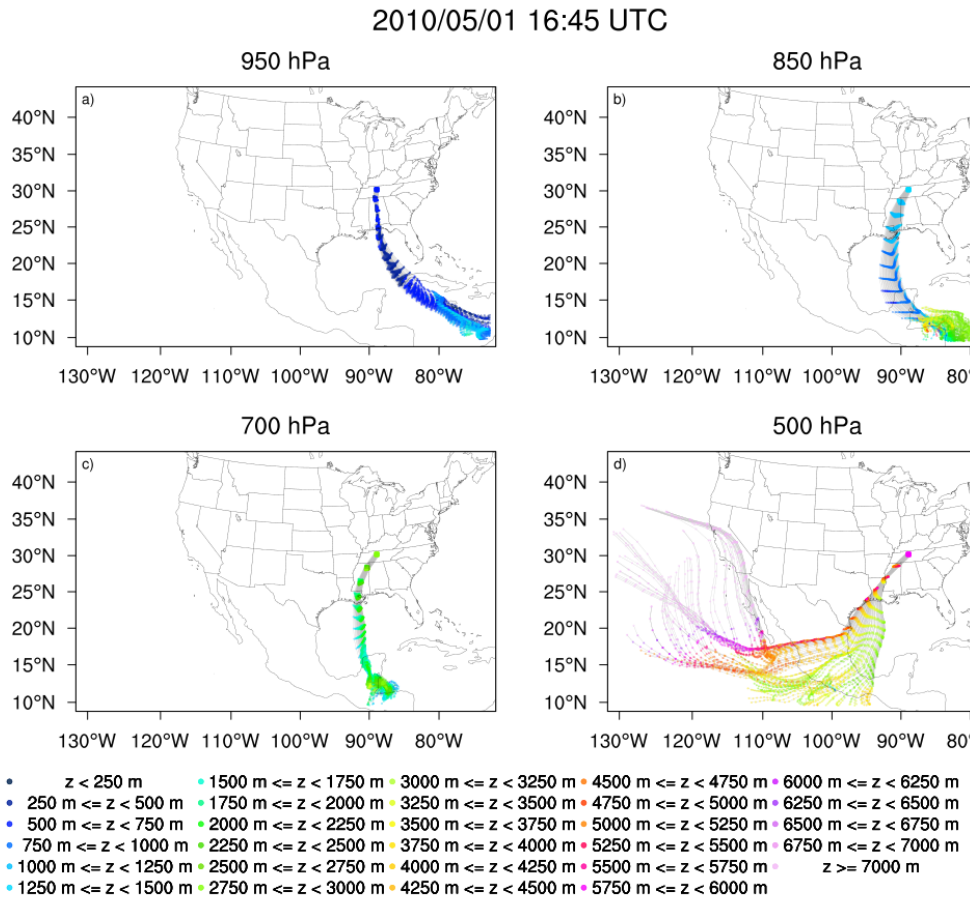

Figure 13. As in Figure 11 but for a flood report at 16:45 UTC on 1 May 2010, part of the Nashville flood event.

A spatial map of parcel trajectories is shown in Figure 13. The path that parcels follow generally veers with increasing height. Trajectories ending at 950 hPa over Nashville originate in the Caribbean Sea, and descend slightly before reaching their final destination. Parcels which terminate at 850 hPa originate near the Honduran and Nicaraguan coasts, above 3000 m ASL and then descend before ascending slightly again as they reach the Gulf Coast. Parcels that end at 700 hPa originate near Belize, and maintain their altitude as they approach the CONUS. Parcels ending at 500 hPa originate over the Pacific Ocean. Some descend over Mexico and Central America before ascending again toward Tennessee, while others remain at the same altitude. The trajectories in this case correspond very well with those calculated from NCEP Global Data Assimilation System (6-hourly; 1°x1° horizontal grid spacing) data with the HYSPLIT model by Moore et al. (2012), though they were launched at slightly different times and from a narrower spatial extent.

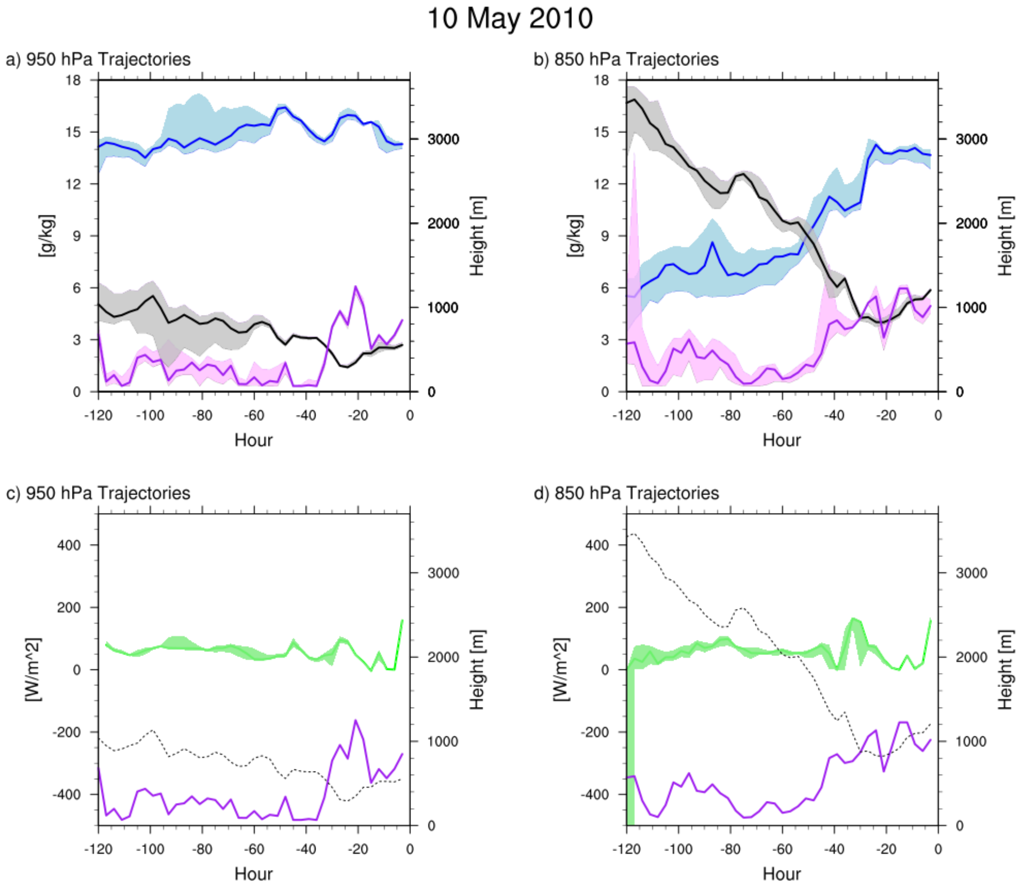

Figure 14. As in Figure 12, but for the flash flood occurring at 16:45 UTC on 1 May 2010.

Low-level parcel trajectories for the Nashville flood event are shown in Figure 14. Parcels ending at 950 hPa generally remain above the boundary layer, but begin with values of specific humidity of ~14 g kg^{-1}, which they maintain throughout their transit. The parcels enter the boundary layer 36 hours before the flood time, and increase their moisture again slightly due to interactions within the PBL. The Nashville floods, however, represent a case of mostly advective contributions to the heavy rainfall that triggered flash flooding. At 850 hPa, the parcels steadily decrease in height and increase in moisture, but all of this occurs above the boundary layer, with the exception of one sharp increase of ~4 g kg^{-1}at 36 hours before the flash flood. In contrast with the case of the 2008 Iowa floods, advection of moisture seems to have played a more important role for the moisture availability in the Nashville case. Additionally, latent heat fluxes along the trajectories in the Iowa floods have daytime peaks of greater than 300 W m^{-2}, whereas in the Nashville case, these values are less than 150 W m^{-2}.

While individual case studies provide insight into the impact of land-atmosphere interactions on flash flooding an event-by-event basis, examining thousands of cases allows for the development of a moisture source climatology, which may aid forecasters in predicting heavy rain and flash flooding.

4.2.3 Parcel Trajectory Analysis

Although parcels were spaced every 30 hPa in the vertical from 950 hPa to 470 hPa for the trajectory calculations, the following analyses focus on the parcel nearest to the mandatory synoptic levels (950 hPa, 850 hPa, 700 hPa, 500 hPa) at the endpoint of the trajectory (parcels launched from 950 hPa, 860 hPa, 710 hPa, 500 hPa). Values for selected atmospheric and land surface variables were recorded every 3 hours along the trajectory. When separated by region and season, the trajectory analysis confirms that many of the well-documented regional climatological features are present and instrumental for flash flood events. The following discussion will feature these prominent mechanisms, but analysis for other regions and seasons will be included in

Appendix A. Parcels which are underground for their given pressure level, especially in the western regions, are not included in these plots or any subsequent analysis.

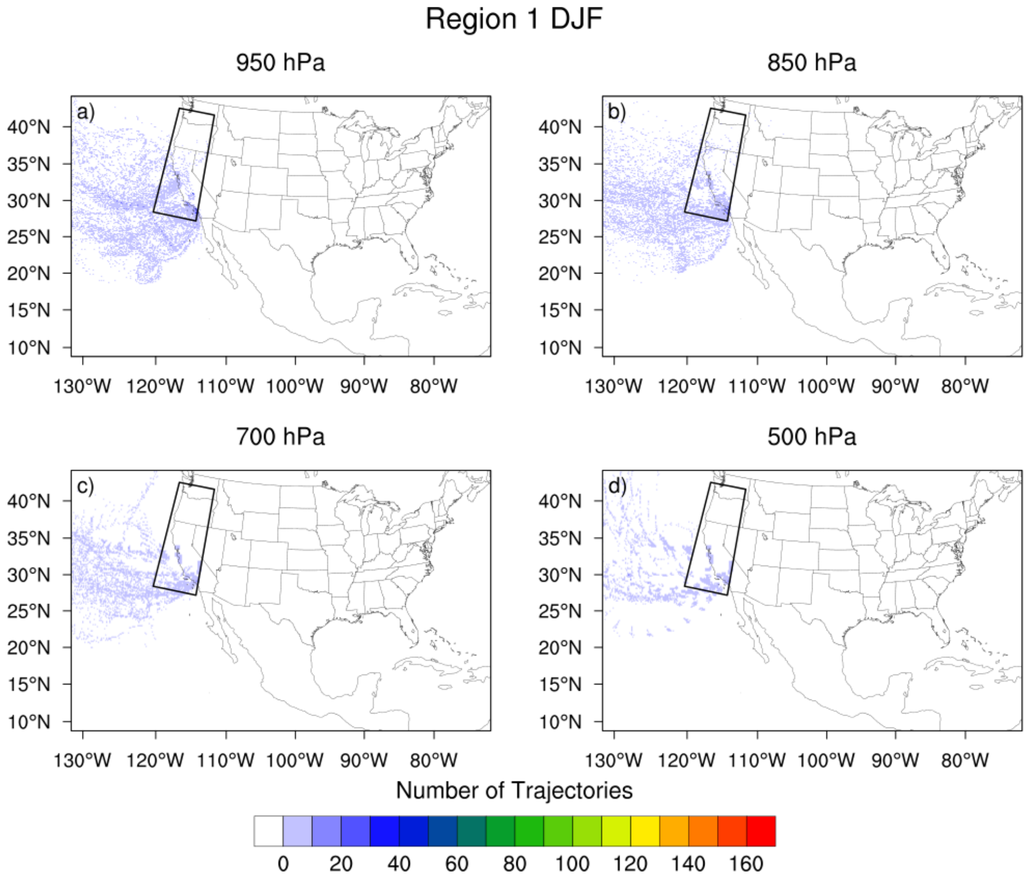

Figure 15. Trajectory density (number of trajectories passing through a given grid point) for parcels ending at the approximate pressure level indicated for flash floods occurring in Region 1 (West Coast, outlined) during DJF.

For the West Coast, during DJF there is nearly unidirectional flow at all levels off the Pacific Ocean (Figure 15), indicative of landfalling extratropical cyclones and the moisture transport associated with enhanced vapor transport from the tropical Pacific, discussed extensively in Chapter 2. In the spring, there are only 11 events, all of which have their flow at all levels off the Pacific Ocean. Because Region 1 as delineated by Saharia et al. (2017) includes portions of southern California and Nevada, there is a warm season peak in activity during the North American Monsoon (Figure 9).

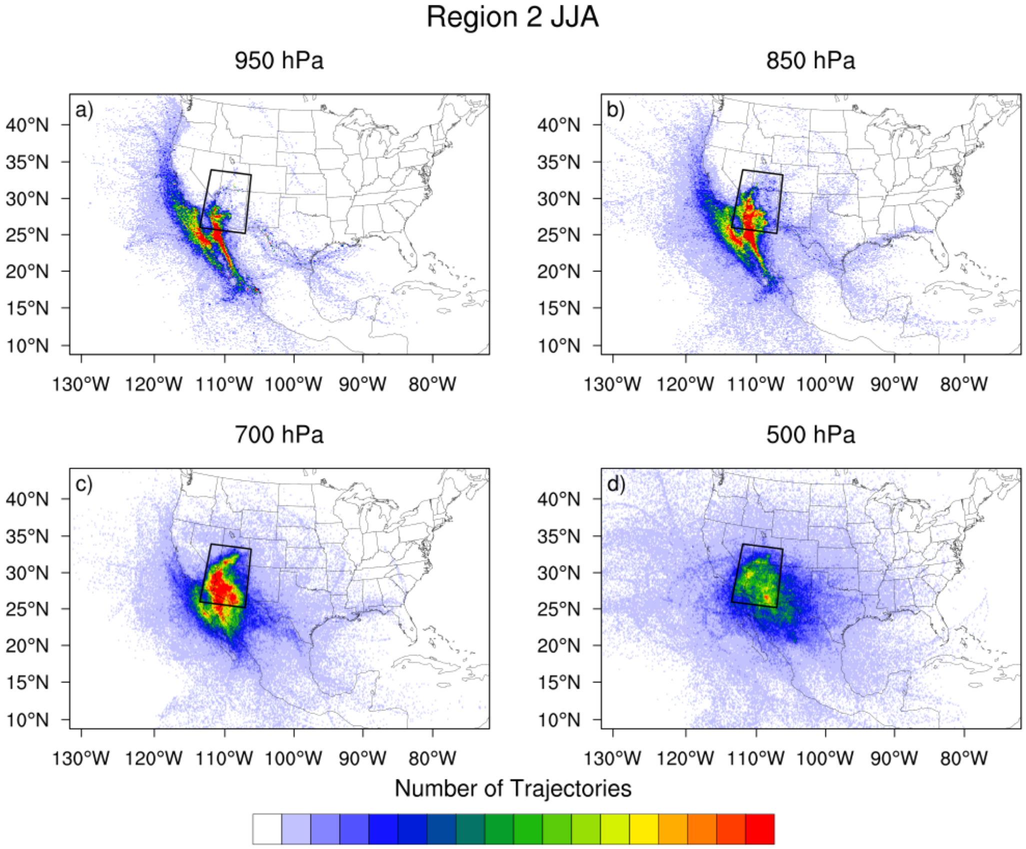

Figure 16. As in Figure 15, but for Region 2 (Arizona) during JJA.

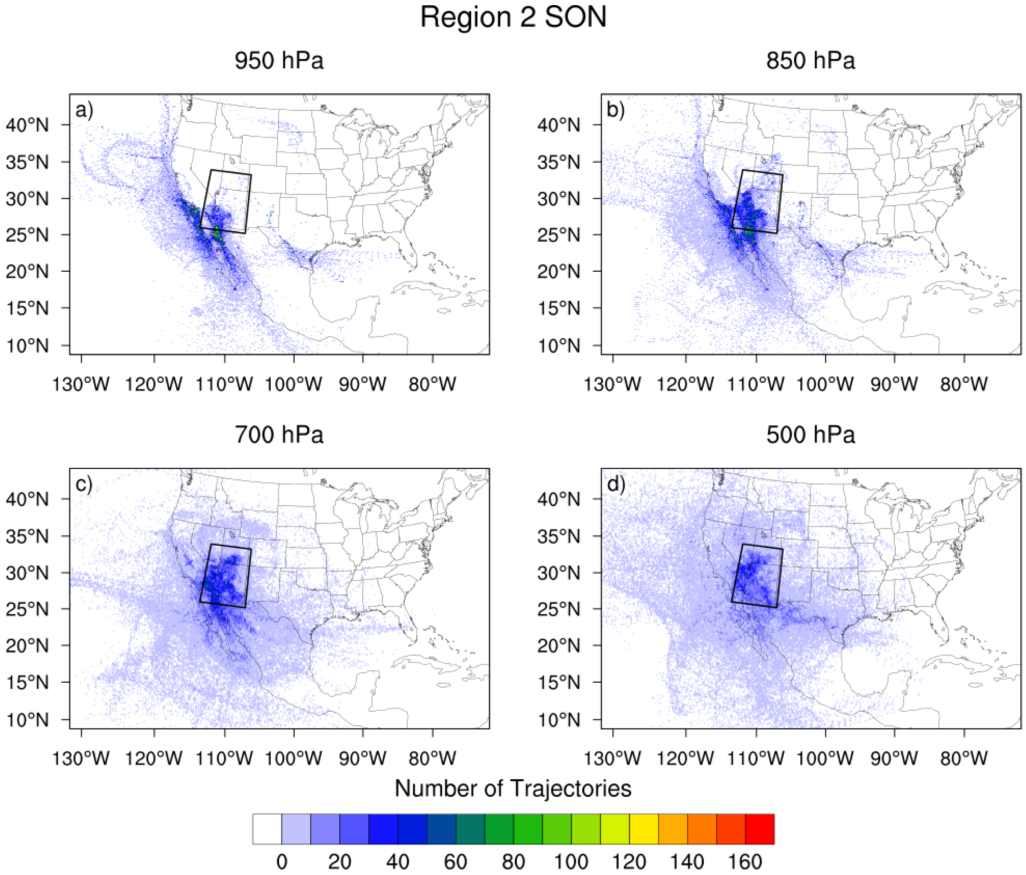

Figure 17. As in Figure 15, but for Region 2 (Arizona) during SON.

For Arizona, during DJF, the flow resembles that of the West Coast region for the same season, with all trajectories originating over the Pacific Ocean (see Appendix A). As it was for the West Coast, Region 2 has a minimum in flash flood reports during MAM, with only 7 reports occurring during the study period. As the North American Monsoon begins to develop and mature later in JJA, the maximum concentration in parcel trajectories lower than 700 hPa occurs off the coast of Baja California on the Pacific side and over the Gulf of California itself (Figure 16). Flow at 500 hPa is curved around the anticyclone that forms in the mid-troposphere during JJA (not shown) and persists through the summer before tapering off during SON (Figure 17).

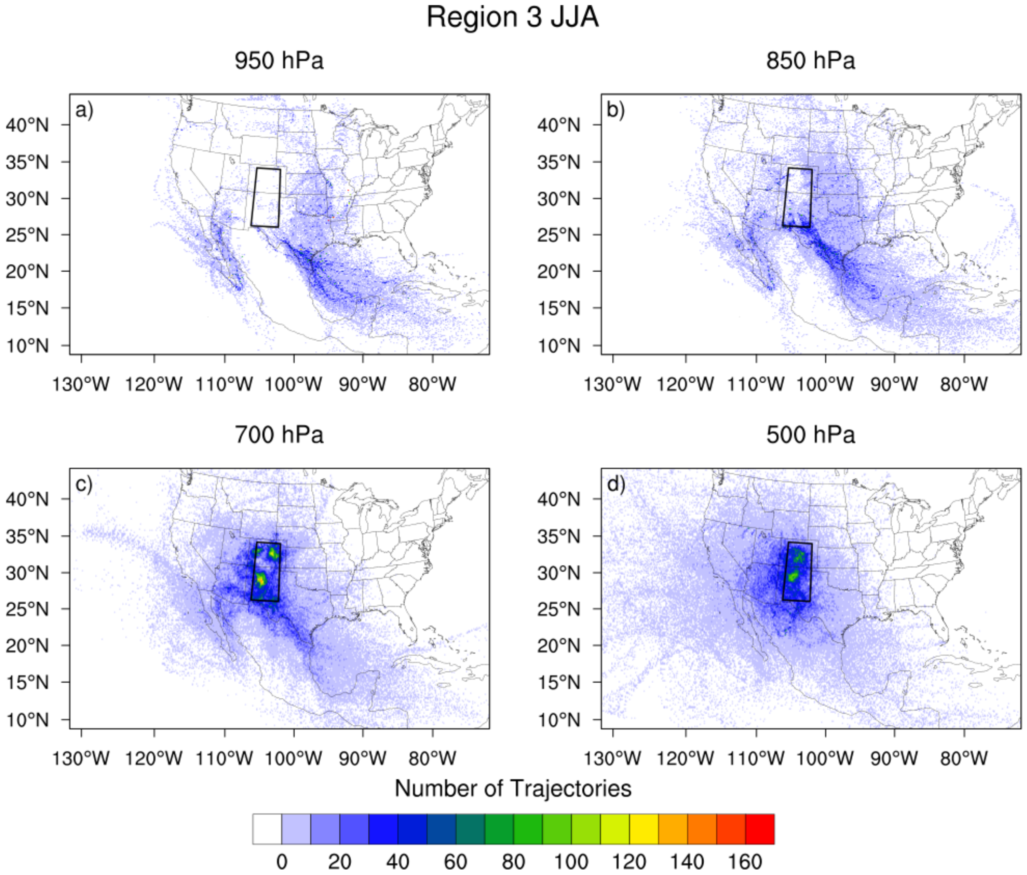

Figure 18. As in Figure 15, but for Region 3 (Front Range) during JJA.

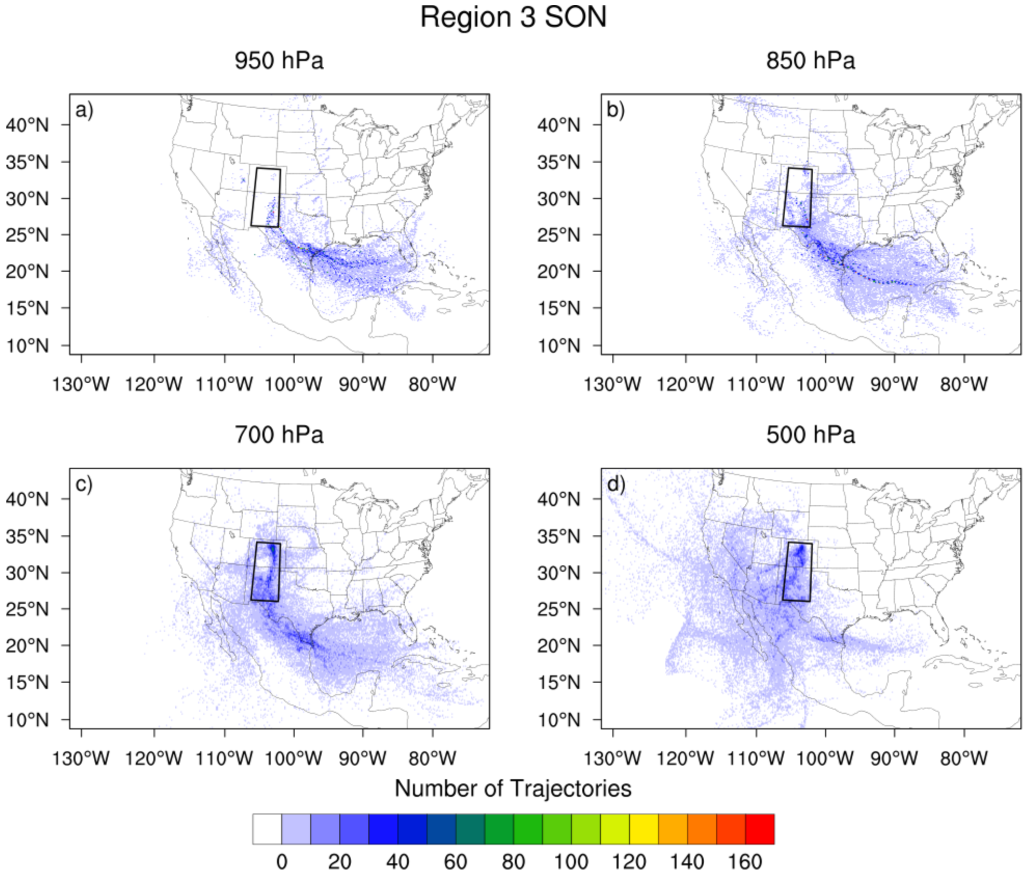

Figure 19. As in Figure 15, but for Region 3 (Front Range) during SON.

No floods occur during the study period during DJF in the Front Range (Region 3). For floods occurring along the Front Range in all other seasons, parcels ending at 850 hPa have a long fetch over the Gulf of Mexico. Some parcels ending at 700 hPa, originate over the Gulf of Mexico and ascend (not shown) as they reach the Front Range while some originate over the Pacific. Parcels ending at 500 hPa exhibit a pattern similar to those in Arizona for JJA, with an upper level system over the southwestern United States (Figure 18). Trajectories ending at 700 hPa vary in origin from the Gulf of Mexico or Caribbean Sea, the Gulf of California and the Pacific Ocean, or from the north. For floods occurring in SON, flow ending at 850 hPa and 700 hPa has two predominant flow paths: a fetch over the Gulf of Mexico and through western Texas and over the Gulf of California. The 500 hPa flow is westerly, however, save for a small fraction of parcels which ascend from over the Gulf of Mexico.

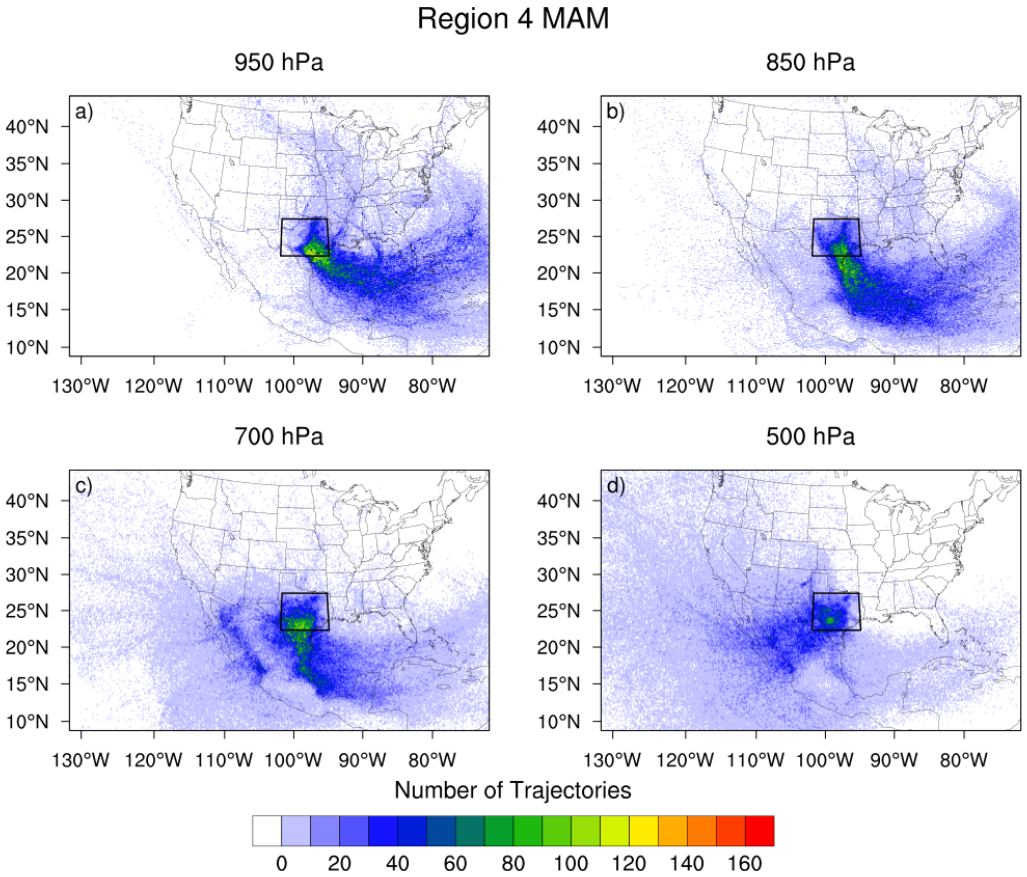

Figure 20. As in Figure 15, but for Region 4 (Flash Flood Alley) during MAM.

For Flash Flood Alley (Region 4), flow for DJF events (see Appendix A) is highly curved for parcels ending at 950 hPa and 850 hPa through the Gulf of Mexico and into central Texas. Flow for parcels ending at 700 hPa descends from over central Mexico or over the western Gulf of Mexico. Flow for parcels ending at 500 hPa is westerly or southwesterly. For floods occurring in MAM, the preferred flow path of parcels veers with height (Figure 20), though flow in the lower troposphere traverses the Gulf of Mexico. Flow for parcels ending at 950 hPa is easterly to southeasterly off the northern Gulf of Mexico. For parcels ending at 850 hPa, it becomes southeasterly to southerly. For parcels ending at 700 hPa, the flow is southerly, and for parcels ending at 500 hPa, flow is predominantly southwesterly. In JJA (Figure 21), the trajectories for parcels ending at 950 hPa have a more southerly component than they do in the spring, and the area with the core of highest concentration of trajectories spanning from the Caribbean Sea into the Western Gulf of Mexico. Trajectories ending at 700 hPa and 850 hPa share a similar north-south oriented axis. Some upper-level trajectories ascend from low-levels over the Gulf of Mexico, while others exhibit cyclonic curvature from the southwest or anticylconic curvature from the northwest. In SON, the lowest level trajectories back slightly from their positions in JJA, and the 500 hPa flow becomes southwesterly again.

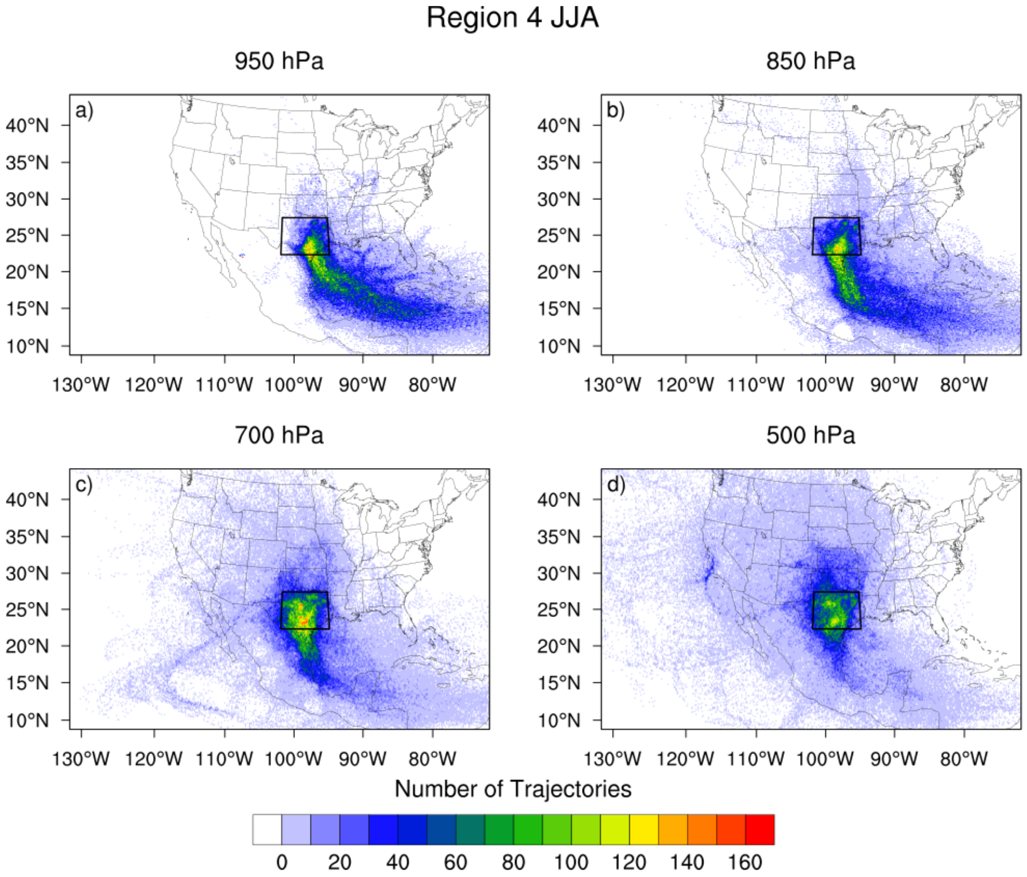

Figure 21. As in Figure 15, but for Region 4 (Flash Flood Alley) during JJA.

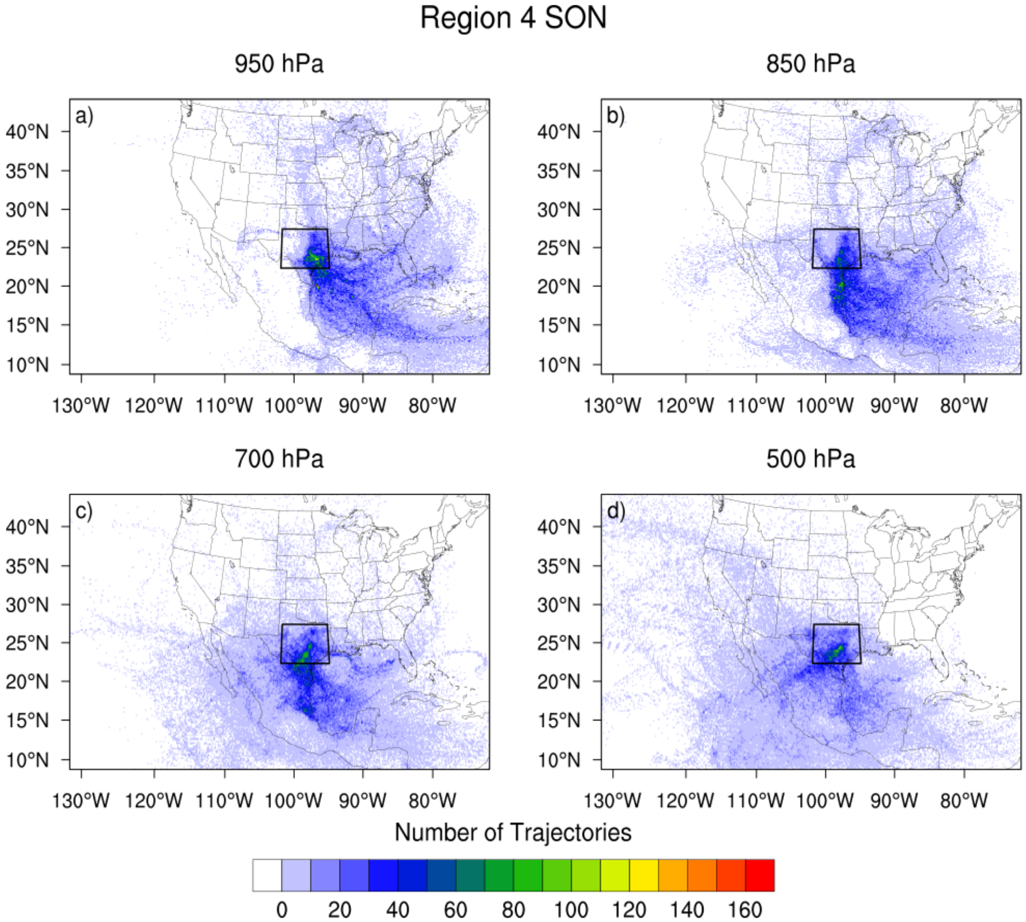

Figure 22. As in Figure 15, but for Region 4 (Flash Flood Alley) during SON.

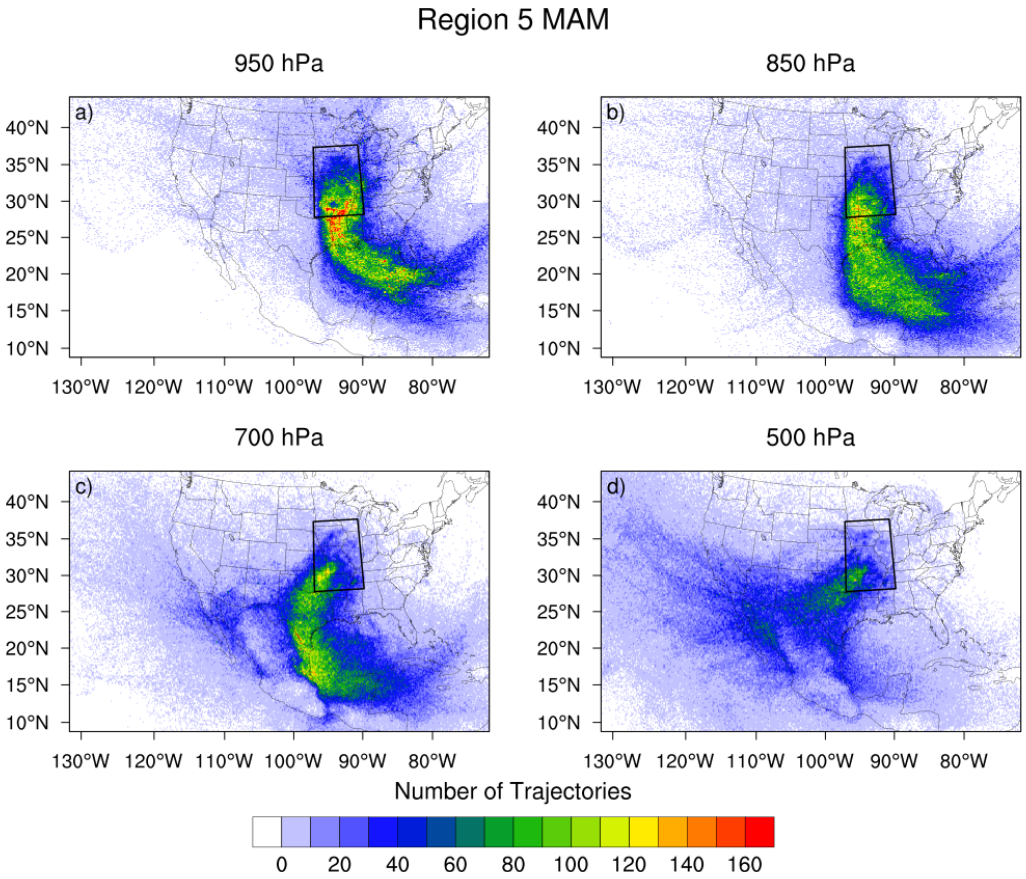

Figure 23. As in Figure 15, but for Region 5 (Missouri Valley) during MAM.

For the Missouri Valley (Region 5), the flow pattern of trajectories strongly resembles that of Flash Flood Alley. In DJF, trajectories ending at 950 hPa exhibit easterly flow across the northern Gulf of Mexico and a curve to a southerly flow into the Missouri Valley (see Appendix A). For trajectories ending at 850 hPa, this pattern is displaced southward, and parcels turn northward near the Mexican coast. Some trajectories that end at 700 hPa exhibit the same pattern as those ending at 850 hPa, while others begin over the Pacific Ocean and descend. Flow for 500 hPa is southwesterly. The two seasons with the most flash flood events are MAM and JJA in Region 5. The pattern of trajectory density during MAM (Figure 23) bears similarity to that in DJF, save for a northward shift in the 500 hPa trajectories. In JJA (Figure 24), trajectories at 500 hPa shift northward further, and are less organized over the Pacific Ocean than in the cool season. Trajectories that were launched from 950 hPa and 850 hPa track over the Caribbean Sea and Gulf of Mexico before turning northward and tracking across eastern Texas and Oklahoma, and over Arkansas and Missouri. Trajectories that end at 700 hPa have a slightly more westerly component than those at lower levels. In the fall (Figure 25), the trajectories make a similar easterly shift from JJA to SON.

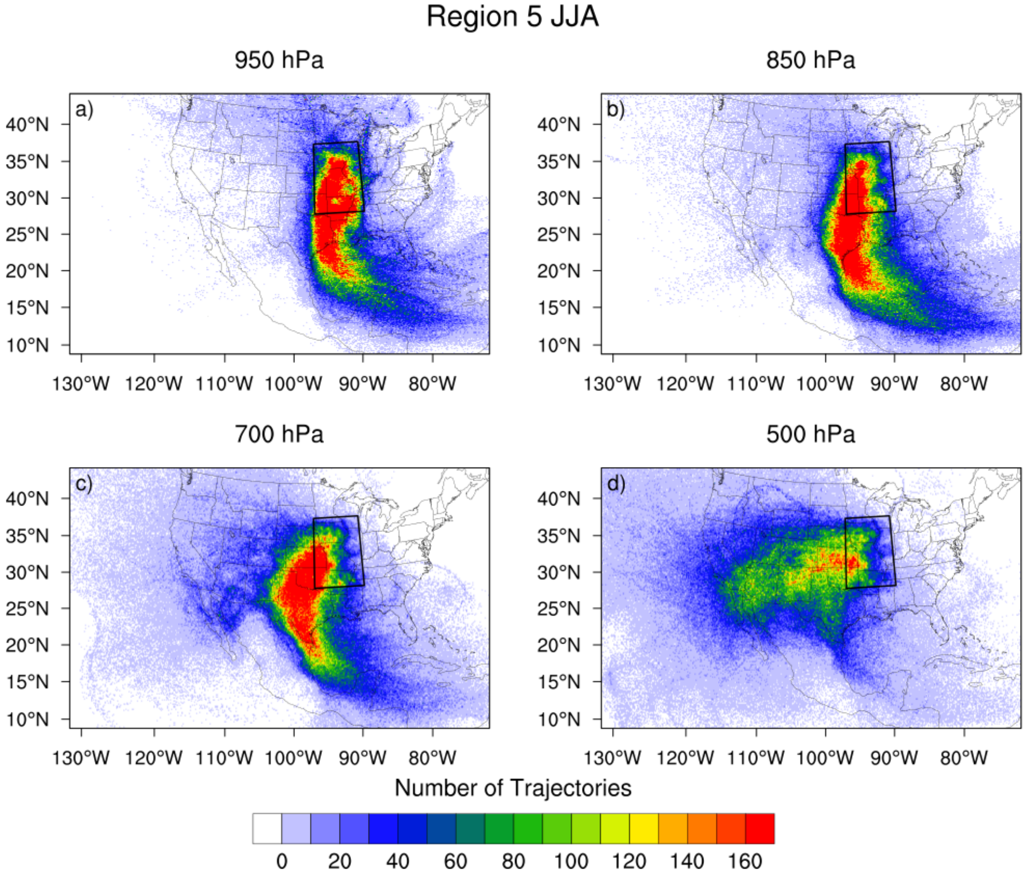

Figure 24. As in Figure 15, but for Region 5 (Missouri Valley) during JJA.

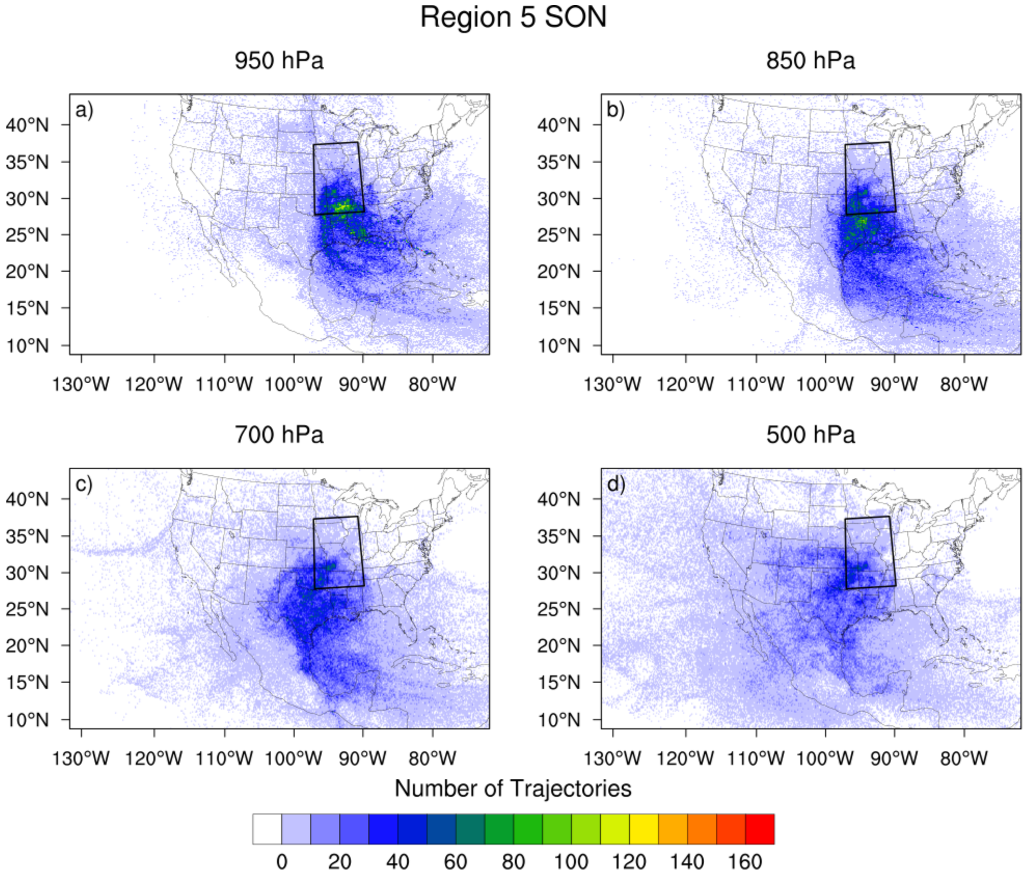

Figure 25. As in Figure 15, but for Region 5 (Missouri Valley) during SON.

For the Appalachians (Region 6), identifying patterns is not as straightforward since the region spans a large area from north to south. The flow for parcels that terminate at 950 hPa and 850 hPa is highly curved and passes over the Atlantic Ocean in DJF (see Appendix A). Many parcels ending at 700 hPa pass over the Gulf of Mexico and along the Appalachians before reaching their final destinations. While some parcels launched from 500 hPa have their origins in the Pacific Ocean, others begin in the Gulf of Mexico and Caribbean Sea and ascend as they move northward. In MAM, many low-level trajectories still approach from over the Atlantic (Figure 26).

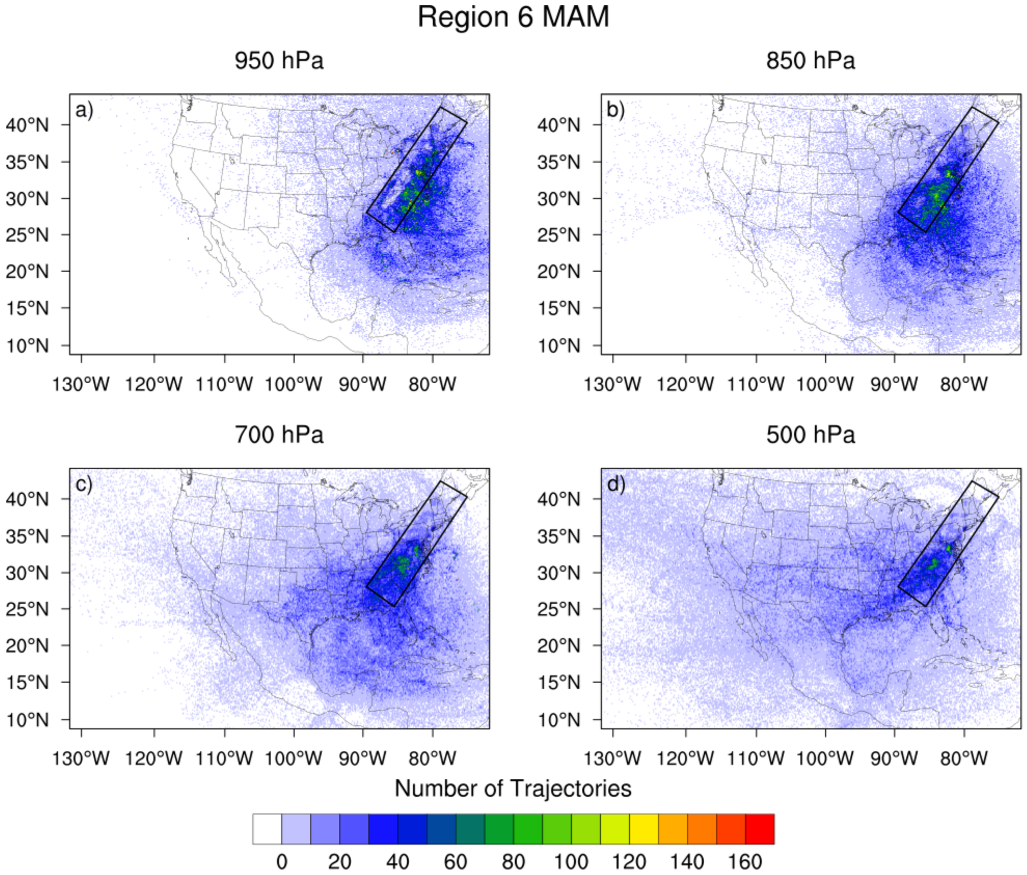

Figure 26. As in Figure 15, but for Region 6 (Appalachians) during MAM.

In JJA the maximum in parcel trajectory positions is located along the axis of the mountains, with some low-level flow off the Atlantic and Gulf of Mexico (Figure 27). In SON, the parcels that terminate at 850 hPa and 700 hPa have their origins over the Gulf of Mexico or the Atlantic Ocean, while many of the parcels that terminate at 950 hPa have their origins over the Atlantic Ocean (Figure 28).

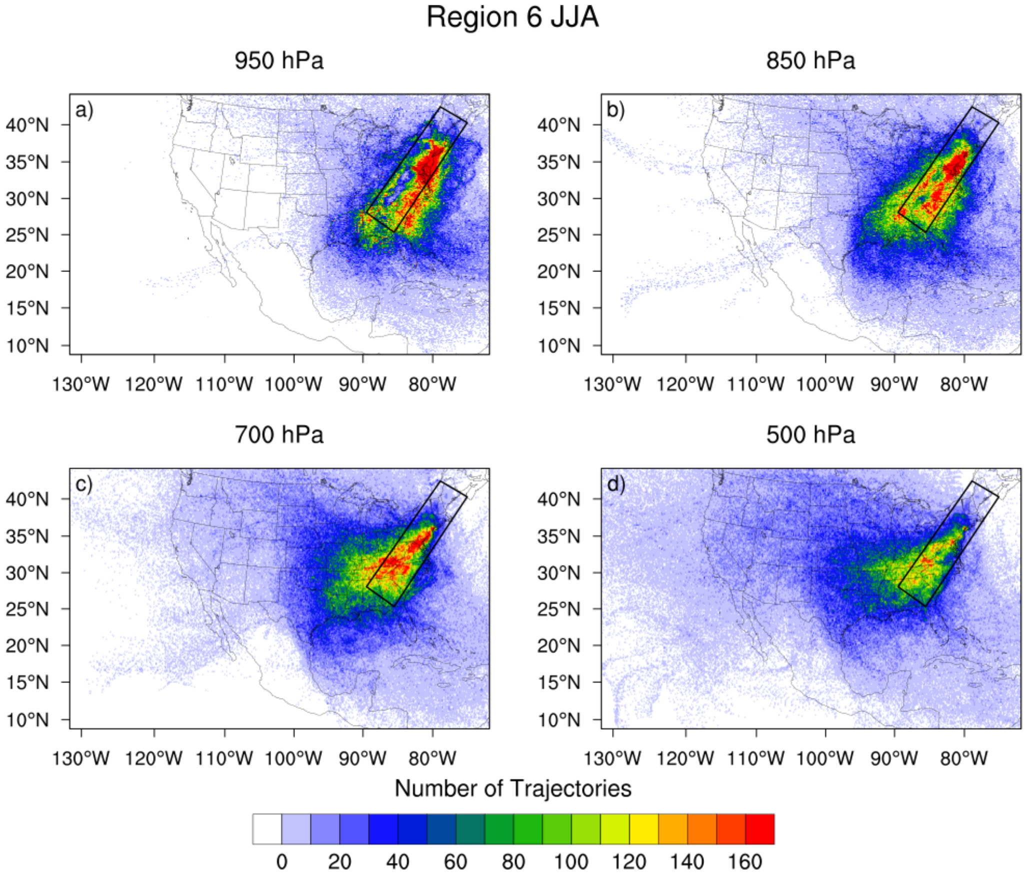

Figure 27. As in Figure 15, but for Region 6 (Appalachians) during JJA.

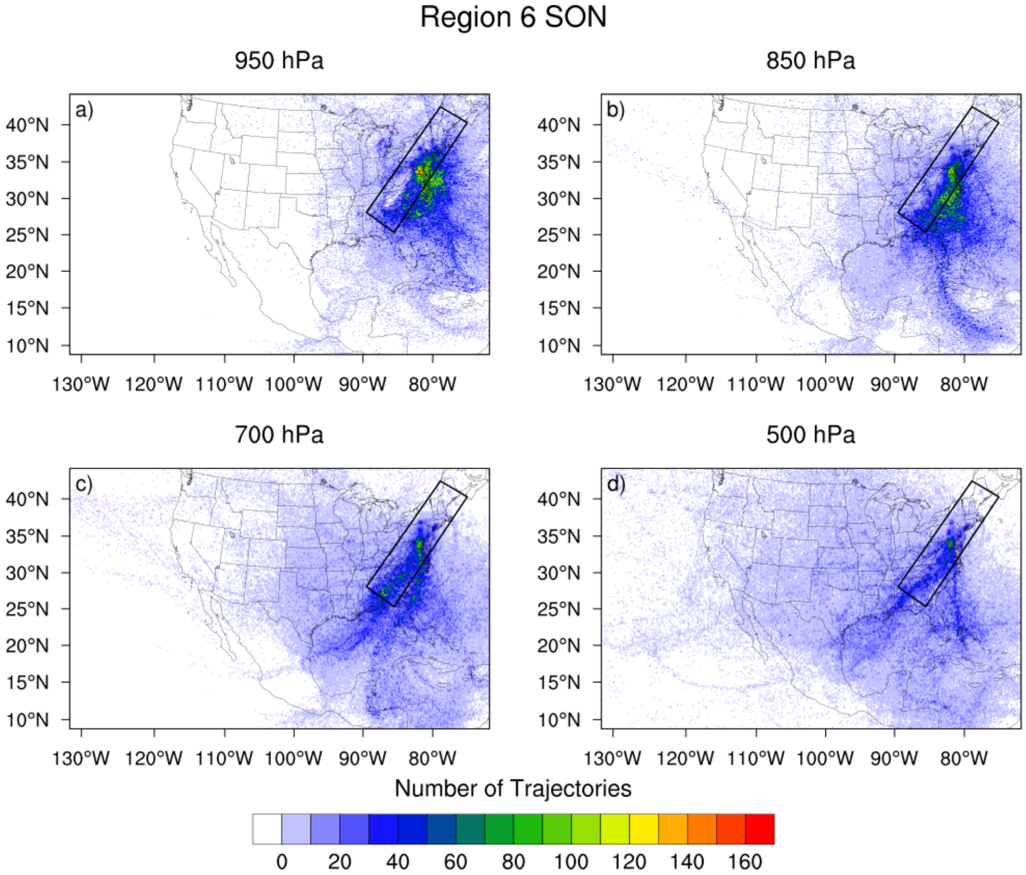

Figure 28. As in Figure 15, but for Region 6 (Appalachians) during SON.

The locations of increases in parcel specific humidity were located using the methodology described in Sodemann et al. (2008). If the uptake occurred with the parcel height less than the height of the PBL (from NARR), then the moisture uptake was attributed to the land surface. (Note: The authors of Sodemann et al. (2008) impose a criterion that each change in specific humidity must be greater than or equal to 0.2 g kg^{-1}, in order to reduce spurious uptakes. They note, however, that this threshold is arbitrary. In this case, a value of 0.1 g kg^{-1} was the threshold for an uptake to be attributed as 'boundary layer' or 'non-boundary layer.') If the uptake occurred with a parcel height higher than that of the PBL, the moisture increase was counted as a non-boundary layer contribution. For each region and season, the total boundary layer and non-boundary layer moisture uptakes (increases in specific humidity) were plotted. Moisture increases were integrated from individual parcel changes in specific humidity according to the adaptation of Sodemann et al. (2008) Equation 3:

$$Q_{tot} = \frac{1}{g} \sum_{j=1}^{j=N} \Delta q_j \cdot 10^{-3} \cdot \Delta p_j \qquad [mm] \tag{61}$$

where Q_{tot} is the total contribution from either the boundary layer or above the boundary layer, g is the acceleration due to gravity, Δq_j is the increase in parcel specific humidity (in g kg^{-1}) for each uptake j (in the total number of uptakes N), and Δp_j is the vertical extent of the air parcel (in Pa).

The total boundary layer uptakes and non-boundary layer uptakes are shown in Figure 29 for all events from 2007-2013. During DJF, the main source for non-boundary layer moisture is the Gulf of Mexico. The Gulf of Mexico and Atlantic Ocean are also the key moisture sources for boundary layer uptakes.

In MAM, the Gulf of Mexico is a source of both boundary layer and non-boundary layer moisture. The axis of non-boundary layer moisture continues northward into central Texas and Oklahoma, which the maximum in non-boundary layer moisture occurs just off the coasts of Texas and Mexico. In terms of mass, more boundary layer moisture uptakes occur over the Gulf of Mexico. The maximum is again, just off the Texas coast. The axis of highest moisture increase continues northeastward into the plains of Louisiana and Arkansas.

The bulk of moisture increases for flash floods occurs in JJA. There is an axis of boundary layer and non-boundary layer uptakes oriented from southeast to northwest over the Gulf of Mexico, but the most mass is added to parcels over land. For non-boundary layer uptakes, this occurs throughout the central United States, with a maximum occurring in the SGP. There is a secondary maximum that borders the Gulf of California. Boundary layer uptakes also occur extensively through the central United States, with the maximum also occurring over the SGP. Other maxima include the coastal plains east of the Piedmont region, along the East Coast as well as the Gulf of California itself, indicating the strong seasonal influence of the monsoon.

In SON, the Gulf of Mexico and the states along the Gulf Coast are the regions with the largest non-boundary layer increases in moisture. Boundary layer increases in moisture also occur within the Gulf of Mexico but also off the Atlantic Coast. A small source region for uptakes in the boundary layer exists over the Gulf of California as the North American Monsoon persists into the early fall.

Further discussion in this section will include a region-by-region analysis of the moisture sources and the land surface conditions associated with the boundary layer uptakes.

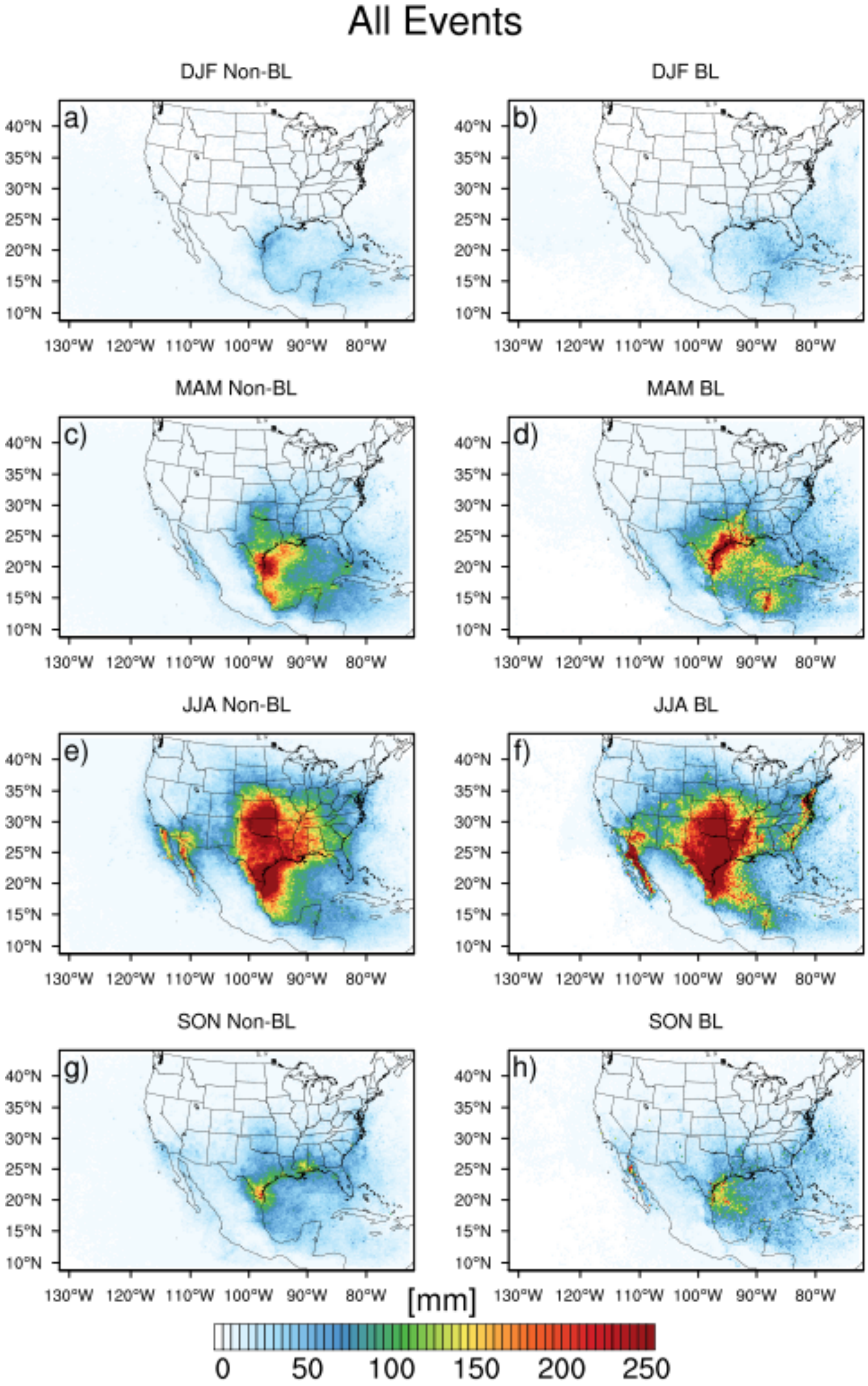

Figure 29: Total boundary layer uptakes and non-boundary layer uptakes by season for all events.

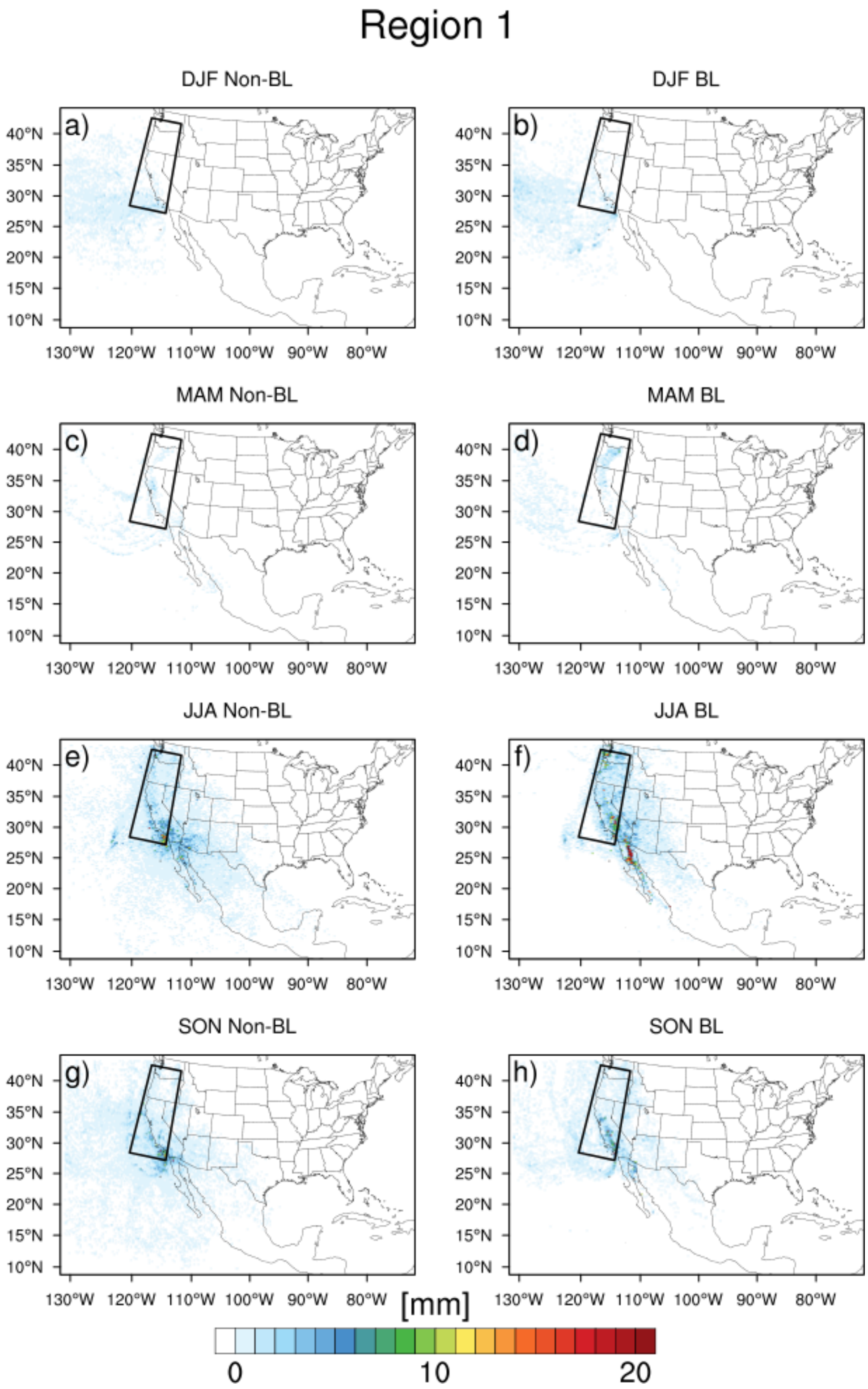

Figure 30. Total boundary layer uptakes and non-boundary layer uptakes by season for Region 1 (West Coast).

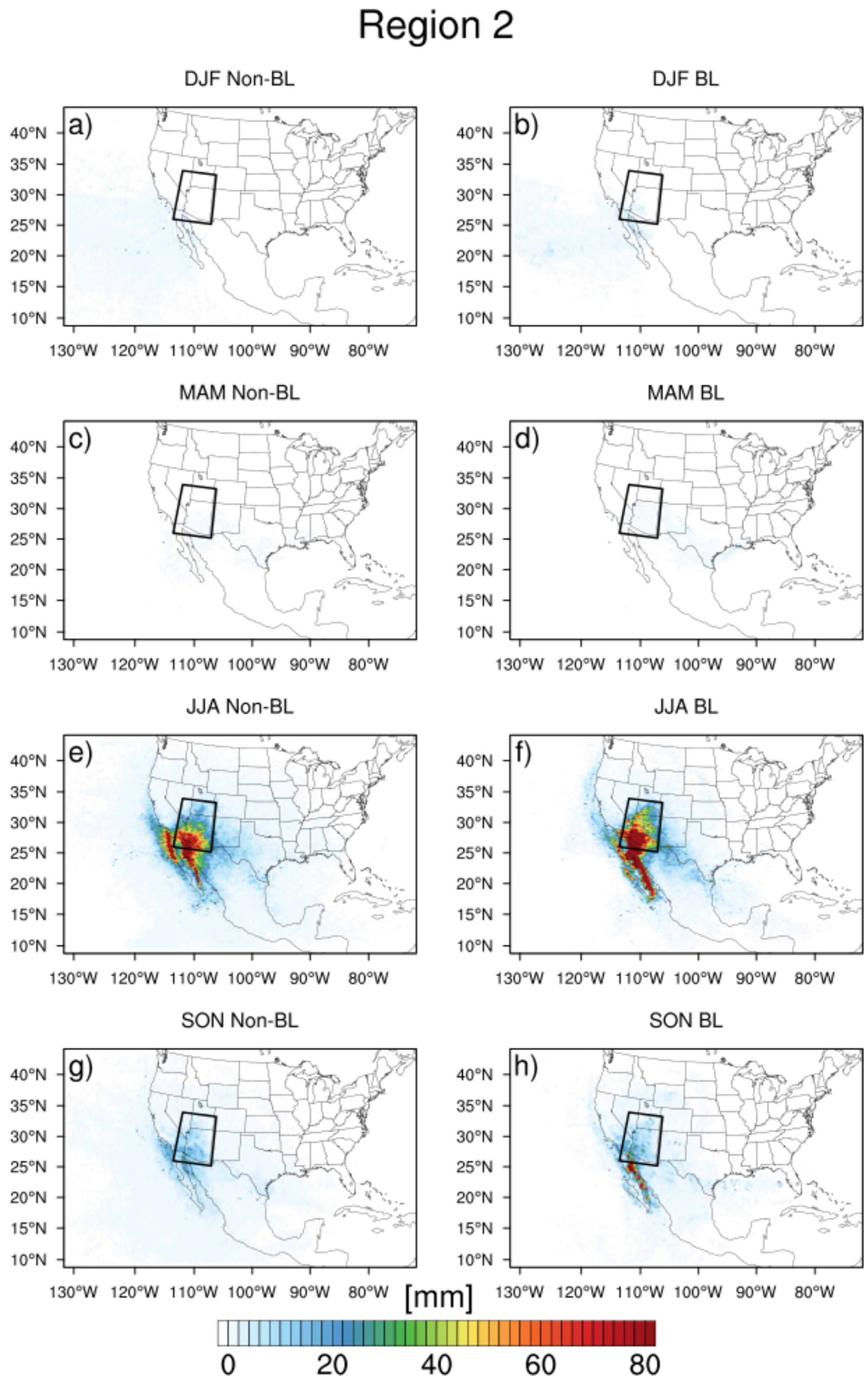

Figure 31. As in Figure 30, but for Region 2 (Arizona).

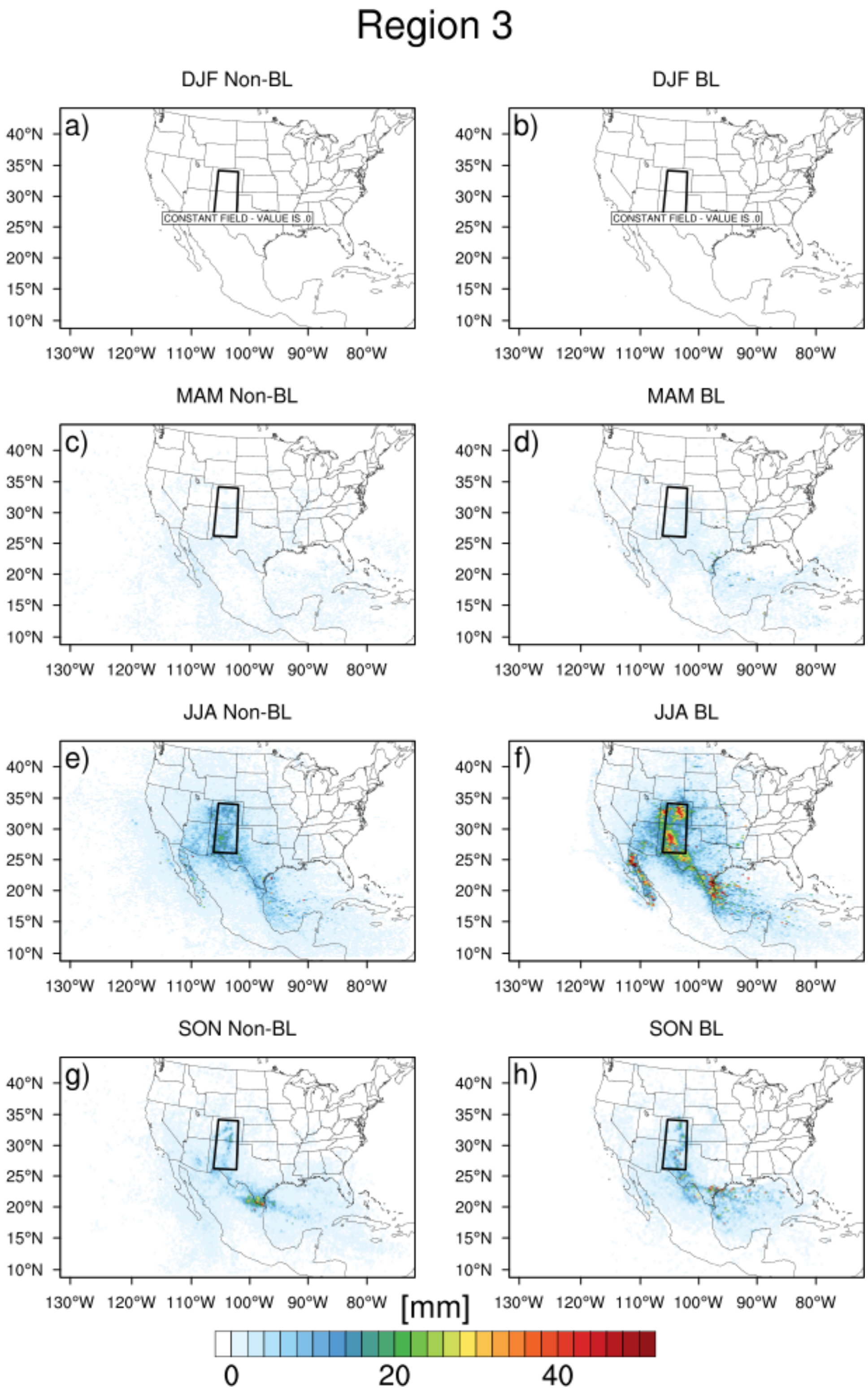

Figure 32. As in Figure 30, but for Region 3 (Front Range).

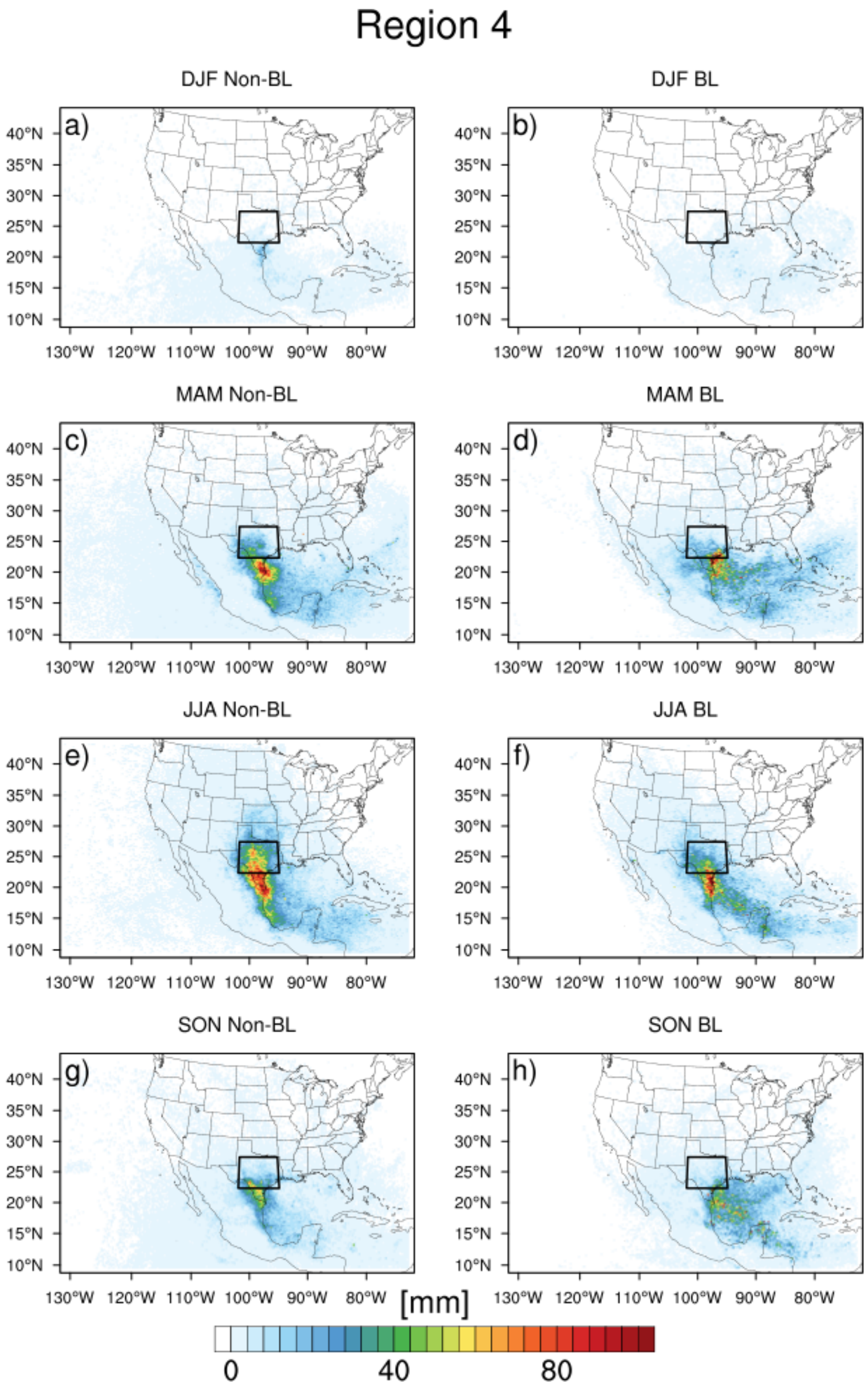

Figure 33. As in Figure 30, but for Region 4 (Flash Flood Alley).

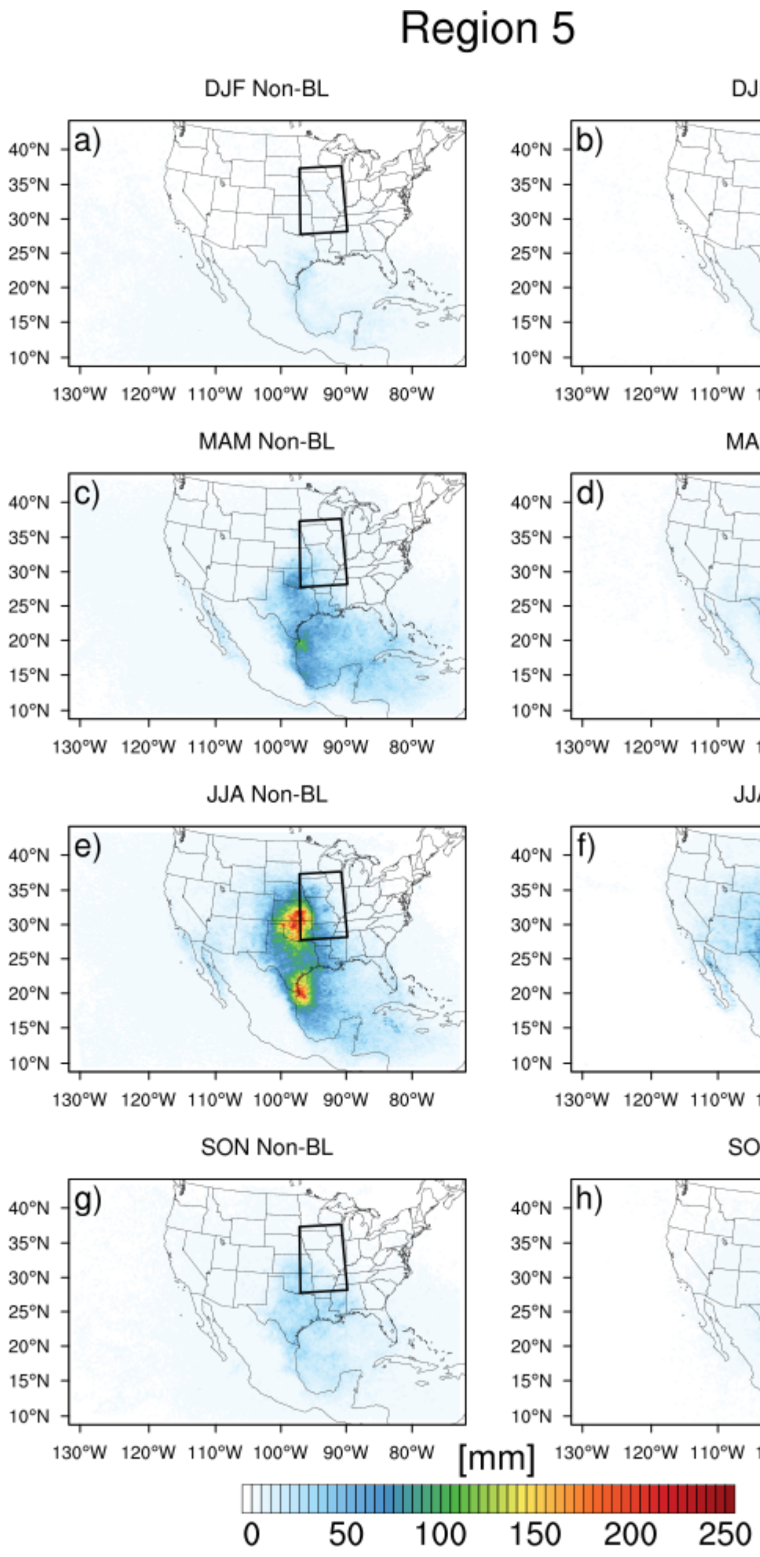

Figure 34. As in Figure 30, but for Region 5 (Missouri Valley).

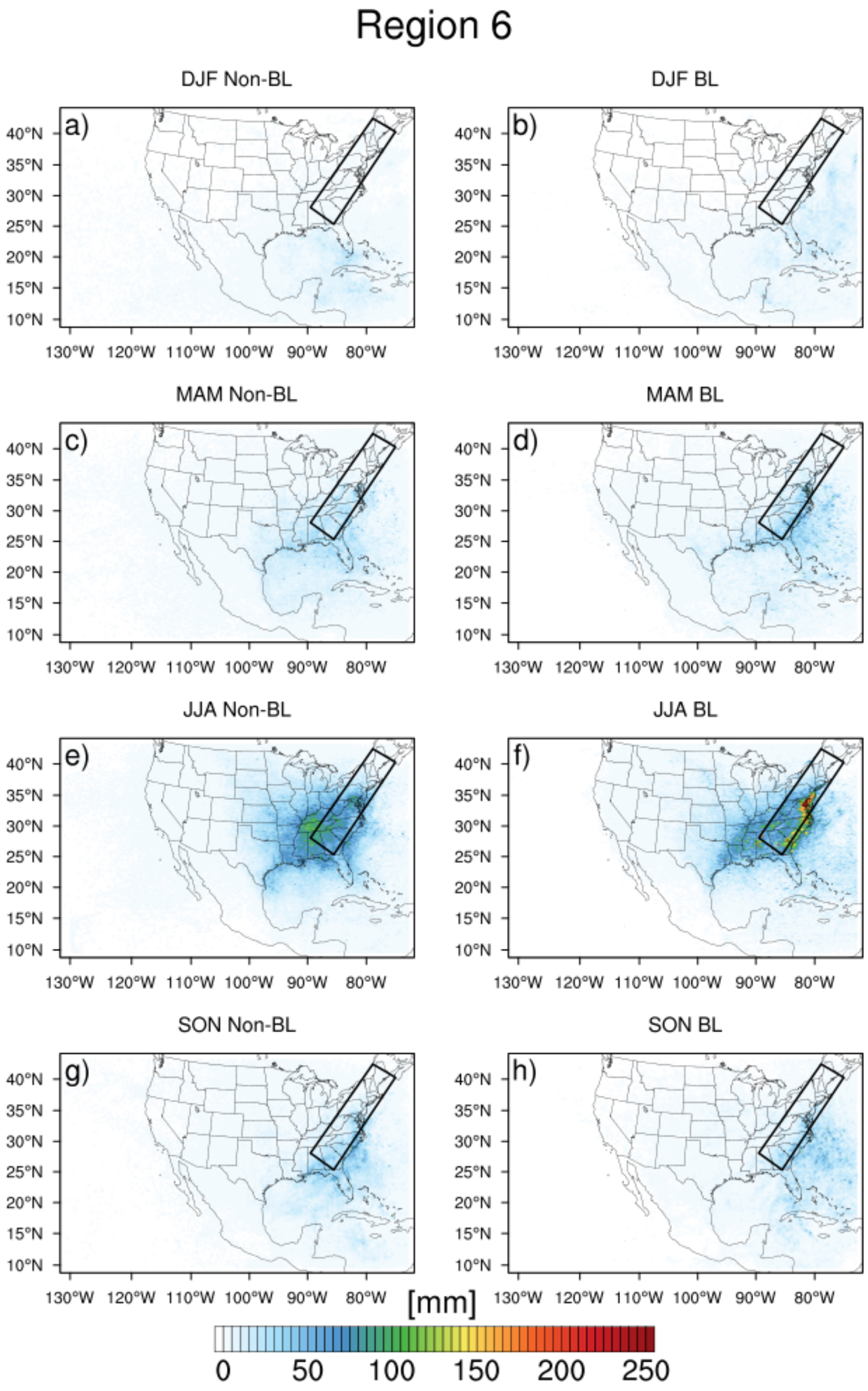

Figure 35. As in Figure 30, but for Region 6 (Appalachians).

For Region 1 (West Coast), boundary layer and non-boundary layer moisture sources are identified over the Pacific Ocean (Figure 30). In MAM, there is a small amount of boundary layer moisture uptakes in northern California as well. In JJA, slight boundary layer uptakes occur over much of the western US, though the largest integrated uptakes are over the Gulf of California as a result of the North American Monsoon. In SON, both boundary layer and non-boundary layer uptakes occur broadly over the western United States.

For Region 2 (Figure 31), the clear source of boundary layer moisture increases during the monsoon season (JJA and SON) is the Gulf of California. Non-boundary layer moisture uptakes occur for the same period in Baja California and along the Mexican coast, as well as within the Gulf of California. During DJF, there are slight increases due to both boundary layer and non-boundary layer sources over the Pacific Ocean.

For Region 3 (Front Range), small boundary layer and non-boundary uptakes occur over the Gulf of Mexico and over Texas, New Mexico, and Arizona (Figure 32). In JJA, there is evidence of contribution of monsoon effects, with the Gulf of California being a large source of boundary layer moisture. Additionally, sources of moisture from the land surface appear to occur locally during JJA, with much of Colorado and New Mexico being a hotspot for boundary layer uptakes. Non-boundary layer uptakes also occur in Colorado, New Mexico and though west Texas, though they of lesser magnitude than the boundary layer uptakes. During SON, boundary layer uptakes occur over the Gulf of Mexico, in western Texas, and in New Mexico and Colorado. Non-boundary layer uptakes also occur in these areas, though the maximum for those contributions is in far southern Texas.

The most important source of boundary layer moisture uptakes is the Gulf of Mexico for Flash Flood Alley (Figure 33). In the spring, moisture uptakes occur along the preferred flow path of parcels, the northern and central parts of the Gulf of Mexico. The largest cumulative moisture increases occur just before the parcels make landfall along the coast of southeast Texas. In the summer, there is a larger contribution relative to spring and fall from the area south of Cuba, but the bulk of the moisture gained by parcels during JJA occurs in the western Gulf of Mexico and as parcels approach the Texas coast. Fall moisture uptakes occur in a similar pattern to the spring uptakes for this region.

Non-boundary layer moisture for Flash Flood Alley occurs in lesser magnitudes over the western Gulf of Mexico in MAM, but most of the mass gained from parcels above the boundary layer occurs as the parcels make landfall over Texas. The same is true for JJA: the bulk of increases occur as the parcels are nearing the Texas coast or are over Texas. The mass of parcels is increased most over south Texas in SON.

For floods occurring over the Missouri Valley, parcels again have boundary layer sources of moisture within the Gulf of Mexico (Figure 34). However, the maximum value for spring mass uptakes occurs along the Texas coastline, with eastern Texas, eastern Arkansas, and Louisiana, all being key moisture sources for floods in this region. This is likely due to the amount of vegetation that begins to grow in this region in the spring (coincident with the maxima in monthly maps of greenness fraction, not shown). The maximum mass uptakes for JJA for the Missouri Valley occur onshore in eastern Texas and Oklahoma into Kansas. This area has been identified as a region where land-atmosphere coupling plays an important role for precipitation episodes. This is also a region where moisture is transported northward via the LLJ. Since there are fewer events in SON for this region, less water vapor is added to parcels, but the area with the largest integrated boundary layer uptakes is again in the northern Gulf of Mexico and into Louisiana and Arkansas.

Non-boundary layer uptakes for Region 5 (Missouri Valley) have two regions where they are maximized in MAM. There is a broad area over the Gulf of Mexico with small contributions, but there are maxima located along the Mexican coast and in southwest Oklahoma. In JJA, again the maxima are near Corpus Christi, TX and north central Oklahoma and south central Kansas. In the fall, there is a broad area of non-boundary layer uptakes over Texas and Oklahoma. Non-boundary layer sources of moisture can be attributed to precipitation evaporating into a column or vertical transport of moisture by convection.

For Region 6 (Appalachian Mountains), boundary layer uptakes occur in the Atlantic Ocean and along the coastal plains in Georgia, the Carolinas, and Virginia (Figure 35). In JJA, the maximum uptakes occur in the coastal regions of the states and further north into the Chesapeake Bay. In JJA, this is also accompanied by a large, weaker area of boundary layer moisture increases in the Southeast, from eastern Arkansas, to the Gulf of Mexico, through Tennessee, Kentucky, and West Virginia. In the fall, the Atlantic Ocean and coastal regions along the eastern seaboard become the primary source regions for boundary layer uptakes of moisture.

In JJA for Region 6, the maximum source for boundary layer moisture is over central Tennessee. In this case, there is not a maximum in moisture uptakes along the coast. In MAM and SON, there is a broad region of lower moisture increases in the Southeast and along the Gulf Stream.

4.2.4 Role of Land-Atmosphere Interactions

The local anomaly of antecedent soil moisture is explored for all events at the center of the 11x11 grid box in time. Beginning from the closest 3-hour time (00, 03, 06 UTC, etc.) after the time of the flood report, the soil saturation was calculated backward in 3-hour increments until t=-30 hours. (Therefore, the flood report occurs sometime in the t=-3h to the t=0h interval for this analysis only.) The saturated values of volumetric soil moisture for each soil type in the STATSGO dataset are given in Table 4.

Table 4. Soil properties in HRLDAS.

	Volumetric Water Content at Saturation Θ_a [m^3m^{-3}]	**Wilting Point Θ_w [m^3m^{-3}]**	**Saturated Hydraulic Conductivity K_{sat} [$m\ s^{-1}$]**
Sand	0.339	0.010	1.07E-6
Loamy Sand	0.421	0.028	1.41E-5
Sandy Loam	0.434	0.047	5.23E-6
Silt Loam	0.476	0.084	2.81E-6
Silt	0.476	0.084	2.81E-6
Loam	0.439	0.066	3.38E-06
Sandy Clay Loam	0.404	0.067	4.45E-6
Silty Clay Loam	0.464	0.120	2.04E-6
Clay Loam	0.465	0.103	2.45E-6
Sandy Clay	0.406	0.100	7.22E-6
Silty Clay	0.468	0.126	1.34E-6
Clay	0.468	0.138	9.74E-7
Organic Material	0.439	0.066	3.38E-6
Water	1.0	0.000	0.0
Bedrock	0.20	0.006	1.41E-4
Other (land-ice)	0.421	0.028	141E-5
Playa	0.468	0.030	9.74E-7
Lava	0.200	0.006	1.41E-4
White Sand	0.339	0.010	1.07E-6

Local soil moisture (in terms of saturation) for two regions is discussed in this section to illustrate of the behavior of antecedent soil moisture both east of the Rocky Mountains (Regions 4-6) and west of and including the Rocky Mountains (Regions 1-

3). Histograms of the antecedent soil moisture for other regions and soil depths are included in Appendix A. This section focuses on top layer (0-10 cm below ground) soil moisture because it showed the most variability among regions. Regions 2 and 4 are shown as examples in Figure 36 and Figure 37, respectively.

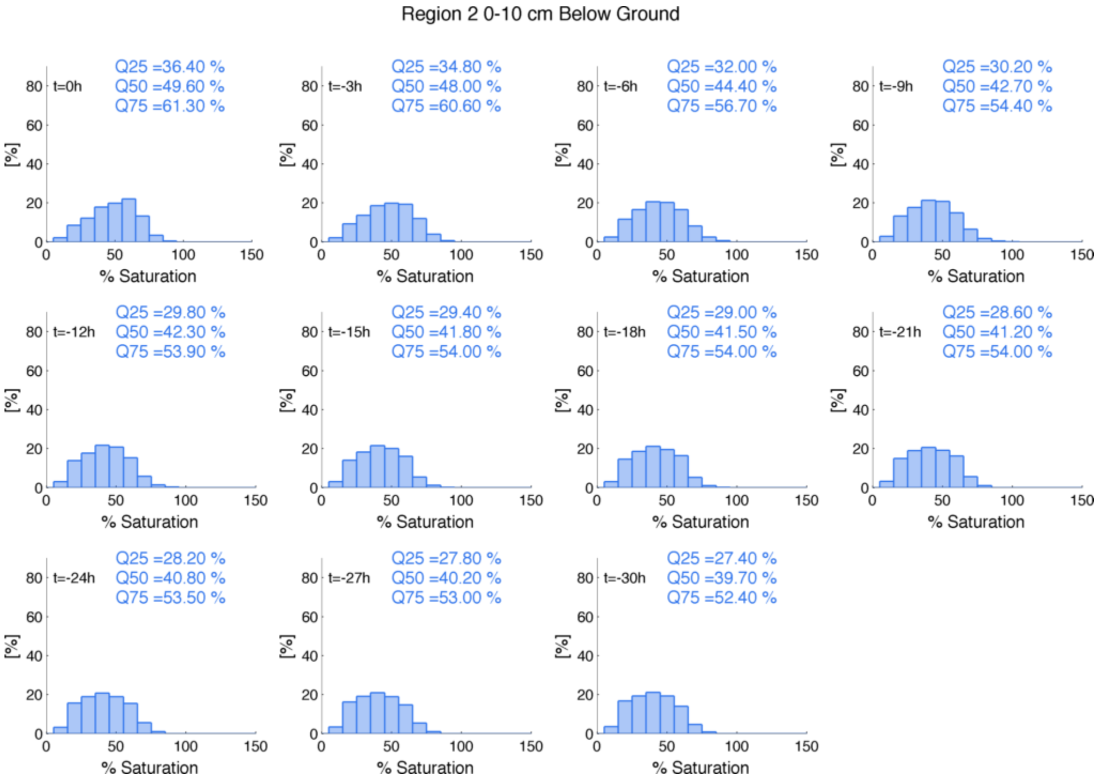

Figure 36. Local soil moisture (saturation) for Region 2 (Arizona) at 3-hour intervals prior to flood time. Quantiles (25th, 50th, and 75th percentiles) of each distribution are marked.

When considering soil saturation in the 11x11 box 24 hours prior to flood time, the arid regions have lower saturation values of 0-10 cm below ground soil moisture than those in humid regions. The median saturation values for 24 hours prior to flood time are as follows: Region 1 30.9%; Region 2 40.8%; Region 3 40.4%; Region 4 55.2%; Region 5 60.5%; Region 6 57.8%. As the time of the flood approaches, there is an increase in saturation for all regions, but humid regions increase more. Six hours prior to the flood time, median top layer soil moisture values are as follows: Region 1

37.4%; Region 2 44.4%; Region 3 44.0%; Region 4 72.8%; Region 5 71.3%; Region 6 67.5%. For humid regions, the 75th percentile local soil moisture six hours prior to the event is ~80%, whereas in Regions 2 and 3, it is ~55%. The exception is Region 1, which develops a bimodal distribution of soil moisture prior to the event.

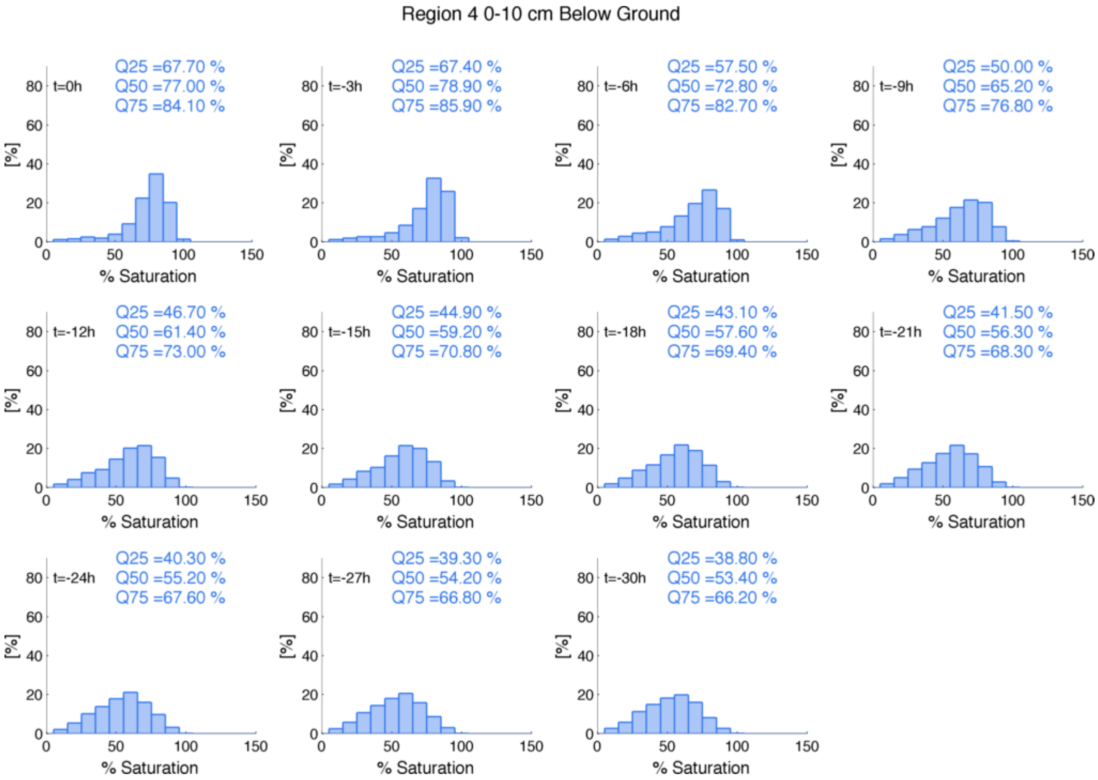

Figure 37. As in Figure 36, but for Region 4 (Flash Flood Alley).

This analysis illustrates some differences in flood generating mechanisms between humid and arid regions. Arid regions show less saturation ahead of the flood time, implying that runoff is generated because of infiltration excess. In humid regions, however, soil saturation steadily increases prior to the flood time, indicating a greater importance of antecedent rainfall and saturation excess as a mechanism for runoff generation.

While many other studies examine the local relationship between antecedent soil moisture, the methodology used here also allows for the interrogation of land surface conditions following the path of the parcels that contributed to flash flood inducing rainfall. The along-trajectory component of soil moisture anomalies is a novel contribution of this study. Climatologies of soil moisture at four levels in the soil column (0-10 cm below ground, 10-40 cm below ground, 40 cm-1 m below ground, and 1-2 m below ground) were computed for each month. The anomalies are presented as the ratio of the modeled soil moisture to the climatology.

Climatologies of sensible and latent heat fluxes were generated from the HRLDAS simulation at 3-hourly intervals for each month. For example, a latent heat flux climatology for 1800 UTC in June would contain mean values at 1800 UTC from all 1800 UTC hours in the month of June from 2007-2013. Over the oceans, flux climatologies were calculated from NARR data instead of HRLDAS data, since HRLDAS does not simulate the oceans.

The along-trajectory sensible and latent heat flux anomalies were calculated. In these cases, pixels with five events or more are retained to reduce noise in the data. (Including all pixels leads to extrema when only one data point is present for a grid cell.) The data at uptake points were also analyzed in terms of evaporative fraction, defined as the ratio of latent heat to the available energy of the land surface:

$$EF = \frac{LH}{LH + SH} \tag{62}$$

The evaporative fraction shows how the available energy at the surface is partitioned. Evaporative fractions that approach 1 indicate that available energy is used for evaporation, whereas evaporative fractions that approach 0 indicate that available energy is transferred from the surface to the atmosphere as heat. Additionally, anomalies in evaporative fraction (computed as departures from the evaporative fraction climatology computed from latent and sensible heat fluxes at each hour for each month) were examined at each point a boundary layer uptake occurred. Concurrently analyzing anomalies in surface fluxes along with how they are partitioned (evaporative fraction) describes the state of the land surface more fully. For example, if surface latent heat fluxes are anomalously large and surface sensible heat fluxes are also anomalously large, the anomaly may be due to increased radiative forcing (e.g., a clear, sunny day in an area where it is usually cloudy in the climatology), which does not affect the partitioning of the available energy at the land surface. If surface latent heat fluxes are anomalously large and sensible heat fluxes are anomalously small at a point, then the evaporative fraction also contains a positive anomaly, and this is a case of increased surface evaporation.

In a similar fashion, Sea Surface Temperature (SST) anomalies were computed relative to the NARR long-term average (1979-2008 monthly mean) at each point a boundary layer uptake occurred. The following figures summarize the character of the land surface at the location of boundary layer uptakes. Locations with 5 or more uptakes are plotted to reduce artificial extrema that occurred when fewer than 5 points were averaged. Anomalies of fluxes, evaporative fraction, and SST are computed as departures from normal.

The timing of boundary layer uptakes was first investigated by region and by season for both land pixels and ocean pixels. The distributions for UTC time of ocean uptakes remained relatively flat, with 10-15% of uptakes occurring for any given three-hour interval. Pixels over land, however, showed more variability with the diurnal cycle of solar forcing, with less than 10% of uptakes occurring in the early morning, and 20%

or more occurring in each of the afternoon hours. This was a consistent pattern across regions and seasons. The distributions are shown as an example for Region 5 (Missouri Valley) in Figure 38.

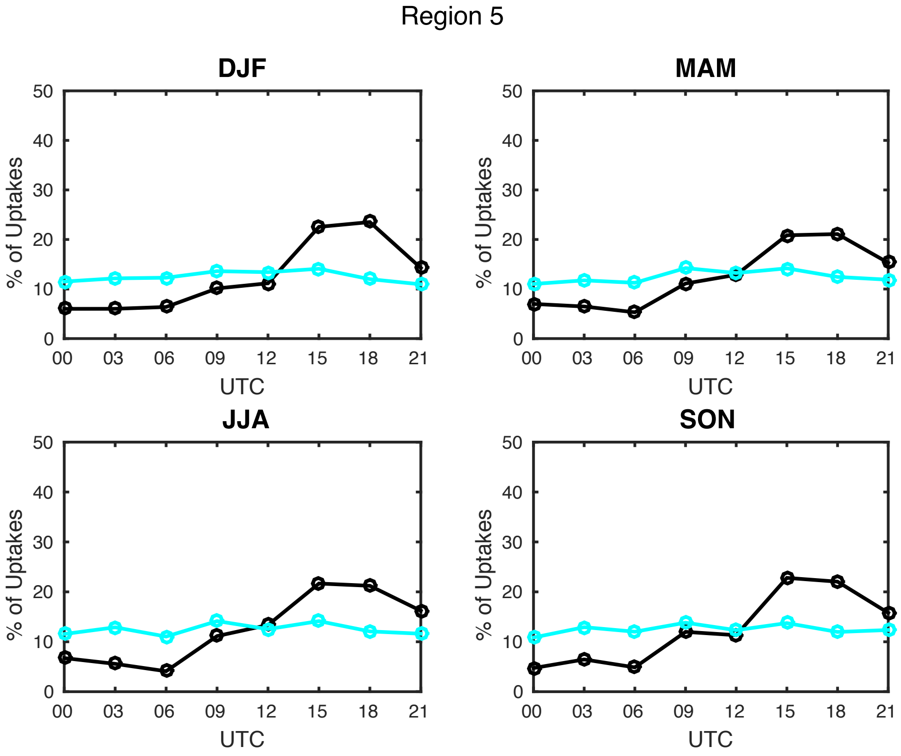

Figure 38. Relative frequency histograms for boundary layer uptakes occurring for Region 5 (Missouri Valley) floods. Boundary layer uptakes over the ocean are shown in cyan, while boundary layer uptakes over land are shown in black.

For the West Coast (Figure 39), there are slight positive latent heat flux anomalies in central California, over the Gulf of California, and in Nevada in JJA and SON, respectively. These areas correspond with slight negative sensible heat flux anomalies. This indicates that, within the confines of this study domain, that the moisture for flash floods on the West Coast is transported with little modification by the land surface.

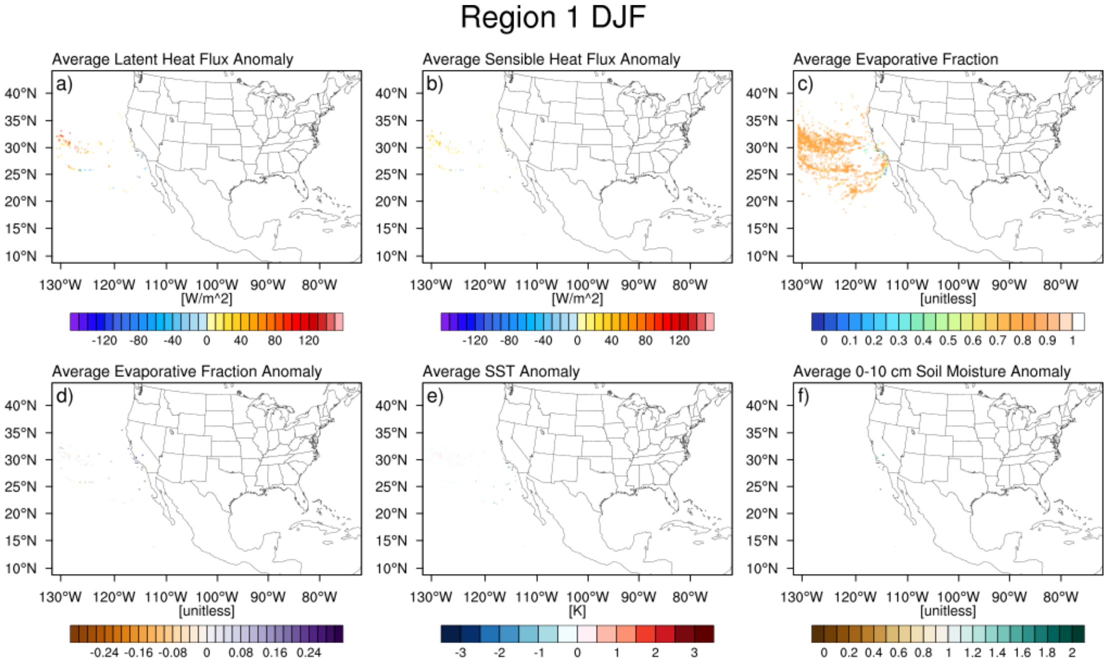

Figure 39. Average a) latent heat flux anomalies [Wm^{-2}] b) sensible heat flux anomalies [Wm^{-2}] c) evaporative fraction d) evaporative fraction anomalies e) SST anomalies and f) top layer (0-10 cm below ground) soil moisture anomalies for boundary layer uptakes for the West Coast (Region 1) in DJF.

For the monsoonal region (Region 2), latent heat flux anomalies occur in the Gulf of California in JJA (Figure 40a). In SON, these anomalies occur over the Southwest as well as over the Gulf of California (Figure 41a). Sensible heat fluxes are anomalously low over the Southwest during these two seasons except over the Gulf of California (Figure 40-Figure 41b). These anomalous fluxes are spatially correlated with warm SSTs (> 0.5K above average) in the Gulf of California in JJA (Figure 40e). Over the Southwest, evaporative fractions range generally from 0.2-0.5, whereas over the water, they approach 1.0 (Figure 40-Figure 41c). However, over the Gulf of California, the fluxes are not anomalously partitioned, but there are slight positive anomalies in evaporative fraction over the Southwest in JJA, and larger evaporative fraction anomalies in Arizona, southern California, southern Nevada, and southern Utah (Figure 40-Figure 41d). Soil moisture is anomalously large over the same region (Figure 40-

Figure 41f), contributing to larger than normal surface evaporation and latent heat fluxes.

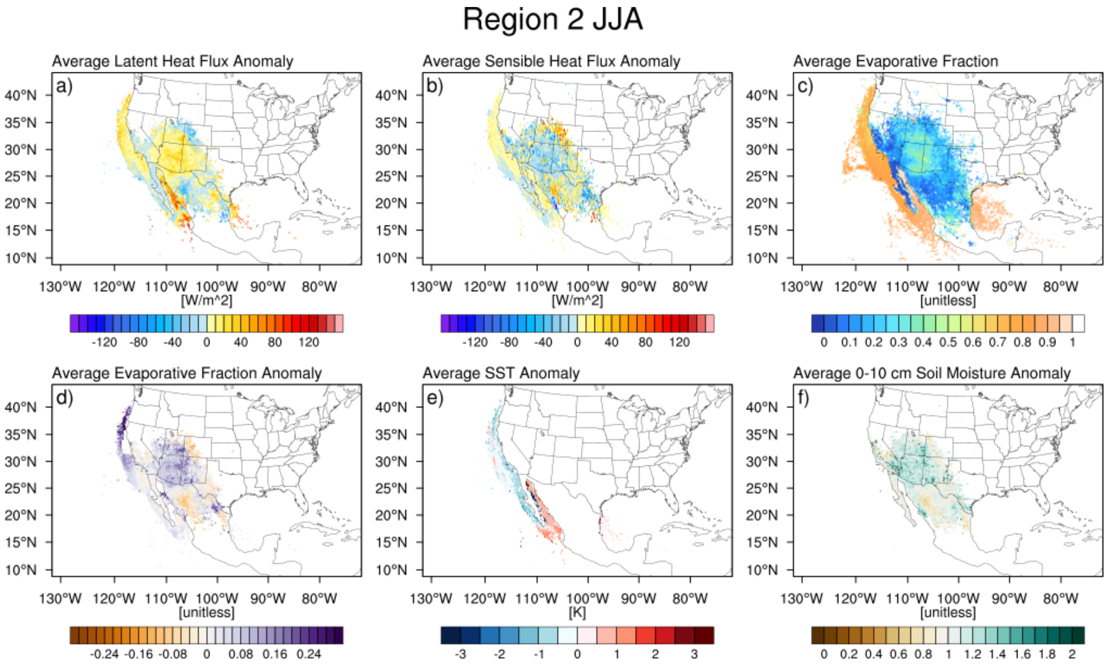

Figure 40. As in Figure 39, but for Region 2 (Arizona) during JJA.

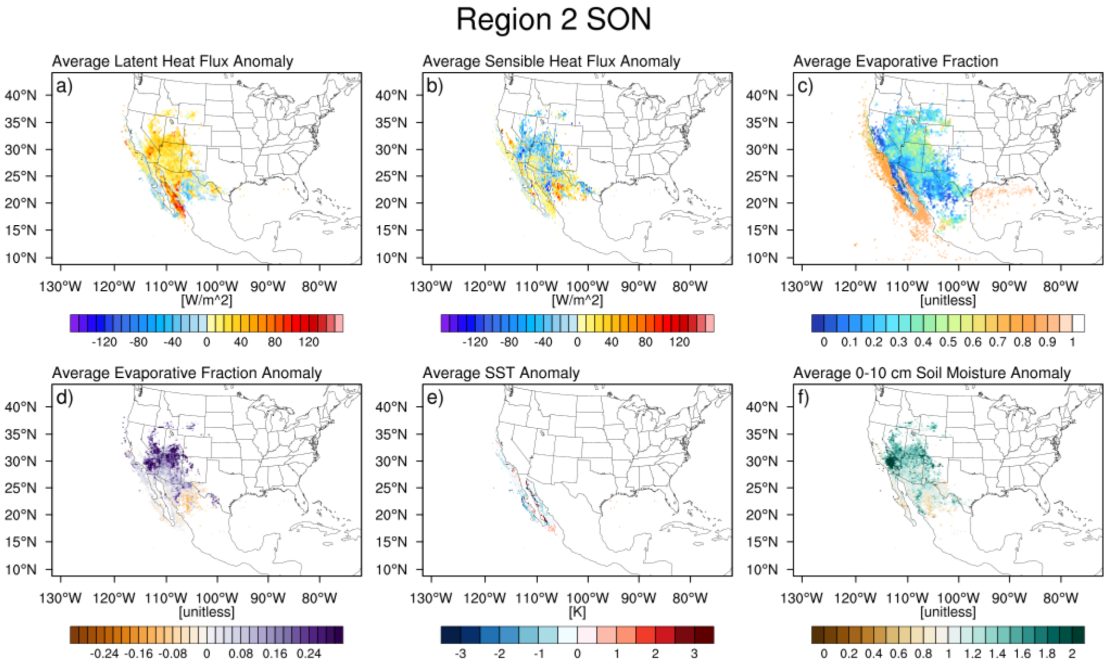

Figure 41. As in Figure 39, but for Region 2 (Arizona) during SON.

Flash floods occurring along the Front Range (Region 3) have a climatological maximum in JJA (Figure 42). Slight positive anomalies in surface latent heat fluxes where boundary layer uptakes occur are present over much of the SGP and Southwest as well as portions of the western Gulf of Mexico and Gulf of California. These anomalies are largest in central Texas, eastern Oklahoma and central Kansas, where they are also accompanied by negative anomalies in surface sensible heat fluxes. Over Oklahoma and Kansas, evaporative fractions exceed 0.6. The partitioning of surface fluxes is also anomalous, with positive anomalies in evaporative fraction occurring over this region as well. Positive SSTs are present in the Gulf of California for JJA. The combination of anomalous latent heat fluxes and higher than normal SSTs in the Gulf of California indicate that some summer floods along the Front Range have similar signatures in land-atmosphere interactions as the North American Monsoon, whose patterns of surface flux and SST anomalies were discussed for the previous region. The land areas with the largest latent heat flux anomalies also contain large top layer soil moisture anomalies (> 150% of normal). Additionally the low-level flow in Figure 18-Figure 19 indicated a western branch for some events that passes over the Gulf of California.

Positive SSTs also occurred off the Texas coast for flash floods occurring in SON for the Front Range (Figure 43). An arc collocated of large positive latent heat flux anomalies, negative sensible heat flux anomalies, positive evaporative fraction anomalies, and positive soil moisture was present along the flow over northern Mexico, through New Mexico and into eastern Colorado.

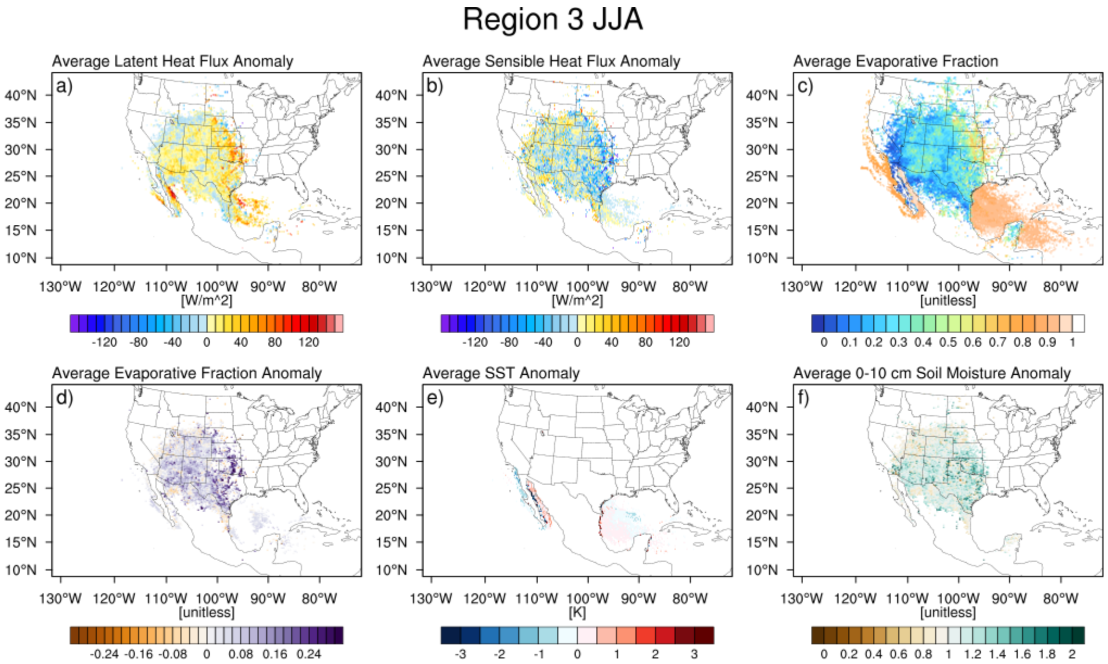

Figure 42. As in Figure 39, but for Region 3 (Front Range) during JJA.

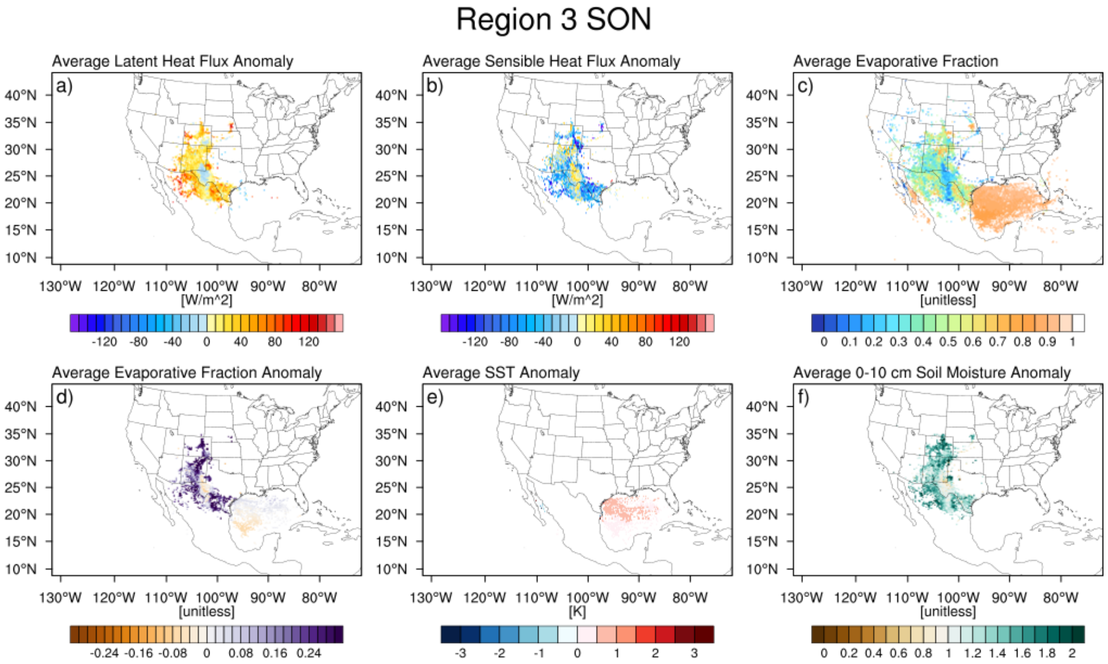

Figure 43. As in Figure 39, but for Region 3 (Front Range) during SON.

In Flash Flood Alley (Region 4), most flash floods occur in MAM (Figure 44) and JJA (Figure 45). For boundary layer uptakes for floods occurring in MAM, there are very large latent heat flux anomalies in the northern Gulf of Mexico, accompanied by slight positive anomalies in sensible heat flux. Over land, there are large positive latent heat flux anomalies over most of Texas, collocated with negative sensible heat flux anomalies. With evaporative fractions greater than 0.5 in magnitude, this also results in a positive evaporative fraction anomaly. SST anomalies are neutral in the Gulf of Mexico, but top positive layer soil moisture anomalies accompany the anomalies in latent heat fluxes, signifying that anomalous evaporation is occurring from wet soils in Texas.

During JJA, there is a large swath of positive latent heat flux anomalies over the Gulf of Mexico, but this axis has shifted south and west, reflecting the prevalent flow pattern. These are accompanied by mostly neutral sensible heat flux anomalies. Over land, however, there are strongly negative sensible heat flux anomalies that are collocated with large positive latent heat flux anomalies over the Balconces Escarpment specifically. Here, evaporative fractions are above 0.6 and are highly positively anomalous. Additionally, there are positive anomalies in SSTs in the central Gulf of Mexico and Caribbean Sea in JJA as well as positive soil moisture anomalies over Mexico, New Mexico, and Texas.

During SON (Figure 46), there are positive latent heat flux anomalies for boundary layer uptakes occurring over the Gulf of Mexico, as well as positive sensible heat flux anomalies and warm SST anomalies throughout the Gulf of Mexico. Over land, the anomalies in surface fluxes are less widespread than in MAM and JJA, but there still remain some positive latent heat flux anomalies, negative sensible heat flux anomalies, and positive evaporative fraction anomalies over central Texas.

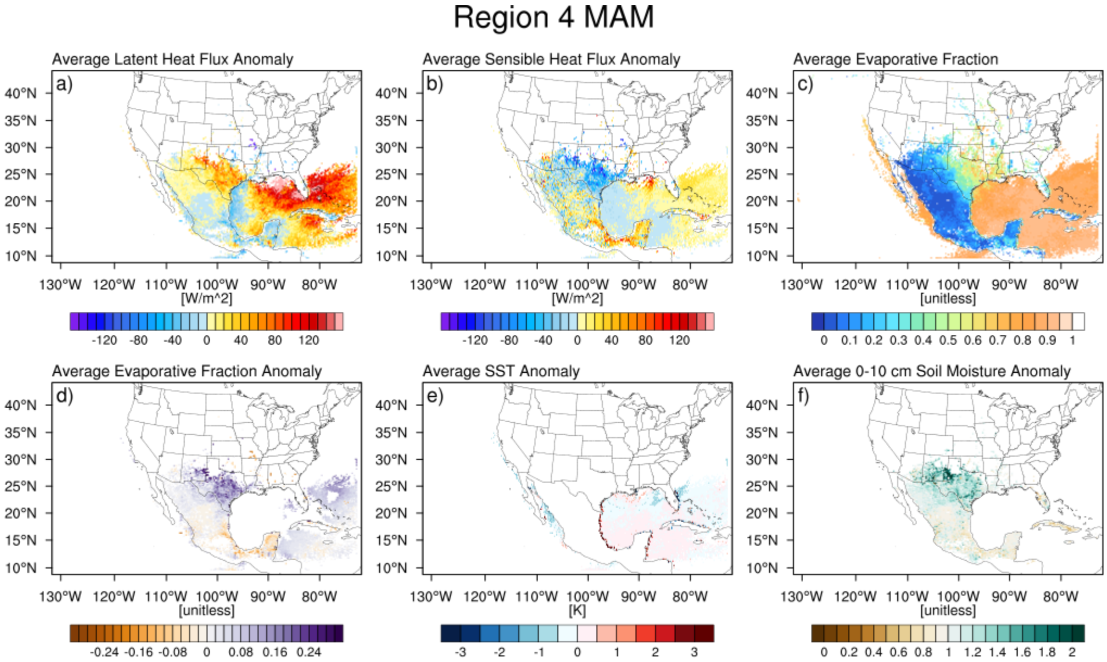

Figure 44. As in Figure 39, but for Region 4 (Flash Flood Alley) during MAM.

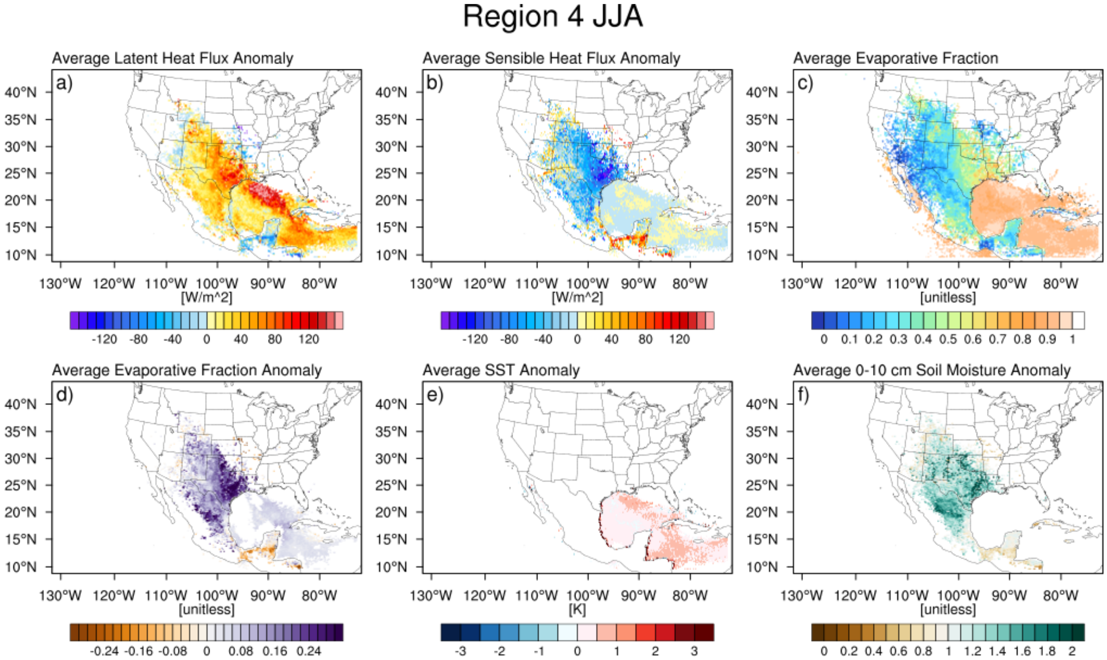

Figure 45. As in Figure 39, but for Region 4 (Flash Flood Alley) during JJA.

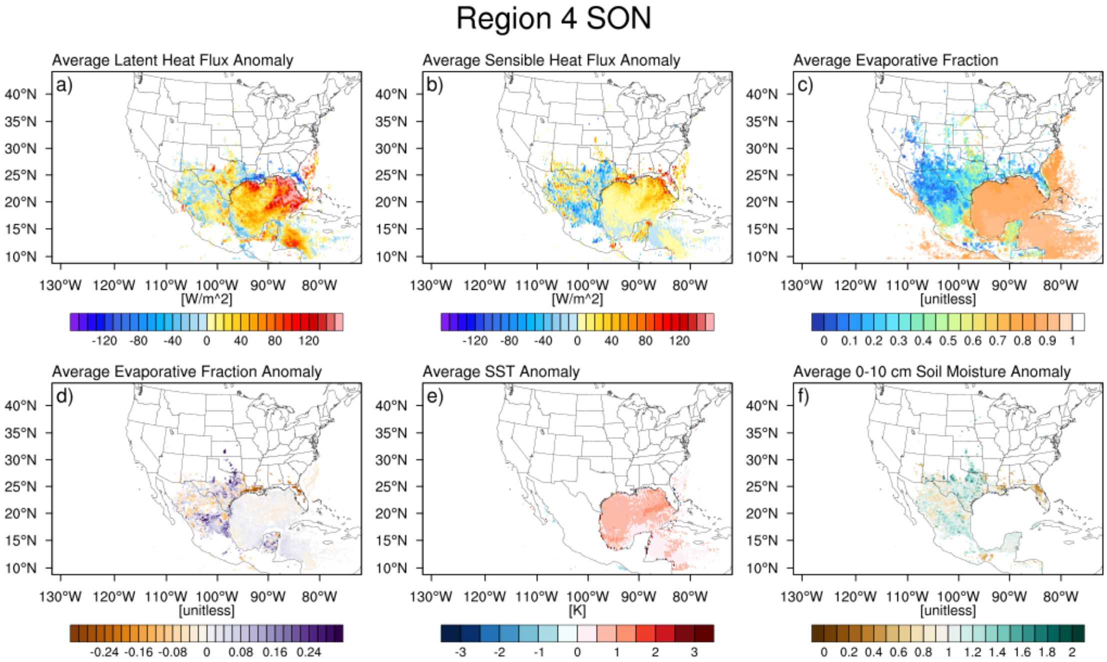

Figure 46. As in Figure 39, but for Region 4 (Flash Flood Alley) during SON.

Flash floods during the warm season in the Missouri Valley (Region 5) are characterized by anomalies in surface fluxes and the largest average evaporative fractions over land in large areas of the CONUS. For boundary layer uptakes for floods occurring in MAM, the largest latent heat fluxes occur in the Gulf of Mexico and Atlantic Ocean off the Florida coasts (Figure 47). Over land, there are positive latent heat flux anomalies over Texas, Oklahoma, Kansas, Missouri, Arkansas, and Missouri, all of which are accompanied by negative sensible heat flux anomalies, and positive anomalies in evaporative fraction. There are slight positive anomalies in SST along the flow south of Florida and generally neutral top layer soil moisture anomalies over the CONUS.

During summer (JJA), latent heat flux anomalies for boundary layer uptakes persist in the Gulf of Mexico off the coasts of Florida and Alabama and in the Caribbean Sea (Figure 48). The maximum in latent heat flux positive anomalies, however, shifts northward, and is centered over Nebraska, Iowa, eastern Kansas, and western Missouri. Again, these positive anomalies are collocated with negative anomalies in sensible heat fluxes, resulting in positive evaporative fraction anomalies. Over Iowa, Missouri, Illinois, and eastern Kansas, evaporative fractions exceed 0.6, indicating that most of the available energy at the surface is used for evaporation. Additionally, there are slight positive anomalies in soil moisture, but these are not as anomalous as those that occurred in western regions.

During SON (Figure 49), positive latent heat flux anomalies are present in the northern Gulf of Mexico, off the coasts of the Carolinas, and in the Caribbean Sea. In the case of the Atlantic Ocean, these are also regions of abnormally high latent heat fluxes and SSTs. The maximum in latent heat fluxes over land shifts southward to Missouri, Kansas, Oklahoma, and Arkansas, and this is a region of negative anomalies in surface sensible heat fluxes and positive anomalies in evaporative fraction. Additionally, in Missouri, there are positive top layer soil moisture anomalies.

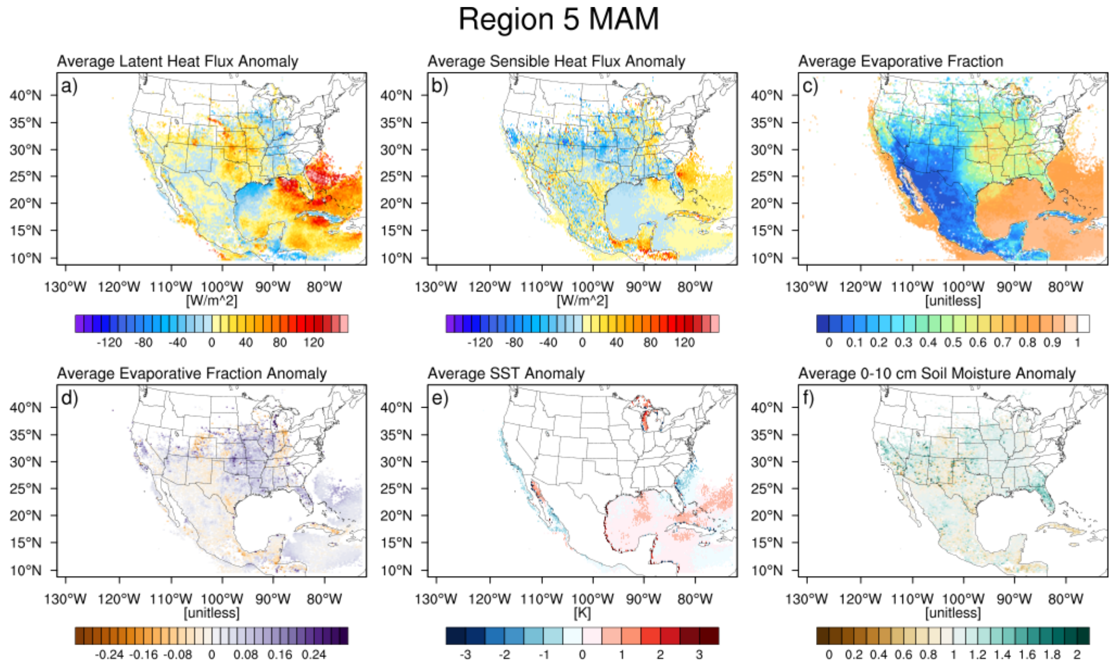

Figure 47. As in Figure 39, but for the Missouri Valley (Region 5) during MAM.

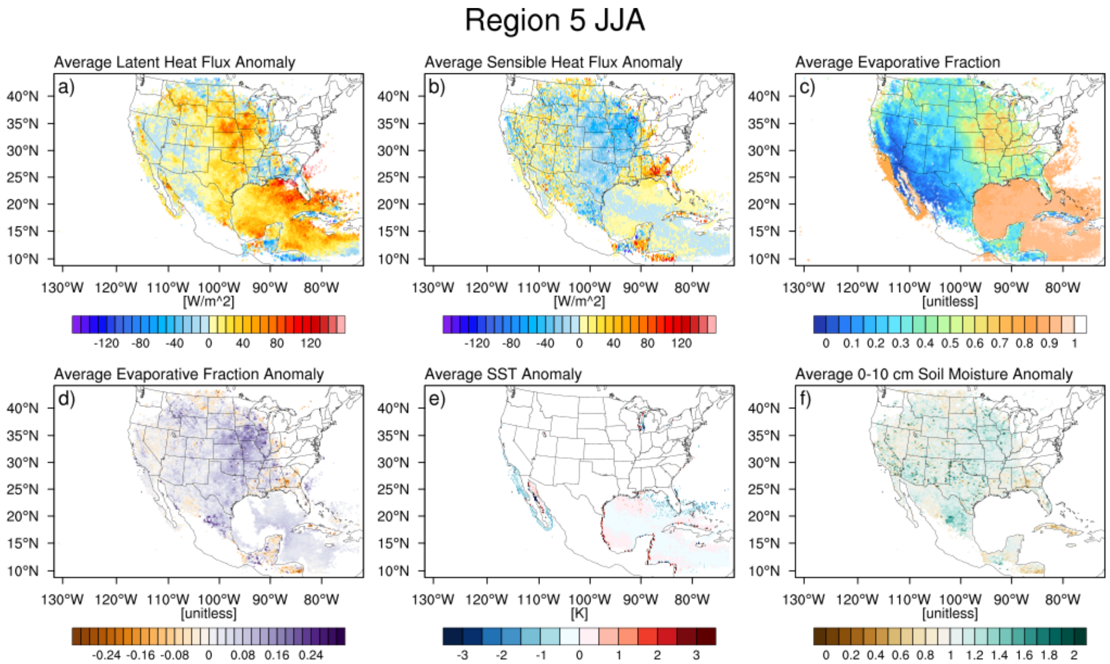

Figure 48. As in Figure 39, but for the Missouri Valley (Region 5) during JJA.

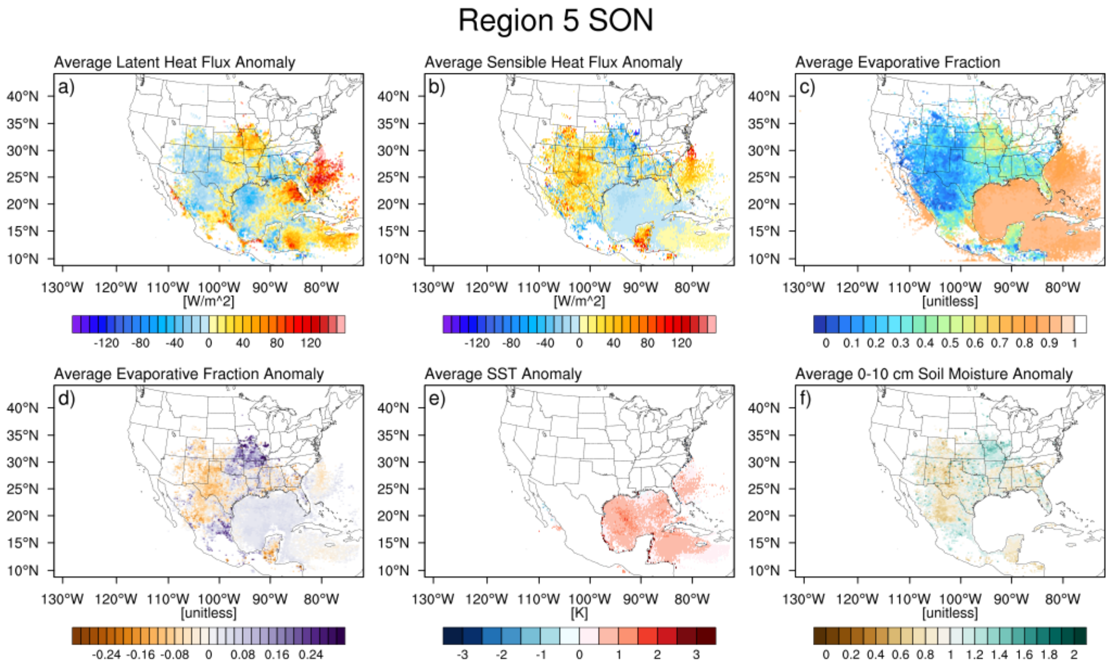

Figure 49. As in Figure 39, but for the Missouri Valley (Region 5) during SON.

Floods occurring along the Appalachians are associated with anomalously high latent heat fluxes in the Northeast and in the Atlantic during MAM (Figure 50). Over land, these regions are also associated with negative sensible heat flux anomalies and positive anomalies in evaporative fraction. Positive anomalies in SST occur along the East Coast, but average top layer soil moisture anomalies are neutral in MAM.

During summer, there are again positive latent heat flux anomalies in the Atlantic Ocean and Gulf of Mexico, the largest of which are collocated with slight sensible heat flux anomalies and warmer than average SSTs (Figure 51). Great Lakes temperatures are also warmer than average. Large values of evaporative fraction are present in Kentucky and Tennessee and northeastward through New England, and there are slight positive anomalies nearly everywhere east of the Mississippi, though soil moisture anomalies are neutral.

In SON, there are positive SST anomalies in the Gulf of Mexico in addition to those off the East Coast, collocated with areas of highly anomalous latent and sensible heat fluxes (Figure 52). Given that tropical cyclones (or extratropical cyclones that had their start as tropical cyclones) are a key driver of flooding in this region, it is unsurprising to see warm SSTs in the Gulf of Mexico during hurricane season in the Atlantic basin. Over land, large latent heat fluxes and low sensible heat fluxes lead to evaporative fraction anomalies in the mid-Atlantic, though the pattern is reversed over Iowa and Illinois. Again, for this region, top layer soil moisture is not especially anomalous, though there are positive anomalies along the East Coast, and slight dry anomalies in Iowa, Illinois, and Missouri.

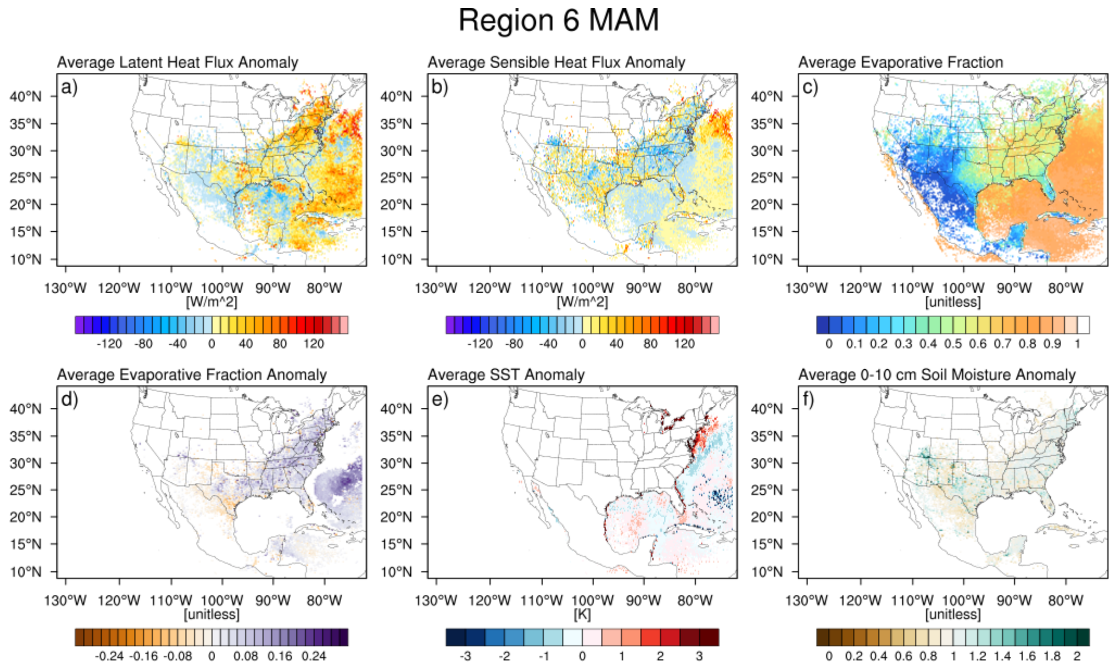

Figure 50. As in Figure 39, but for the Appalachians (Region 6) during MAM.

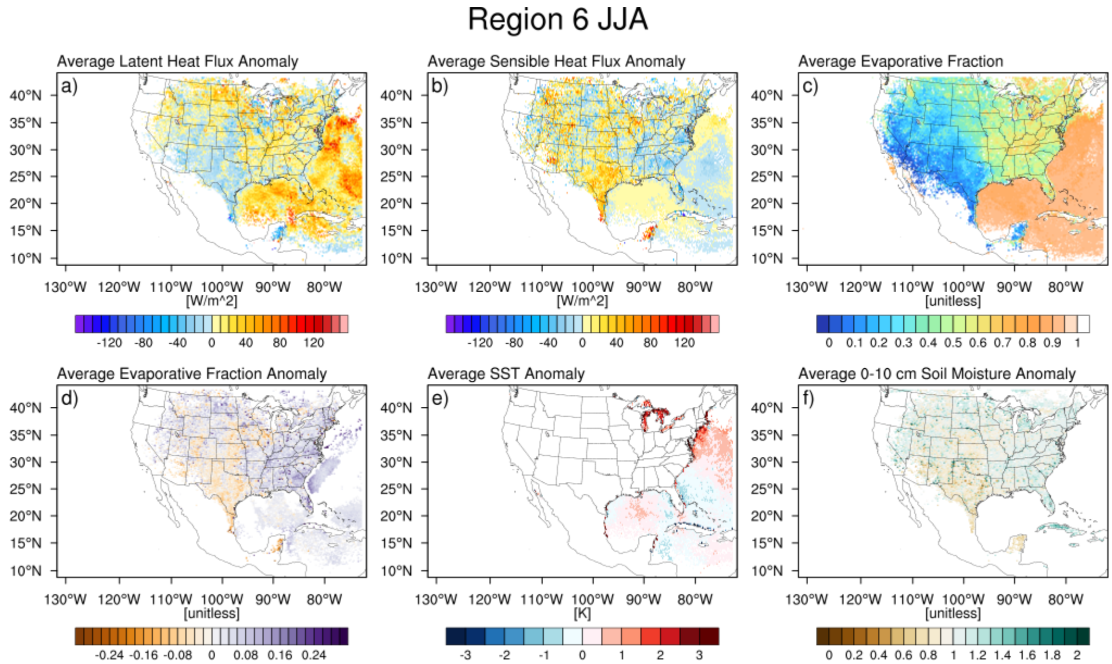

Figure 51. As in Figure 39, but for the Appalachians (Region 6) during JJA.

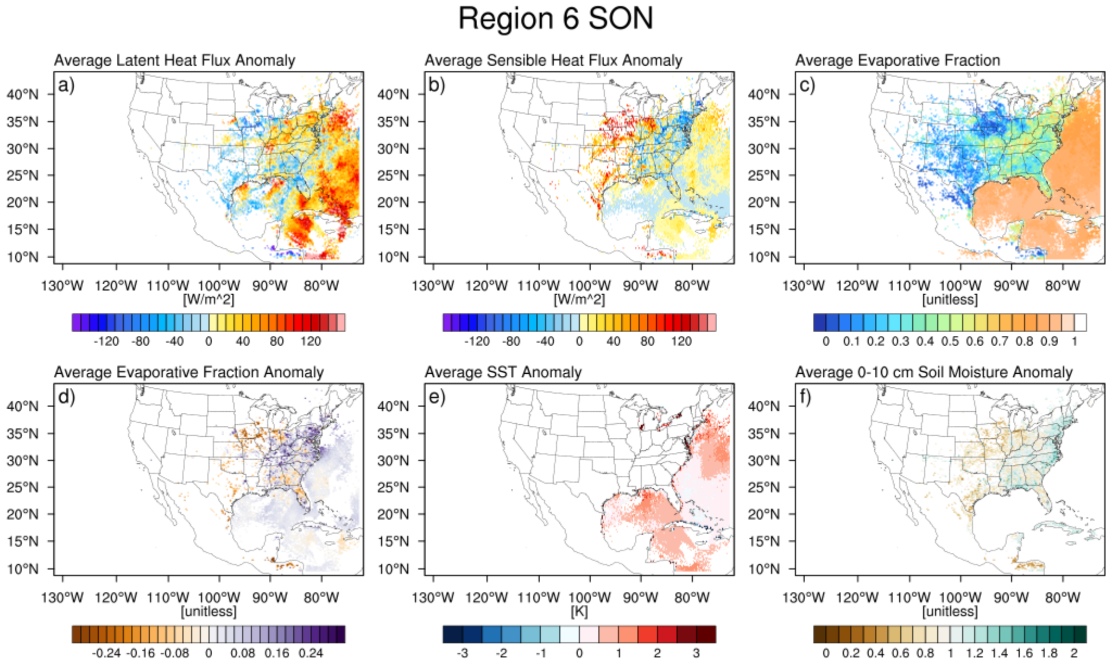

Figure 52. As in Figure 39, but for the Appalachians (Region 6) during SON.

The relationship between evaporative fraction and the change in parcel specific humidity was also examined separately over land and water pixels both regionally and seasonally. Because the change in water pixels only depends on temperature and properties of the atmosphere above (that is, the surface is always saturated), it is expected that water pixels have high evaporative fractions independent of the change in specific humidity of the parcel above them. Since there is a wider range of realizations of the land surface properties, the change in parcel specific humidity is expected to vary with the partitioning of the fluxes at the land surface.

The prior assumption about the relationship between changes in specific humidity and evaporative fraction over the ocean holds true. In all regions and seasons, contour plots of frequency show a relatively flat distribution of evaporative fractions of 0.8 or larger for a variety of uptake magnitudes. Figure 53 shows an example of this behavior for Region 5 (Missouri Valley).

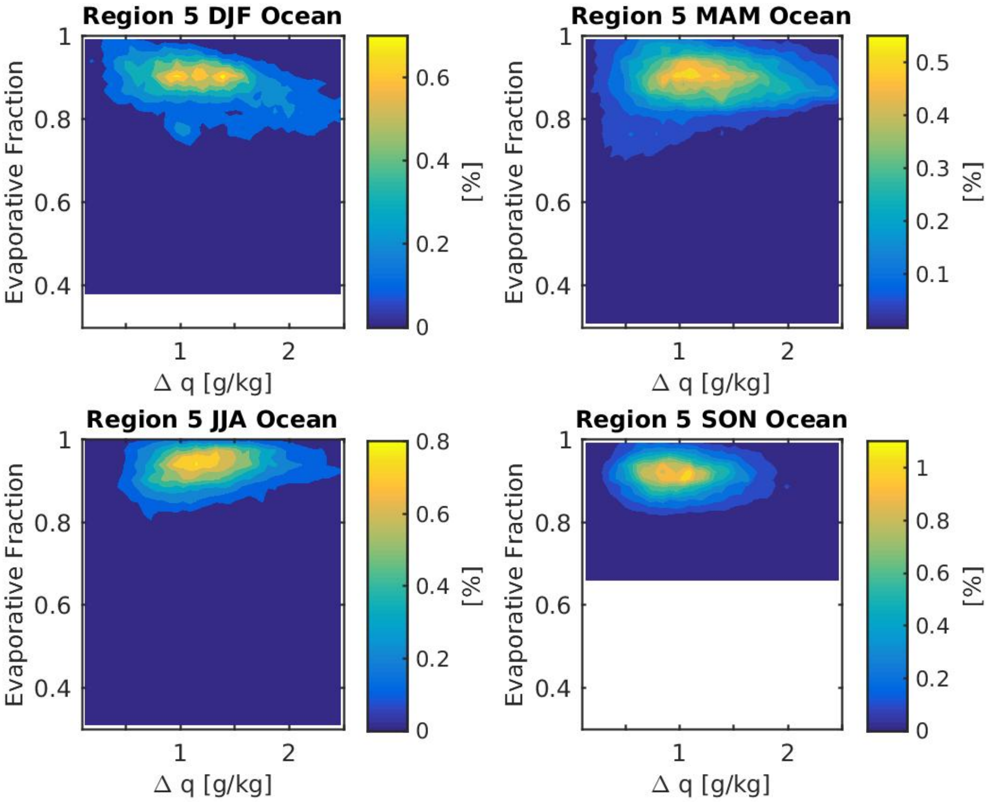

Figure 53. Relative frequency contour plots for boundary layer uptakes over ocean pixels for floods occurring in Region 5 (Missouri Valley).

Over land, however the relationship between the magnitude of boundary layer uptake and evaporative fraction is positive. That is, with increasing evaporative fraction (more incoming radiation partitioned into latent heat flux/evaporation), the magnitude of boundary layer uptake increases. The slope of the relationship appears to depend on the geographic location of the uptakes. For more arid regions (e.g., Region 2), where many of the uptakes occur over climatologically drier areas, the evaporative fraction for a given uptake is smaller. For floods occurring in more humid regions (e.g., Region 5), evaporative fraction is larger for a given uptakes. Uptakes of large magnitudes also occur for floods in more humid regions. The maximum increase in specific humidity appears to have an upper limit of 1.5 g kg^{-1}, though the corresponding range of evaporative fractions is larger.

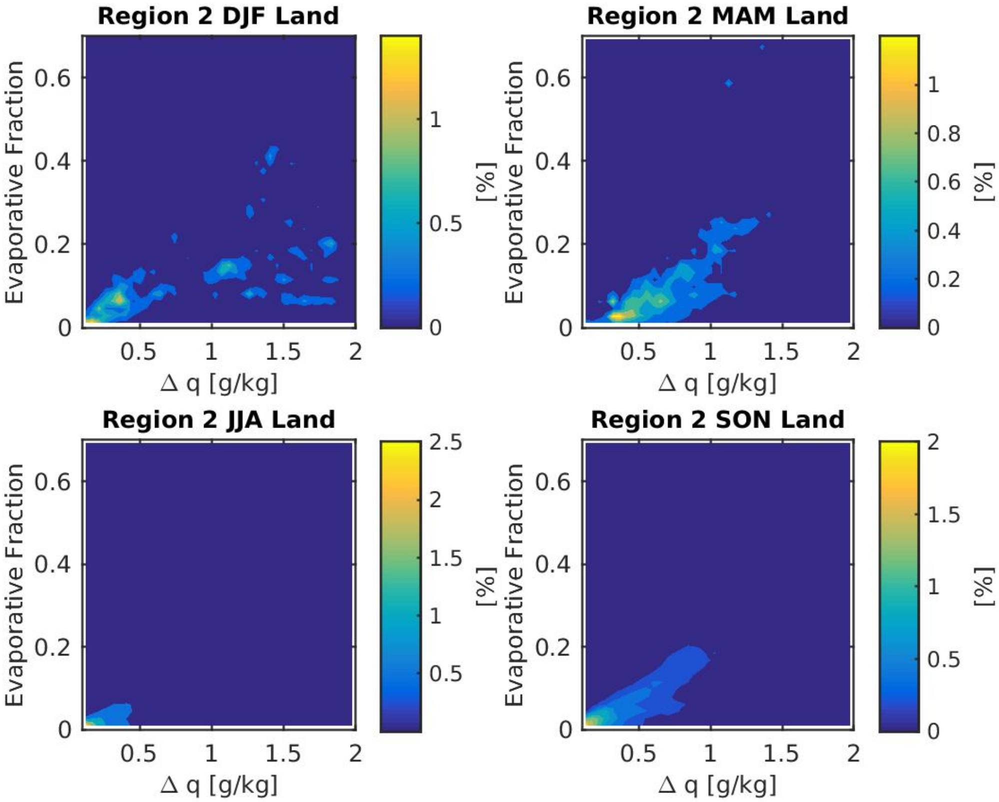

Figure 54. As in Figure 53, but for boundary layer uptakes over land pixels for floods occurring in Region 2 (Arizona).

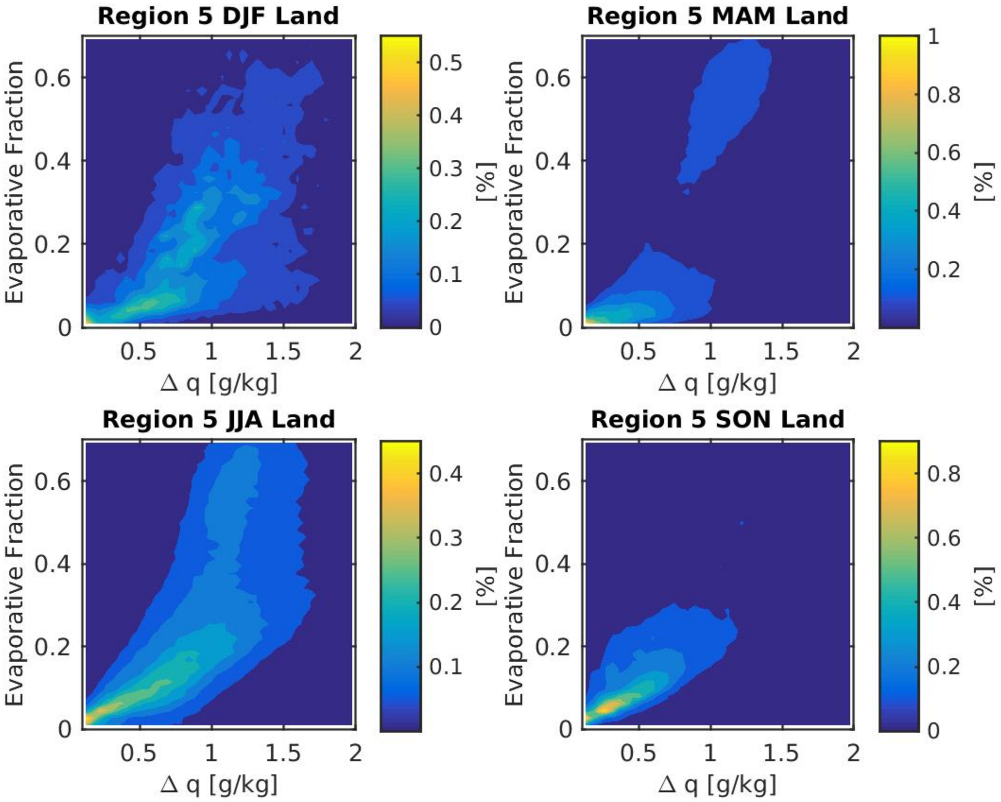

Figure 55. As in Figure 53, but for boundary layer uptakes over land pixels for floods occurring in Region 5 (Missouri Valley).

Lastly, the values of f_{tot} (the total fraction of the final moisture due to boundary layer uptakes) e_{tot} (the total fraction of the final moisture due to non-boundary layer uptakes), and d_{tot}, (the total fraction of the final moisture due to uptakes which cannot be classified by this method and are attributed to a variety of causes including advection and uptakes smaller than 0.1 g kg^{-1}) were computed for each region and each season, as described earlier in this chapter. Relative frequency histograms of each parcel's fractional boundary layer contribution, fractional non-boundary layer contribution, and advection/other contribution are presented. The values of the 25th, 50th, and 75th percentiles are noted for each type of contribution and for each season at the top of the figures. It is important to note that the advection contribution in the following plots represents the specific humidity of the parcel present 120 hours (5 days) or before the parcel was launched. While this is close to the time scale in which atmospheric water vapor is recycled, the parcels are allowed to start their journey to the flooded area with some water vapor.

For Region 1 (West Coast) during DJF, where the primary driver of cool season heavy rainfall and flash flooding involves moisture transport across the Pacific Ocean, and landfalling extratropical cyclones, the median values for the fraction of parcel water vapor content that is advected/other is 0.85, that is 50% of parcels have more than 85% of their ending water vapor attributed to advection (Figure 56). During winter 25% or more of parcels have 100% of their water vapor due to advection or uptakes less than 0.1 g kg^{-1}. In other seasons, the median fraction of advected water vapor is around 50% (0.51 in MAM, 0.48 in JJA, and 0.53 in SON), and the tail of the distribution shifts leftward, with a minimum 75th percentile value of 0.71 in JJA. In MAM (though a smaller sample) and JJA, the 75th percentile values of boundary layer contributions are 0.54 and 0.55 respectively, indicating that 25% of parcels have greater than half of their ending values of specific humidity derived from the boundary layer. In JJA, the distributions of boundary layer fraction and advected fraction closely match, with the exception of there being a percentage of advected fraction values close to 1.0. In all seasons, the fraction of parcel water vapor due to increases in moisture above the boundary layer is low, with 75% of parcels having less than 11%, 19%, and 24% of their water vapor from this source in MAM, JJA, and SON, respectively.

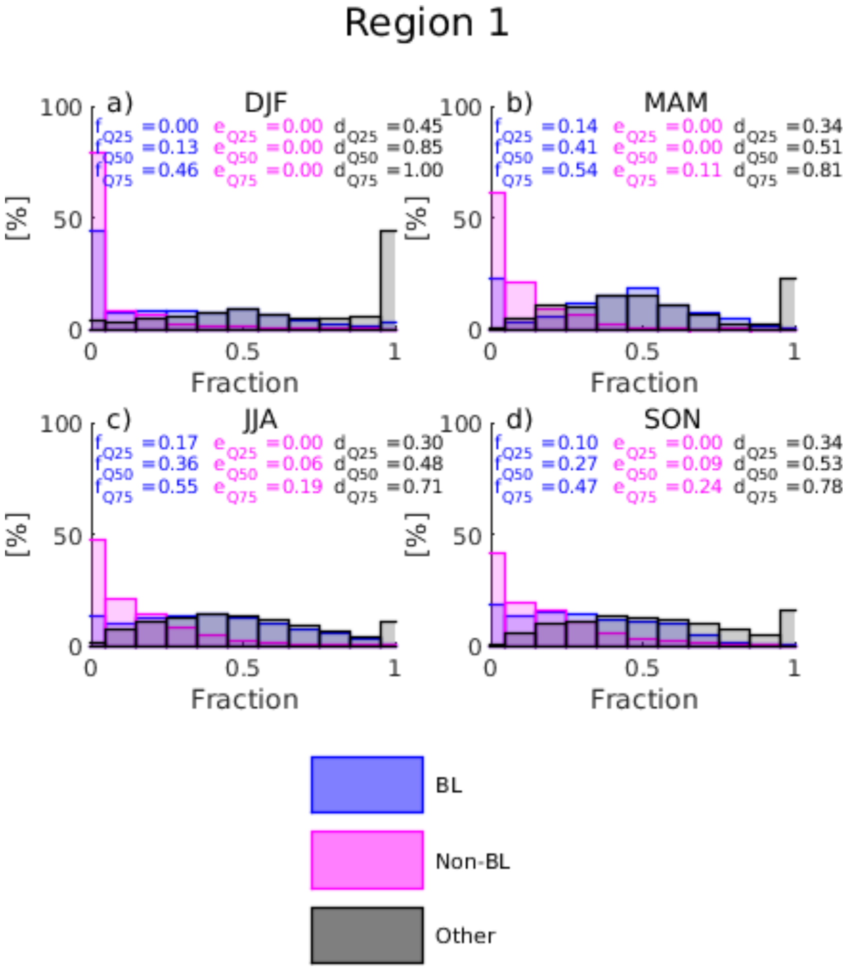

Figure 56. Relative frequency histograms of the fraction of parcel specific humidity at the end of the trajectory due to boundary layer uptakes (blue), uptakes occurring outside of the boundary layer (magenta), and advection/uptakes less that 0.1 g kg^{-1} during a) DJF, b) MAM, c) JJA, and d) SON for Region 1 (West Coast).

In Region 2 (Arizona), a similar pattern of advection dominates events occurring in DJF, with 50% of parcels having 56% or more of their water vapor prior to the start of the 120-hour trajectories (Figure 57). MAM has a very small number of events, but in those cases, 75% of parcels had 48% or less of their specific humidity from advection. As with Region 1, the fractions of boundary layer contribution and advective contribution were most equal during JJA and SON. MAM events saw 50% of parcels have 57% or greater contribution from the boundary layer. Non-boundary layer uptakes were maximized in JJA, though these uptakes remained a small amount of the final specific humidity of parcels.

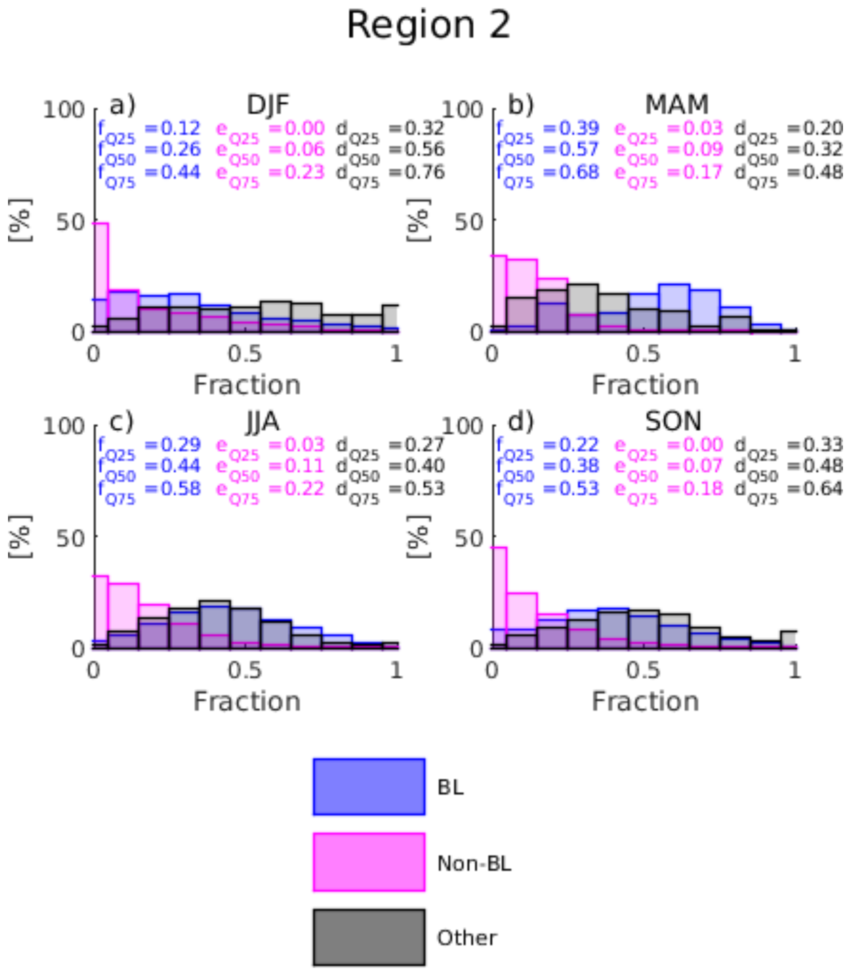

Figure 57. As in Figure 56, but for Region 2 (Arizona).

Along the Front Range (Region 3), the advective contribution to the parcels' final specific humidity is largest in SON, followed closely by JJA (Figure 58). In JJA, as in the previous regions, the distributions of fractional contributions of boundary layer moisture and the advective component are similar. In SON, there is a larger advective component, and in MAM there is a larger fractional contribution of boundary layer moisture. In all cases, the non-boundary layer contribution to parcel specific humidity has a median value less than or equal to 7%, and a 75th percentile value of 17% or lower.

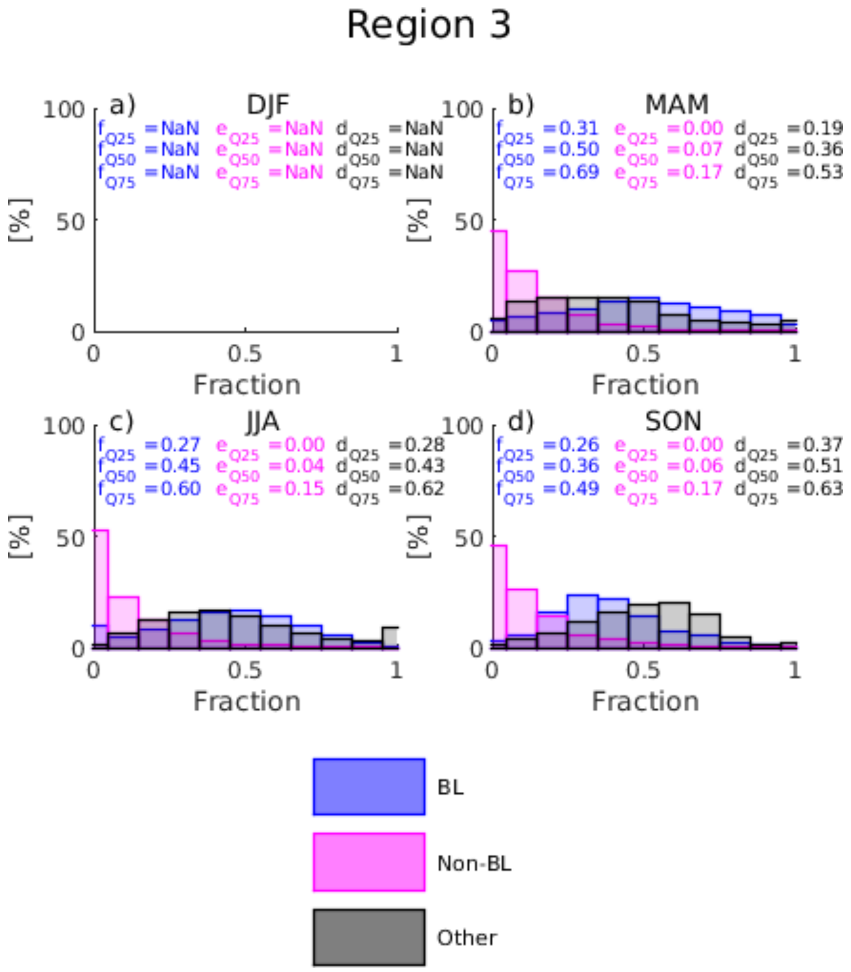

Figure 58. As in Figure 56, but for Region 3 (Front Range).

In Flash Flood Alley (Region 4), advection is no longer the largest constituent of parcel specific humidity (Figure 59). In this case the median value of the fractional contribution of boundary layer moisture is 35%, whereas for advection it is 29%. The 75th percentile values are 75% for the boundary layer contribution and 54% for the advective component. In MAM, the 75th percentile value for fractional contribution of boundary layer moisture is 66%, and the advective component is 49%. These distributions become more balanced, with JJA median values of 38% and 40% for boundary layer and advective/other, respectively, with the 75th percentile values of 53% and 51%. In SON, the boundary layer contribution again dominates with median values of 48% (34% advective) and 75th percentile values of 74% (50% advective). In Flash Flood Alley, the non-boundary layer sources of moisture play the largest role in JJA, but the values of non-boundary layer fractional contribution to specific humidity are larger than Regions 1-3.

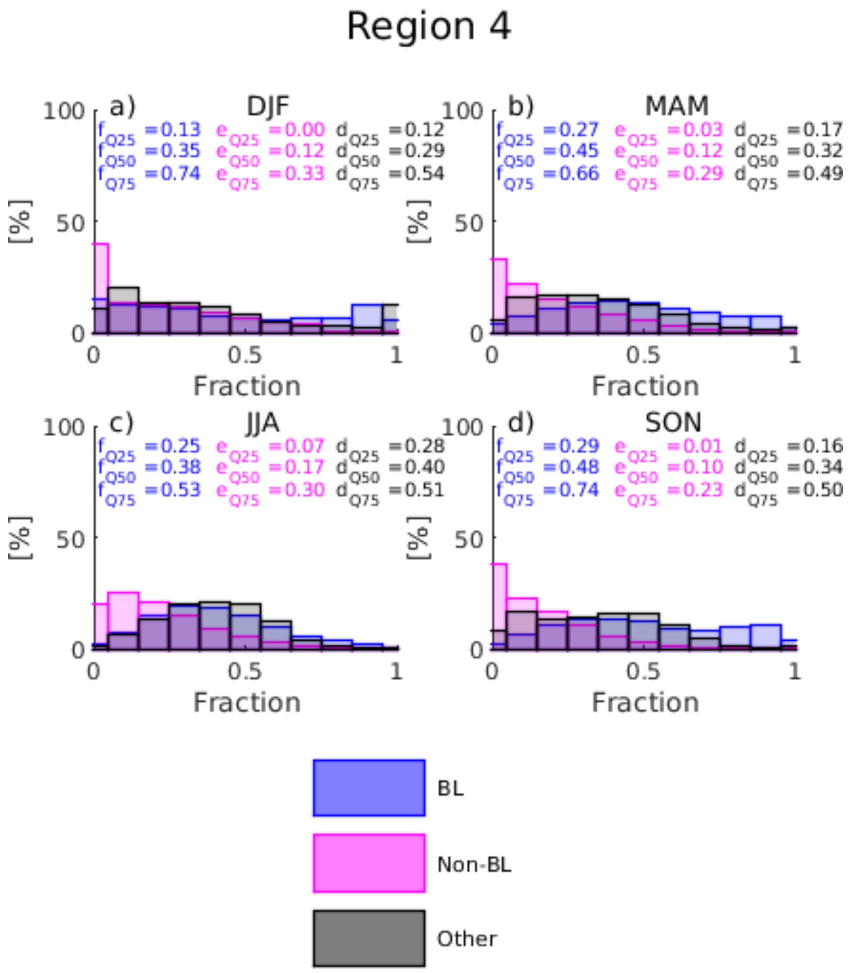

Figure 59. As in Figure 56, but for Region 4 (Flash Flood Alley).

For Region 5 (Missouri Valley), the rightmost tails of the distributions are populated by contributions from the boundary layer in DJF and MAM, with median values of 48% and 47%, respectively, with 75th percentile values of 73% and 66%

(Figure 60). In JJA, the median and upper quartile values diminish to 44% and 58%, though the entire distribution moves toward the median, with a slight increase in the value of the lower quartile. The distribution of advective contribution also shifts rightward from median values slightly less than 30% in DJF and MAM to a median value of 37% in JJA. The SON distribution is most similar to that in JJA for this region. Non-boundary layer uptakes play more of a role for the Missouri Valley, though not as much of a role as they do for Flash Flood Alley.

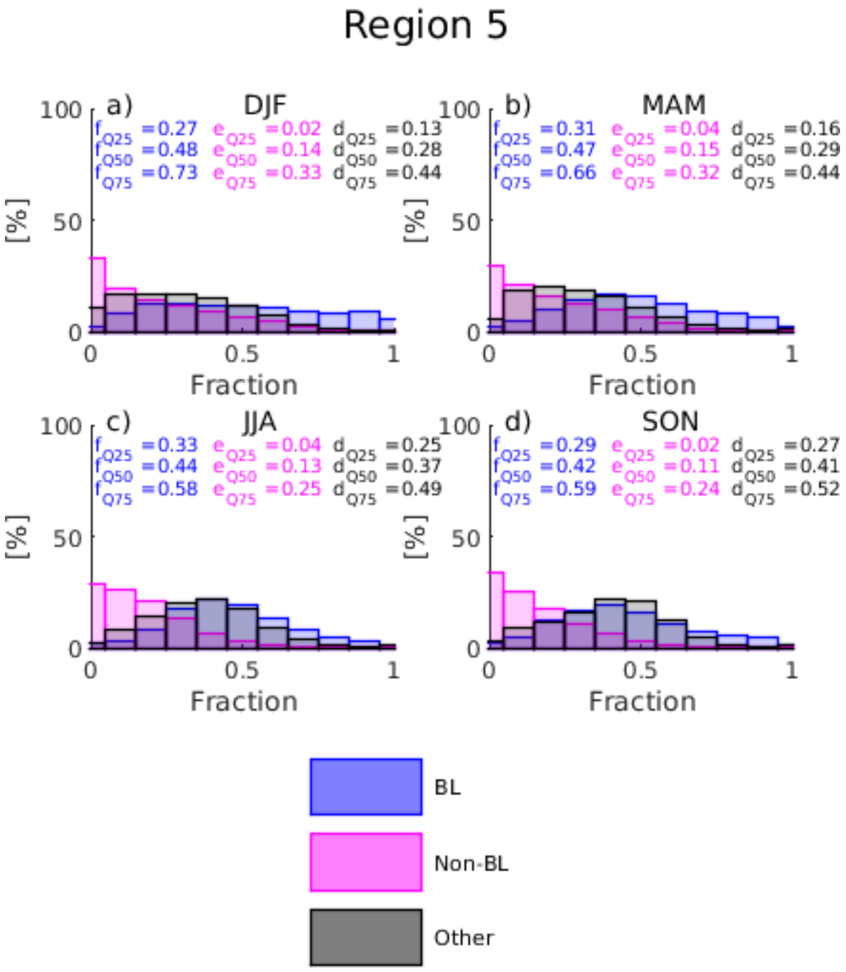

Figure 60. As in Figure 56, but for Region 5 (Missouri Valley).

In the Appalachians (Region 6), the fractional contributions of boundary layer moisture are largest during DJF and MAM, with median values of 50% and 47%

respectively (Figure 61). At these times the distribution of advected moisture is skewed to the left and is at its minimum for this region. During DJF and MAM, the amount of water vapor due to non-boundary layer sources is also the largest, with median values of 10% and 75th percentile values of 29% and 26% respectively. In JJA, advection and boundary layer uptakes are of equal magnitude, with all quartiles being within 0.01 of each other. During JJA, non-boundary layer sources of moisture diminish in importance, and have a very small contribution by SON. During SON, the right tail is slightly heavier for advective sources of moisture, though both the advective and boundary layer sources of moisture have a wide and flat distribution. That is, some parcels have large contributions of advective moisture and that is compensated by low values of boundary layer moisture and vice versa.

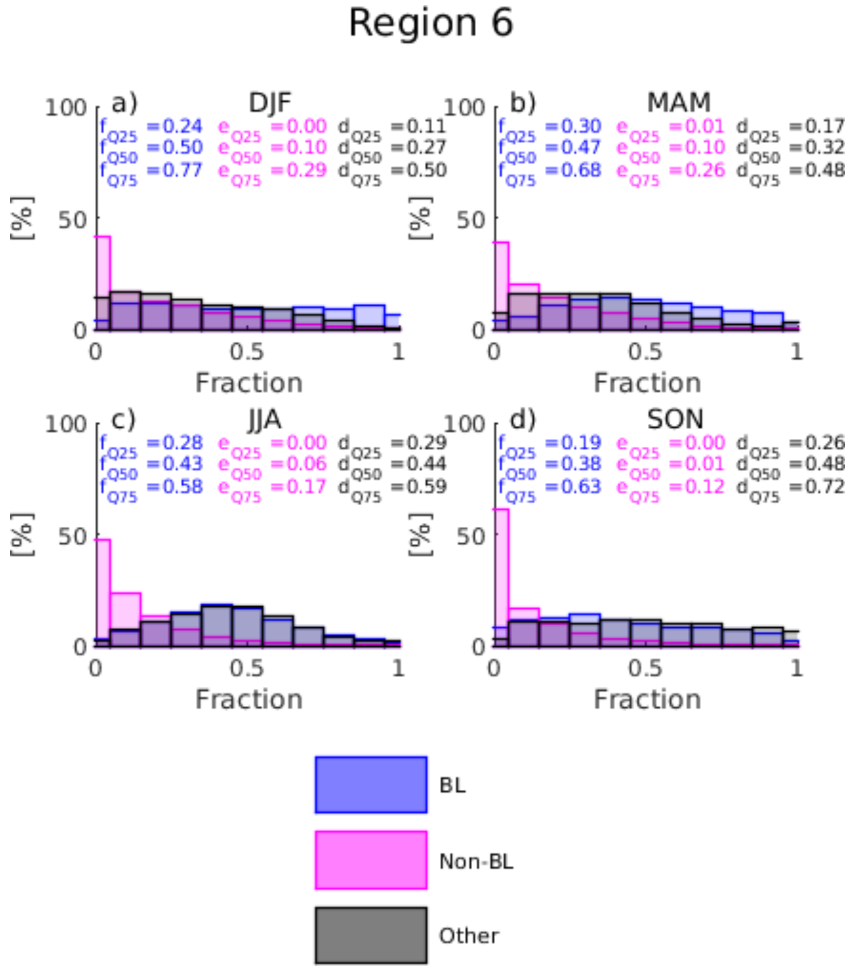

Figure 61. As in Figure 56, but for Region 6 (Appalachians).

In summary, advection is the most important contributing mechanism to total parcel specific humidity for floods occurring along the West Coast and in Arizona during the cool season. The boundary layer contributions to final parcel moisture were largest in transitional seasons (spring and fall) for Flash Flood Alley and the Missouri Valley. Contributions during the summer months are portioned similarly between boundary layer uptakes and advection.

4.3 Summary and Conclusions

The centroids of flash flood reports from NWS *Storm Data* for the period 2007-2013 were used to initialize 66 km x 66 km grids with 30 hPa spacing in the vertical (from 950 hPa to 470 hPa). Parcels were launched from these three dimensional boxes, centered on the flash flood report, and traced backwards 120 hours (5 days) in order to 1) assess the dominant track of parcels that terminate at various pressure levels in flash flooding setups; 2) delineate regions where parcels increased their specific humidity; 3) determine whether or not those moisture uptakes occurred within the boundary layer, having some influence from the land surface properties, and 4) characterize the properties of the land surface when parcel moisture uptakes were linked to the boundary layer. This work extends the methodology described in Sodemann et al. (2008) by including the land surface properties from a multi-year HRLDAS simulation, the offline version of the Noah land surface model, where boundary layer uptakes were observed.

The analysis was divided into six regions of interest: 1) West Coast, 2) Arizona, 3) Front Range, 4) Flash Flood Alley, 5) Missouri Valley, and 6) Appalachians according to the flashiness regions delineated by Saharia et al. (2017). Cases were subdivided further by season (DJF, MAM, JJA, and SON) in order to study the seasonality of flash flood mechanisms.

The major source regions for boundary layer moisture for flash floods in the United States are the Gulf of Mexico and the Gulf of California. The Gulf of California is most active during JJA and SON, when the NAMS is active. The Gulf of Mexico is a key source of moisture for flash floods occurring east of the Continental Divide for all seasons. Most of the mass that is evaporated from these bodies of water occurs over the summer months, which is the peak season for flash flooding in the CONUS. The terrestrial area where most of the boundary layer uptakes occur is the south central US, which includes the SGP, a known hotspot for land-atmosphere interactions. All regions exhibit nearly unidirectional or slightly veering flow with height throughout a deep layer in the lower troposphere.

Non-boundary layer sources of moisture tend to coincide with boundary layer sources of moisture over land, though these uptakes are lesser in magnitude. Over water, the spatial pattern of where boundary layer uptakes occur versus where non-boundary layer uptakes occur differs, and boundary layer uptakes account for most of the mass taken up over water.

In all regions and seasons, pixels where boundary layer uptakes occur are characterized by anomalously high latent heat fluxes, anomalously low sensible heat fluxes, anomalously large evaporative fractions, and anomalously wet soils in the 0-10 cm layer below ground. Positive SST anomalies are largest during JJA for Arizona (Region 2) in the Gulf of California, characteristic of the NAMS. SST anomalies are also large in regions and season affected by tropical storms in the Atlantic basin.

Lastly, the fraction of final parcel moisture attributed to boundary layer, non-boundary layer and advective moisture sources was assessed using the methodology described in Sodemann et al. (2008). In DJF, transport is the most important mechanism for events occurring in Regions 1 and 2, which was expected given the climatological pattern of ARs for these regions. The boundary layer contribution for final parcel moisture was largest in the spring and fall for Flash Flood Alley and the Missouri Valley and largest from spring along the Appalachians. During the summer months, transport and boundary layer contributions had similar distributions, indicating that some parcels had larger contributions from advection that would be balanced out by smaller contributions from the boundary layer and vice versa. In all cases, non-boundary layer uptakes were the smallest contributor to the parcel’s final moisture.

Chapter 5: Microphysical Insights into Orographic Precipitation During IPHEx

5.1 Moisture Sources for Flash Floods in the Smoky Mountains

The study of orographic precipitation and its related mechanisms has led to specific experiments in mountainous regimes. In particular, the meteorology and hydrology of the Great Smoky Mountains have been the focus of studies related to precipitation processes in previous years (Prat and Barros 2010; Wilson and Barros 2014 and 2015; Duan et al. 2015). Wilson and Barros (2014) relate the increase of reflectivity toward the ground in Micro Rain Radar observations with the interactions between low-level clouds and fog and precipitation, as well as model moisture convergence patterns required to produce the low-level phenomena.

Using the methodology from the previous chapters, the seasonal and diurnal cycles of floods in the Smoky Mountains are shown in Figure 62. The peak in flood activity is in the late spring through summer, with secondary peaks in March and November. This fits within the broader pattern of floods within Region 6, whose peak was in August and September. The temporal pattern of floods in the Smokies matches that in the Appalachians more broadly, with the peak timing for floods occurring in the afternoon with thunderstorm activity.

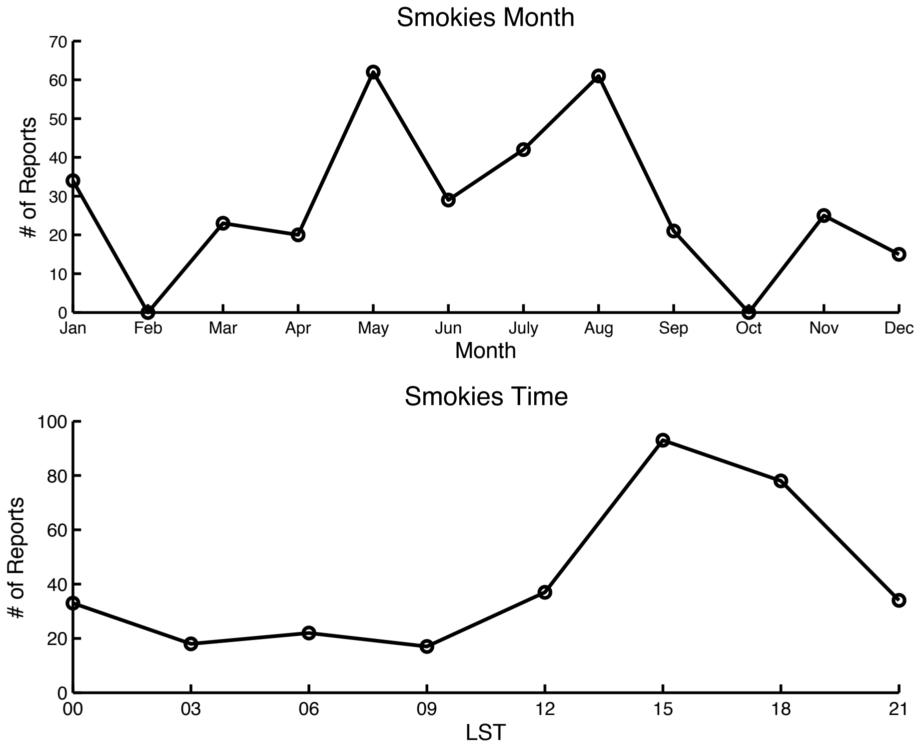

Figure 62. Flash flood reports by month (top) and LST hour (bottom) for floods occurring from 2007-2013 in the Smoky Mountains.

The trajectories for centroid points for the Smoky Mountains are shown in Figure 63. Trajectories that terminate at 850 hPa and 700 hPa originate over the Gulf of Mexico or the Atlantic Ocean. Some parcels which end at 500 hPa are embedded in westerlies, while others ascend from over the Gulf of Mexico toward the Smoky Mountains. Moisture sources for this region include uptakes over the Atlantic Ocean, Gulf of Mexico and a broad region of the Southeast (not pictured).

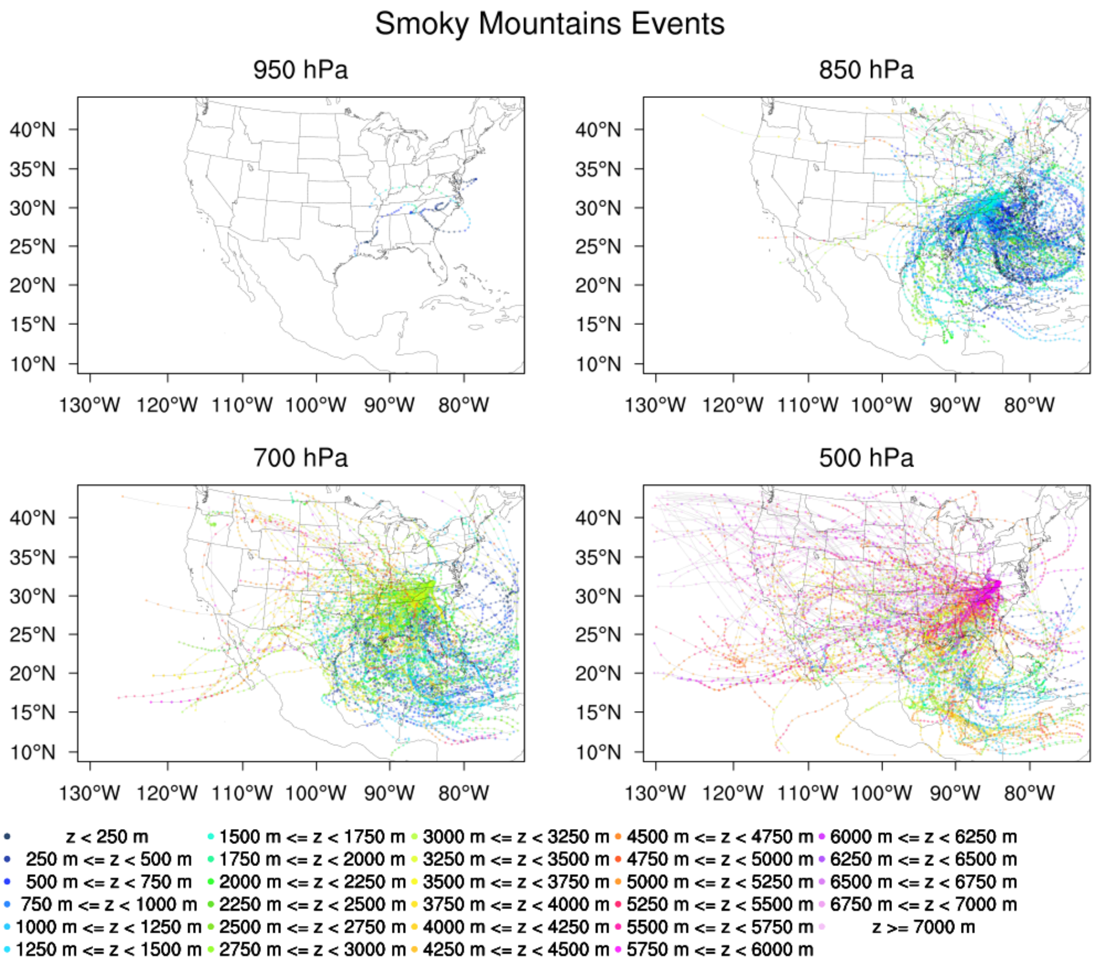

Figure 63. As in Figure 11, but for floods occurring in the Smoky Mountains.

5.2 The Integrated Precipitation and Hydrology Experiment (IPHEx)

An Intensive Observation Period (IOP) for the Integrated Precipitation and Hydrology Experiment (IPHEx; Barros et al. 2014), part of the NASA's Ground Validation (GV) campaign for the Global Precipitation Measurement Mission (GPM; Hou et al. 2014) satellite, launched 27 February 2014, took place from 1 May-15 June 2014 in the Smoky Mountains of western North Carolina. As part of the experiment, the National Severe Storms Laboratory's (NSSL) mobile dual-polarization X-band radar, NOXP, was deployed in the Pigeon River Basin (PRB). During that time, several events were sampled, ranging from morning fog to diurnally driven convection to landslideinducing thunderstorms. The field experiment also leveraged a network of tipping bucket rain gauges, which has been in place in the Southern Appalachians since 2007 as a joint endeavor between Duke University and The University of North Carolina-Asheville, hereafter Great Smoky Mountain National Park Rain Gauge Network (GSMNP-RGN). Additional ground instrumentation included a network of dual-platform rain gauges, a disdrometer network, NASA's NPOL S-band radar, and NASA's ground-based radar, D3R (Chandrasekar et al. 2010). The NASA ER-2 and UND Citation aircraft carried a number of passive and active sensors and GPM satellites also sampled events during this time. The locations of relevant ground instrumentation and NOXP are shown in Figure 64.

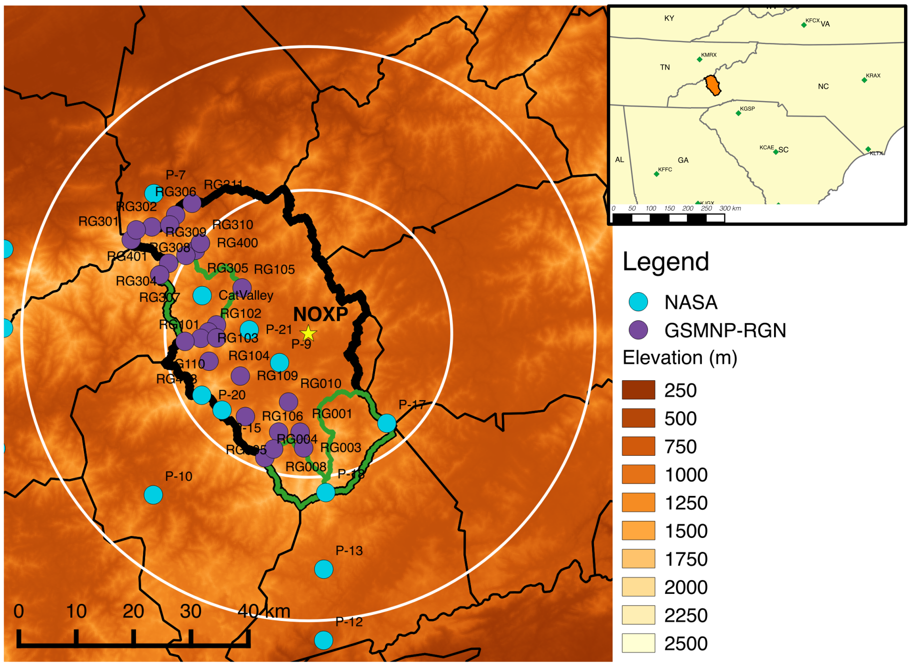

Figure 64. Map of NOXP (yellow star) and the surrounding vicinity. Outlined in black is the Pigeon River basin, and its sub-catchments are outlined in green. Disdrometer sites (with co-located PARSIVEL disdrometers and NASA dual-platform rain gauges) are marked with blue circles, and GSMNP-RGN gauges are marked with purple circles. Range rings correspond to 25 km and 50 km from the radar.

Table 5. Characteristics of NOXP.

Latitude	35.56419°N
Longitude	82.91123°W
Altitude above sea level (m)	1176
Frequency (MHz)	9410
Wavelength	3.22 cm
Peak Power at antenna port (kW)	81.1
Antenna type	Parabolic Dish
Antenna Gain (dBi)	45.5
-3 dB Antenna aperture	0.9°
Polarization	Dual Linear
Rotation speed (rpm)	0-5
Range	111 km (for 1350 pulses/s)

The specifications for NOXP are shown in Table 5. The NOXP site was located on a ridge below the Chambers Mountain fire station near the center of the Pigeon River Basin. The scanning strategy was a series of Plan Position Indicator (PPI) surveillance scans in a modified Volume Coverage Pattern (VCP)-12, shown in Figure 65, with the addition of a 0.1 degree tilt.

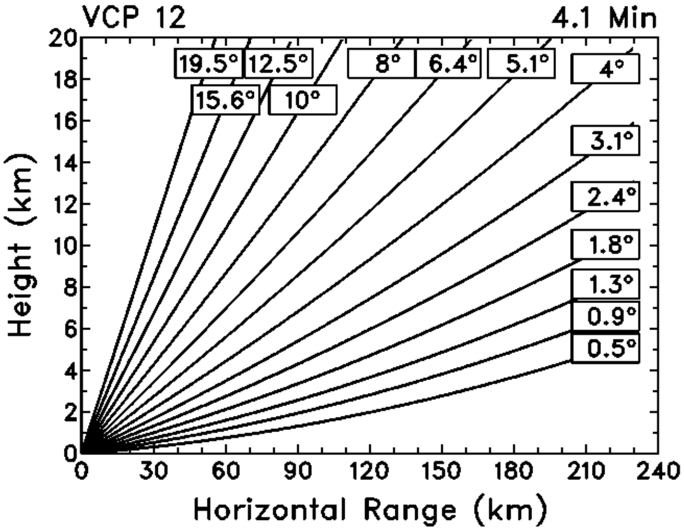

Figure 65. Volume coverage pattern used by NOXP. Additional Range Height Indicator scans were performed as well as vertically pointing scans. Source : nssl.noaa.gov

Given a pulse repetition frequency of 1350 s^{-1}, the radar data had an unambiguous range of 111 km. Unfortunately, the radar experienced severe blockage due to nearby trees and terrain at lower elevation angles from about 330 degrees to 115 degrees in azimuth. However, NOXP was positioned to sample the atmosphere above networks of ground instrumentation and three small catchments within the larger PRB previously studied by Tao and Barros (2013): the Cataloochee Creek Basin (128 km^2), the East Fork Pigeon River Basin (131 km^2), and the West Fork Pigeon River Basin (71 km^2). The radar was also capable of performing Range Height Indicator (RHI) scans and vertically pointing scans for differential reflectivity (ZDR) calibration. RHI scans were performed primarily in coordination with aircraft and NPOL at the direction of mission scientists but also for storms of interest to the radar operator. In total, NOXP collected nearly 182 hours of data and 1267 RHI scans. Hybrid scans were produced based on the beam height above terrain, with a correction to account for trees near the radar site, especially to the west and southwest.

The Self-Consistent Optimal Parameterization-Microphysics Estimation (SCOP-ME) radar processing algorithm applied on the NOXP for radar observations in liquid precipitation is described in detail in Kalogiros et al. (2013), Anagnostou et al. (2013), and Kalogiros et al. (2014) based on their work with the National Observatory of Athens mobile dual-polarization Doppler X-band radar (XPOL). Once the radar volume has been quality controlled and then corrected for attenuation (only in the selected liquid precipitation regimes) and bright band effects as in Kalogiros et al. (2013), the precipitation rate is estimated as follows (Anagnostou et al. 2013):

$$R = 0.8106 F_R(\mu) N_W D_0^{4.67} f_{R_2}(D_0) \tag{63}$$

The rainfall rate is based on a normalized gamma drop size distribution (DSD; Testud el al. 2000; Illingworth and Blackman 2002):

$$n(D) = N_W f(\mu)\left(\frac{D}{D_0}\right)^{\mu} \exp\left[-(\mu+3.67)\frac{D}{D_0}\right] \tag{64}$$

where n(D) (m^{-3} mm^{-1}) is the volume density, D_0 (mm) is the median volume diameter, N_W (mm^{-1} m^{-3}) is the intercept parameter, and μ is the shape parameter of the DSD. The other variables in Equation 63 are determined from radar measurements by

$$F_R(\mu) = 0.6\times10^{-3}\pi\times3.78\frac{6}{3.67^4}\frac{(3.67+\mu)^{\mu+4}}{\Gamma(\mu+4)}\times\frac{\Gamma(\mu+4.67)}{(\mu+3.67)(\mu+4.67)} \tag{65}$$

where Γ is the gamma function. The DSD parameters are estimated as follows

$$D_0 = D_Z f_{D_0}(D_Z) \tag{66}$$

$$D_Z = D_{Z_1} f_{D_{Z_1}}(D_{Z_1}) \tag{67}$$

$$D_{Z_1} = 0.1802\left[\frac{Z_H}{K_{DP}}\xi_{DR}^{-0.2929}(1-\xi_{DR}^{-0.4922}\right]^{1/3} \tag{68}$$

$$N_W = 3610\left[\frac{K_{DP}}{(1-\xi_{DR}^{-0.3893})}\right]D_0^{-4} f_{N_{W_2}}(D_Z) \tag{69}$$

subject to the constraint on the shape parameter (derived from disdrometer observations) of

$$\mu = 165e^{-2.56D_0} - 1 \tag{70}$$

In the above equations, D_Z is the reflectivity-weighted mean diameter (mm), ξ_{DR} is the differential reflectivity in linear units, and the horizontal reflectivity (Z_H) is also expressed in linear units in the above equations. The functions of the form $f_p(D_Z)$, where p denotes parameter in question, characterize the Mie scattering effects and are of the form:

$$f_p(D_Z) = \frac{\sum_{n=0}^{3} a_n D_Z^n}{\sum_{n=0}^{3} b_n D_Z^n} \tag{71}$$

The coefficients a_n and b_n are given in Table 6. A -10 dB bias in reflectivity was found when checking the calibration of NOXP against the nearest disdrometer. After the bias was removed, this algorithm was used to process the raw NOXP data and produce precipitation estimates. The ground validation campaign data have been published online at https://fcportal.nsstc.nasa.gov/iphex/.

Table 6. Coefficients for the rational polynomial in Equation 71, reproduced from Anagnostou et al. 2013.

Function	a_0 / b_0	a_1 / b_1	a_2 / b_2	a_3 / b_3
f_{D0}	0.9542/1.0000	0.2989/0.2243	0.0577/0.2949	0.0030/-0.005
f_{DZ1}	0.9190/1.0000	0.1501/-0.2248	-0.1722/0.0182	0.0511/0.023
f_{Nw2}	1.0000/1.0000	-0.6792/-0.6410	0.2112/0.1551	-0.0109/-0.0006
f_{R2}	1.0000/1.0000	-1.2313/-0.2176	2.1166/0.3064	0.6842/1.230

5.3 Results

The PRISM climatology of precipitation (Daly et al. 1994; Daly et al. 2008) over the PRB is shown in Figure 66.

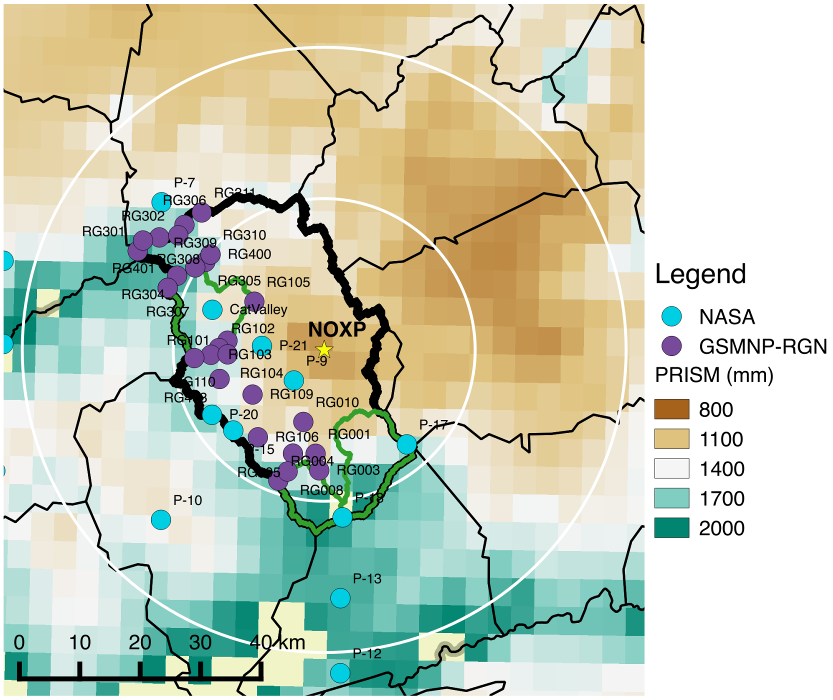

Figure 66. PRISM annual rainfall climatology (mm) over the IPHEx domain.

The PRISM climatology is a regression from station data onto DEM cells weighted by several factors: location, elevation, proximity to the coast, orientation of the topography, among others. Local maxima in precipitation are found along ridgelines to the west and south of the PRB, and it is posited here that orographic enhancement of precipitation is a cause of these patterns. The PPI and RHI NOXP data were examined to find cases where storms were propagating upslope. Of these data, the case of widespread stratiform precipitation with embedded convection (Figure 67) in the morning hours of 27 May 2014 was sampled by NOXP and will be presented as a case study of orographic effects on precipitation microphysics. Preceding the event, fog and low-level clouds were observed, characteristic of the Smoky Mountains. Surface winds were out of the west-southwest to west, resulting in upslope flow in the western portion of the PRB.

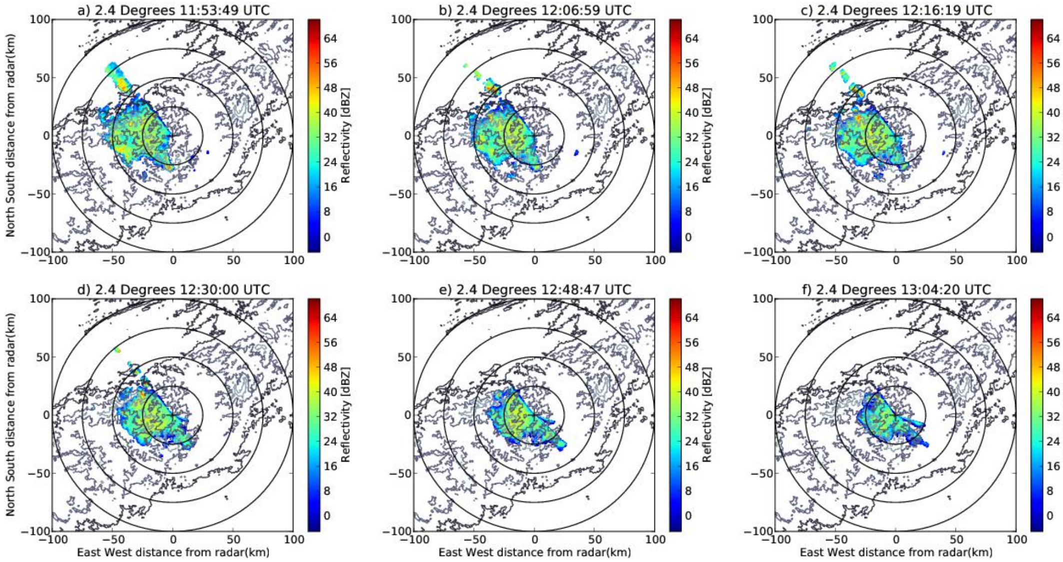

Figure 67. Radar reflectivity for Plan Position Indicator scans at the 2.4 degree elevation angle for a) 1153 UTC, b) 1207 UTC, c) 1216 UTC, d) 1230 UTC, e) 1248 UTC, and f) 1304 UTC. Range rings are shown every 25 km from the radar. Underlying terrain is contoured every 500 meters.

Over the course of the event, the radar operator performed sets of RHIs for areas of interest, interspersed with volume scans to accomplish the primary objective of precipitation estimation. Three sets of RHIs were performed within the 1200 UTC hour, for a total of 54 scans. A representative example of the structure of precipitation in the RHIs is shown in Figure 68. There is a well-defined bright band just below 4 km AMSL, with the heaviest precipitation falling along the ridgeline and tapering off toward the valley. The polarimetric signatures present include the prominent melting layer (high Z and ZDR; low correlation coefficient) and a signature of riming over the higher terrain. The signature of riming includes an increase of Z and decrease of ZDR from the upper regions of the cloud toward the melting layer and a “sagging” of the bright band due to the increased terminal velocity of falling rimed particles (Kumjian et al. 2016). Below the melting layer, there is an increase of Z and ZDR toward the ground, because these particles are becoming liquid, are large in size, and are efficient collectors of smaller drops as they fall.

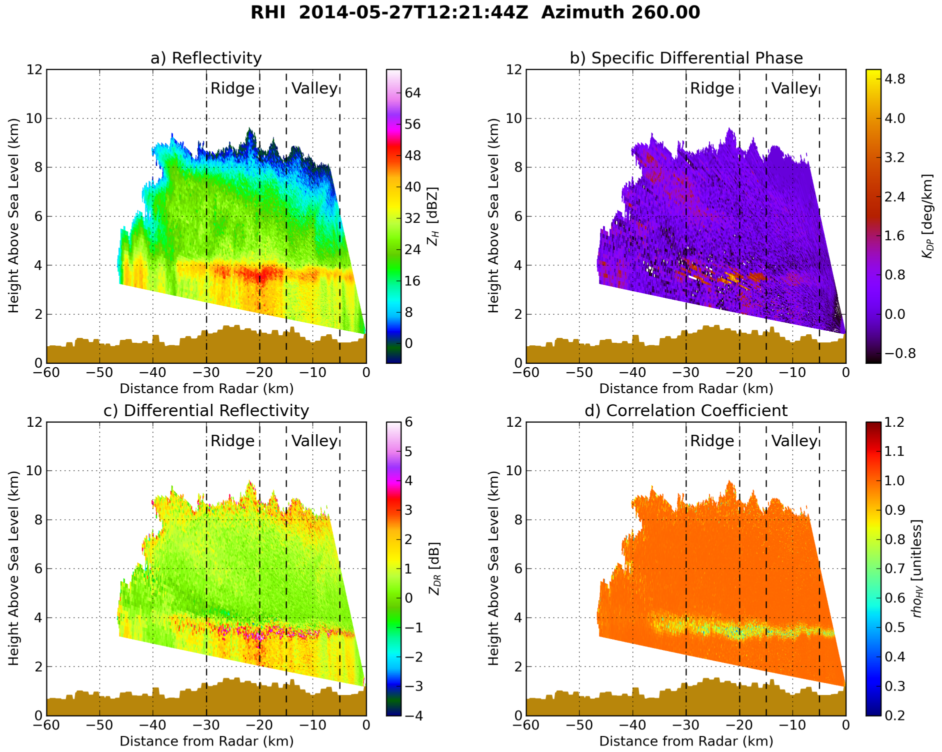
RHI 2014-05-27T12:21:44Z Azimuth 260.00

a) Reflectivity

b) Specific Differential Phase

c) Differential Reflectivity

d) Correlation Coefficient

Figure 68. Range Height Indicator scan at 1221 UTC at 260 degrees in azimuth for a) reflectivity, b) specific differential phase, c) differential reflectivity, and d) correlation coefficient. The terrain height is filled along the x axis.

Contoured Frequency By Altitude (CFAD) diagrams (Yuter and Houze 1994) of reflectivity and differential reflectivity are shown Figure 69a-b and d-e for the RHI scans at ridge and valley locations. The ridgeline is defined as 20-30 km in range from 225-315 degrees in azimuth. The valley locations are defined as 5-15 km in range for the same azimuthal sector. RHIs were used in lieu of PPIs at this stage due to the limited vertical extent of the VCP over the valley locations. The 25th, 50th, and 75th, percentile values are shown at each height bin. The CFAD diagrams reveal a wider distribution of Z and ZDR over the ridgeline and narrower distributions over the valley. The magnitude of Z and ZDR values over the ridge are larger over the vertical profile than those over the valley. The slope in reflectivity above the melting layer is steeper over the valley than over the ridge. This characteristic has been observed previously by Wilson and Barros (2014) using micro rain radars at the seasonal time scale. The vertical profile over the ridge reveals the presence of two different slopes in reflectivity above the bright band, including a segment centered on 25 dBZ from 4-7 km AMSL. This is due to a higher concentration of supercooled liquid water droplets and/or the riming of ice particles. The nearly vertical slope of ZDR values greater than zero in the same region would also suggest that this is likely. Over the terrain, updrafts may be enhanced and sustained, promoting the existence of these hydrometeors. Above 7 km, the profiles over the ridge and valley are quite similar.

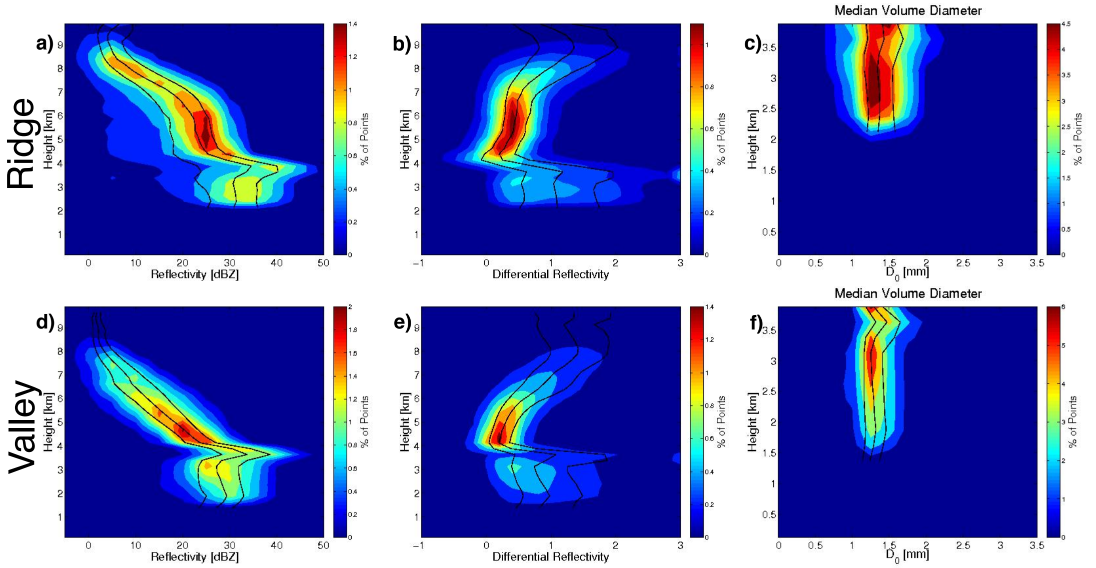

Figure 69. Contour Frequency by Altitude Diagrams from RHI scans in the 1200-1300 UTC hour over the ridge (top) and valley (bottom) for reflectivity (a and d), differential reflectivity (b and e), and median volume diameter (c and f). Quantile values for the 25th, 50th, and 75th percentiles are overlaid in black.

CFAD diagrams were also produced for the median volume diameter, D_0, of the DSDs and are shown in Figure 69c and f. As with the profiles of Z and ZDR, the profiles of D_0 over the valley have a narrower distribution than those over the ridge. The larger drops over the ridgeline suggest the dominance of coalescence processes and convection over the mountains.

In order to discern the microphysical processes governing the precipitation in this case, the framework described by Kumjian and Ryzhkov (2010) (henceforth KR) and used in Kumjian and Prat (2014) was employed. Within this parameter space, the differences in reflectivity and differential reflectivity between bins at the bright band and bins at the lowest gate are used to determine the dominant microphysical regime of the precipitation: size sorting/evaporation, breakup, coalescence, and a balance between breakup and coalescence. Size sorting/evaporation and coalescence result in an increase in differential reflectivity from the bright band to the surface, while breakup and the breakup-coalescence balance exhibit a decrease in differential reflectivity. In coalescence and breakup-coalescence regimes, reflectivity increases, while in size sorting/evaporation and breakup processes, there is a negative change in reflectivity from the bright band to the surface. These regimes are annotated in the following figures for convenience.

The differences in Z and ZDR from 1100-1500 UTC on 27 May 2014 in KR space derived from PPI scans are shown in Figure 70a and b for locations along the ridge and valley. The KR parameter space from the 54 RHI scans within the 1200 UTC hour are shown in Figure 70c and d. Over the valley, a variety of microphysical processes are ongoing, and the distribution of points is nearly centered over the origin of the KR plot. Over the ridge, the center of mass of the density plot shifts into the upper-right quadrant dominated by coalescence processes, as the melted aggregates fall and increase in size. Because the pattern of microphysical processes in the parameter space for both PPIs and RHIs is similar, PPIs perhaps may be used to discern microphysical regime from operational radar data.

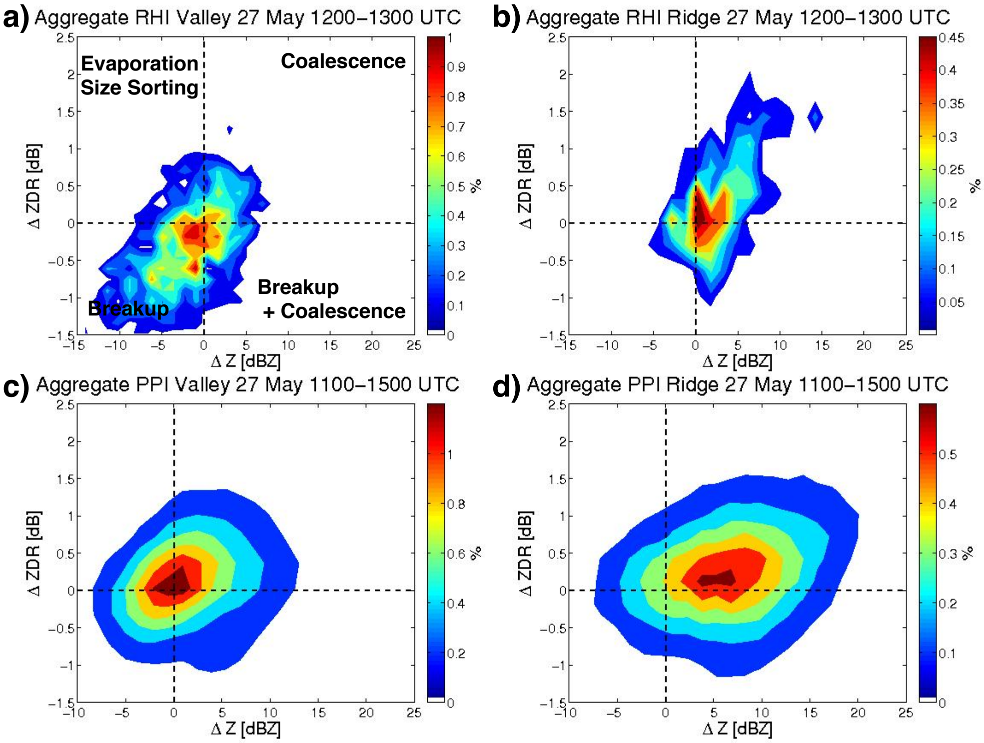

Figure 70. Density plots of KR diagrams for RHIs over the a) valley and b) ridge and PPIs over the c) valley and d) ridge. For reference, the qualitative descriptions of dominant microphysical regime are annotated in panel a).

5.4 Summary and Conclusions

An IOP for the IPHEx experiment was conducted from 1 May – 15 June 2015 in the Great Smoky Mountains of North Carolina. During that time, the mobile dual-polarization radar, NOXP, was positioned within the Pigeon River Basin for precipitation estimation. On 27 May 2014, the radar was used to observe a case of widespread stratiform precipitation. Signatures of riming of ice particles and larger drops below the melting layer were observed over the ridgeline in the sector 20-30 km west of the radar, whereas these signatures are absent over the valley (5-15 km in range). CFAD diagrams of reflectivity and differential reflectivity suggest the presence of a greater concentration of supercooled water from 4-6 km above sea level in this region, possibly due to sustained and enhanced updrafts of moist (or fog-laden) air controlled by the topography. Below the bright band, and over the ridge, the change in Z and ZDR plotted in KR parameter space suggests a regime dominated by coalescence, while there is no dominant signal of one microphysical regime over another over the valley. This pattern is present both in PPIs and RHIs. In the absence of RHIs, as in an operational radar setting, this suggests that PPIs used in this framework may have utility in characterizing the dominant microphysical processes below the melting layer, presuming there is reasonable radar coverage at low levels. The enhanced coalescence over the ridgeline coincides with a climatological maximum in precipitation, and this mechanism provides a partial microphysical explanation to enhancing rainfall rates in these upslope regimes.

Although much of the success of the NOXP-derived precipitation products is attributed to better low-level radar coverage in the PRB, the location of the radar and its coverage in the vertical is insufficient for addressing precipitation-fog interactions. This study suggests, however, that in addition to precipitation-fog interactions and landform control of moisture convergence, the effects of topography on microphysical processes play a role in forming the observed precipitation gradients in complex terrain.

Chapter 6: Conclusions and Future Work

Flash flooding is an especially difficult forecasting challenge because it requires both an accurate forecast of the atmosphere and the land surface. The role that the land surface plays in flash flooding that may be most obvious is the generation of runoff and subsequent routing of overland flow. While these effects are indeed important, the work in this dissertation seeks to quantify the effect of the land surface along the trajectories of air parcels that terminate at flooded locations. In order to address 1) if the land surface has a discernable relationship to the moisture budget of flash flood producing storms and 2) if that relationship exists, how it varies seasonally and regionally, 19,253 flash flood cases from NWS *Storm Data* from 2007-2013 were selected to develop a moisture source climatology for flash floods in the United States.

An 11x11 grid or parcels (with 6 km grid spacing), discretized 30 hPa in the vertical from 950 hPa to 470 hPa was released from each flooded location and tracked backwards 5 days (120 hours) in order to assess the parcel's origin. Along each track, when increases in parcel specific humidity were observed, the location of the parcel relative to the boundary layer height was recorded. For moisture increases that occurred within the boundary layer, the land surface properties from a HRLDAS run (the offline version of the Noah land surface model) were also noted. These data were then used to assess the state of the land surface that contributes to parcel moisture in six key regions seasonally (West Coast, Arizona, Front Range, Flash Flood Alley, Missouri Valley, and Appalachians).

This methodology, though uniquely applied here to the flash flood problem, elucidates that many well-known climatological mechanisms are key components for heavy rainfall in these regions. The land surface was found to have a positive contribution to the moisture budget for flash flood events for the United States, though the extent to which this is true varies for region and season, as hypothesized in Chapter 1.

Boundary layer uptakes for all regions and seasons were linked with patterns of high latent heat fluxes combined with low sensible heat fluxes (large evaporative fractions) and positive soil moisture anomalies in the top layer. Trajectory density plots reveal that the flow for flash flood events was unidirectional or slightly veering with height throughout the lower part of the troposphere. This is especially evident when, during DJF, the majority of final parcel moisture for the West Coast (Region 1) is attributable to advection and trajectories at all levels progress across the Pacific Ocean to their final destinations.

For the region influenced most by the NAMS, Region 2 (Arizona), flow during DJF was off the Pacific, and most of the parcels' final moisture was attributed to advection, as in Region 1 in this season. During the NAMS period in JJA and SON, low level flow passes over the Gulf of California. This body of water is characterized with anomalously high SSTs for flash flood events, and is the most notable source of moisture for flash floods in this region. Over land, boundary layer uptakes were characterized by anomalously large latent heat fluxes and anomalously small sensible heat fluxes, which resulted in anomalously large evaporative fractions. These were due to increased top layer soil moisture over the Southwest.

For Region 3 (Front Range), low level parcels approach from over the Gulf of Mexico in the warm season, including over the Gulf of Mexico in JJA. The key boundary layer sources of moisture are the Gulf of California, Gulf of Mexico, and the local areas to the floods. Land surface conditions for boundary layer uptakes show positive latent heat flux anomalies and large evaporative fraction anomalies where the land-atmosphere interactions take place. Positive SST anomalies in the Gulf of Mexico also occurred for this region in SON.

In Flash Flood Alley (Region 4), the main moisture source is the Gulf of Mexico. From DJF to JJA, low level trajectories begin with a westward component that gains a more northward component from season to season and veers with height. Spring and summer are characterized by positive latent heat flux anomalies, negative sensible heat flux anomalies, positive anomalies in evaporative fraction and top layer soil moisture. In SON, there are 0.5-1.5 K anomalies in the Gulf of Mexico where boundary layer uptakes occur. Boundary layer uptake contributions are largest in MAM and SON.

In the Missouri Valley (Region 5), many of the same patterns exist as in Region 4, with respect to parcel flow direction with height, patterns in anomalies of surface fluxes and soil moisture, as well as the relative importance of boundary layer uptakes seasonally.

For flash floods in the Appalachians (Region 6), latent heat flux and SST anomalies were largest in SON, when tropical cyclone activity is most likely to affect the region. Uptakes in the winter are largely confined to the Atlantic Ocean, whereas in summer, uptakes occur across the CONUS, keeping with the same pattern of anomalies as in Regions 4 and 5 east of the Mississippi River. Most of the moisture for flash floods in the region is from source regions either over the Atlantic Ocean, Gulf of Mexico, or the Southeast US.

Extensions of this work could include adding more cases beyond 2013 or before 2007 to increase the sample size for the number of events used in this study and to increase the number of regions studied. Error analysis could include running the backward trajectories with different reanalysis data (including global reanalysis data to extend the backward trajectories slightly further in time to ~10 days or so), using different land surface models or the NLDAS dataset to account for uncertainty in the parameterization of the land surface. Other models include those with dynamic vegetation to assess how the moisture source climatology might change with agricultural changes, especially for the Missouri Valley cases. Additional endeavors could include the lagged releases of parcels, with trajectories being launched throughout the course of a flash flood event.

Regions with complex terrain are especially vulnerable to natural hazards such as flash flooding, landslides, and debris flows, given the short concentration time in small headwater catchments and the orographic effects on precipitation. Data from the deployment of a mobile X-band radar from the NSSL (NOXP) were used to investigate a case of precipitation impinging on terrain, a situation which can sometimes result in flash flooding. The windward slopes of the Smoky Mountains show a climatological maximum in precipitation, and there is a sharp gradient in precipitation across this region.

Along the ridgeline, signatures of riming of ice particles and larger drops below the melting layer were observed, and these signatures are absent over the valley.

Examining reflectivity and differential reflectivity suggest the presence of a greater concentration of supercooled water from 4-6 km above sea level over the ridgeline, possibly due to sustained and enhanced updrafts of moist air controlled by the topography. Along the ridge, the change in Z and ZDR plotted in KR parameter space suggests a regime dominated by coalescence below the bright band, while there is no dominant signal of one microphysical regime over another over the valley. The observations, albeit from one case, suggest that landform may control not only where convection forms but may exert its influence over the microphysical properties of the precipitation as well.

The IPHEx work could be extended using more cases from different field campaigns to see if the similar signatures of enhanced aggregation and presence of supercooled water are observed on the ridgelines. Unfortunately, RHIs were somewhat limited for the IPHEx case, but PPIs could be used to further investigate the reflectivity profiles observed on the 27 May 2014 case.

In summary, this work seeks to further the knowledge of land-atmosphere interactions and how these interactions exert their effects on flood-producing storms by assessing the moisture sources for flash flood events in the United States. Considering both local and nonlocal effects of the land surface are an important step in forecasting flash floods, not only for the hydrological response of the land surface, but in assessing potential moisture sources for the production of heavy rainfall. As the forecasting paradigm for flash floods shifts to include direct simulation of the land surface and both surface and surface subsurface flows, it is important that forecasters consider these effects when producing forecasts for heavy rainfall and flash flooding.

References

Adams, D. K., and A. C. Comrie, 1997: The North American Monsoon. *Bull. Am. Meteorol. Soc.*, **78**, 2197–2213, doi:10.1175/1520-0477(1997)078<2197:TNAM>2.0.CO;2.

Anagnostou, M. N., J. Kalogiros, F. S. Marzano, E. N. Anagnostou, M. Montopoli, and E. Piccioti, 2013: Performance Evaluation of a New Dual-Polarization Microphysical Algorithm Based on Long-Term X-Band Radar and Disdrometer Observations. *J. Hydrometeorol.*, **14**, 560–576, doi:10.1175/JHM-D-12-057.1.

Arnault, J., R. Knoche, J. Wei, and H. Kunstmann, 2016: Evaporation tagging and atmospheric water budget analysis with WRF: A regional precipitation recycling study for West Africa. *Water Resour. Res.*, **52**, 1544-1567, doi:10.1002/2015WR017704.

Ashley, S. T., and W. S. Ashley, 2008: Flood fatalities in the United States. *J. Appl. Meteorol. Climatol.*, **47**, 805–818, doi:10.1175/2007JAMC1611.1.

Baeck, M. L., and J. A. Smith, 1998: Rainfall estimation by the WSR-88D for heavy rainfall events. *Weather Forecast.*, **13**, 416–436, doi:10.1175/1520-0434(1998)013<0416:REBTWF>2.0.CO;2.

Baker, V. R., 1975: Flood Hazards along the Balcones Escarpment in Central Texas Alternative Approaches to their Recognition, Mapping, and Management. *Geol. Circ.*, **75**, 1–20. http://www.lib.utexas.edu/books/landscapes/publications/txu-oclc-1967634/txu-oclc-1967634.pdf.

Barros, A.P., Petersen, W., Schwaller, M., Cifelli, R., Mahoney, K., Peters-Liddard, C., Shepherd, M., Nesbitt, S., Wolff, D., Heymsfield, G., Starr, D., Anognostou, E., Gourley, J.J., Kim, E., Krajewski, W., Lackman, G., Lang, T., Miller, D., Mace, G., Petters, M., Smith, J., Tao, W.-K., Tsay, S.-C., and Zipser, E., 2014: NASA GPM-Ground Validation: Integrated Precipitation and Hydrology Experiment 2014 Science Plan. NASA. Text. http://dx.doi.org/10.7924/G8CC0XMR

Beck, J., and C. Weiss, 2012: An Assessment of Low-Level Baroclinity and Vorticity Within A Simulated Supercell. *Mon. Weather Rev.*, 120803125110003, doi:10.1175/MWR-D-11-00115.1.

Betten, D. P., M. I. Biggerstaff, and L. J. Wicker, 2017: A trajectory mapping technique for the visualization and analysis of three-dimensional flow in supercell storms. *J. Atmos. Ocean. Technol.*, **34**, 33–49, doi:10.1175/JTECH-D-16-0043.1.

Braud, I., and Coauthors, 2014: Multi-scale hydrometeorological observation and modelling for flash flood understanding. *Hydrol. Earth Syst. Sci.*, **18**, 3733–3761, doi:10.5194/hess-18-3733-2014.

Brooks, H. E., and D. J. Stensrud, 2000: Climatology of Heavy Rain Events in the United States from Hourly Precipitation Observations. *Mon. Weather Rev.*, **128**, 1194–1201, doi:10.1175/1520-0493(2000)128<1194:COHREI>2.0.CO;2.

Brubaker, K. L., and Coauthors, 2001: A 36-yr Climatological Description of the Evaporative Sources of Warm-Season Precipitation in the Mississippi River Basin. *J. Hydrometeorol.*, **2**, 537–557, doi:10.1175/1525-7541(2001)002<0537:AYCDOT>2.0.CO;2.

Caran, S. C., and V. R. Baker, 1986: Balcones Escarpment. *The Balcones Escarpment, Central Texas*, P.L. Abbot and C.M.J. Woodruff, Eds., Geological Society of America, 1–14 http://lib.utexas.edu/geo/balcones_escarpment/contents.html.

Caracena, F., R. A. Maddox, L. R. Hoxit, and C. F. Chappell, 1979: Mesoanalysis of the Big Thompson Storm. *Mon. Weather Rev.*, **107**, 1–17, doi:10.1175/1520-0493(1979)107<0001:MOTBTS>2.0.CO;2.

Carbone, R. E., and J. D. Tuttle, 2008: Rainfall Occurrence in the U.S. Warm Season: The Diurnal Cycle*. *J. Clim.*, **21**, 4132–4146, doi:10.1175/2008JCLI2275.1.

Carr, N., P. E. Kirstetter, J. J. Gourley, and Y. Hong, 2017: Polarimetric Signatures of Midlatitude Warm-Rain Precipitation Events. *J. Appl. Meteorol. Climatol.*, **56**, 697–711, doi:10.1175/JAMC-D-16-0164.1.

Chandrasekar, V., M. Schwaller, M. Vega, J. Carswell, K. V. Mishra, R. Meneghini, and C. Nguyen, 2010: Scientific and engineering overview of the NASA Dual-Frequency Dual-Polarized Doppler Radar (D3R) system for GPM ground validation. *Int. Geosci. Remote Sens. Symp.*, 1308–1311, doi:10.1109/IGARSS.2010.5649440.

Chen, F., and Coauthors, 1996: Modeling of land surface evaporation by four schemes and comparison with FIFE observations. *J. Geophys. Res.*, **101**, 7251, doi:10.1029/95JD02165.

——, and J. Dudhia, 2001: Coupling an Advanced Land Surface–Hydrology Model with the Penn State–NCAR MM5 Modeling System. Part II: Preliminary Model Validation. *Mon. Weather Rev.*, **129**, 587–604, doi:10.1175/1520-0493(2001)129<0587:CAALSH>2.0.CO;2.

Clark, R. A., J. J. Gourley, Z. L. Flamig, Y. Hong, and E. Clark, 2014: CONUS-Wide Evaluation of National Weather Service Flash Flood Guidance Products. *Weather Forecast.*, **29**, 377–392, doi:10.1175/WAF-D-12-00124.1.

Coleman, J. S. M., and D. Budikova, 2010: Atmospheric aspects of the 2008 Midwest floods: A repeat of 1993? *Int. J. Climatol.*, **30**, 1645–1667, doi:10.1002/joc.2009.

Cook, K. H., and E. K. Vizy, 2010: Hydrodynamics of the Caribbean low-level jet and its relationship to precipitation. *J. Clim.*, **23**, 1477–1494, doi:10.1175/2009JCLI3210.1.

Cosby, B. J., G. M. Hornberger, R. B. Clapp, and T. R. Ginn, 1984: A Statistical Exploration of the Relationships of Soil Moisture Characteristics to the Physical Properties of Soils. *Water Resour. Res.*, **20**, 682–690, doi:10.1029/WR020i006p00682.

Costa, J. E., 1987: Hydraulics and basin morphometry of the largest flash floods in the conterminous United States. *J. Hydrol.*, **93**, 313–338, doi:10.1016/0022-1694(87)90102-8. http://linkinghub.elsevier.com/retrieve/pii/0022169487901028.

Daly, C., M. Halbleib, J. I. Smith, W. P. Gibson, M. K. Doggett, G. H. Taylor, J. Curtis, and P. P. Pasteris, 2008: Physiographically sensitive mapping of climatological temperature and precipitation across the conterminous United States. *Int. J. Climatol.*, **28**, 2031–2064, doi:10.1002/joc.1688. http://cdiac.esd.ornl.gov/oceans/GLODAP/glodap_pdfs/Thermohaline.web.pdf.

——, P. Neilson, and D. L. Phillips, 1994: A Statistical-Topographic Model for Mapping Climatological Precipitation over Mountainous Terrain. *J. Appl. Meteorol.*, **33**, 140–158, doi:10.1175/1520-0450(1994)033<0140:ASTMFM>2.0.CO;2.

DeAngelis, A., F. Dominguez, Y. Fan, A. Robock, M. D. Kustu, and D. Robinson, 2010: Evidence of enhanced precipitation due to irrigation over the Great Plains of the United States. *J. Geophys. Res. Atmos.*, **115**, 1–14, doi:10.1029/2010JD013892.

Dickinson, A., Henderson-Sellers, and P. J. Kennedy, 1993: Biosphere-Atmosphere Transfer Scheme (BATS) Version 1e as coupled to the NCAR Community Climate Model. NCAR Tech. Note NCAR/TN-387+STR, 72 pp.

Dirmeyer, P. A., and J. L. Kinter, 2009: The “Maya Express”: Floods in the U.S. Midwest. *Eos (Washington. DC).*, **90**, 101–102, doi:10.1029/2009EO120001.

——, and ——, 2010: Floods over the U.S. Midwest: A Regional Water Cycle Perspective. *J. Hydrometeorol.*, **11**, 1172–1181, doi:10.1175/2010JHM1196.1. http://dx.doi.org/10.1175/2010JHM1196.1.

——, and K. L. Brubaker, 1999: Contrasting evaporative moisture sources during the drought of 1988 and the flood of 1993. *J. Geophys. Res.*, **104**, 19383.

Doswell, C.A., H. E. Brooks, and R. A. Maddox, 1996: Flash flood forecasting: An ingredients-based methodology. *Weather Forecast.*, **11**, 560–581, doi:10.1175/1520-0434(1996)011<0560:FFFAIB>2.0.CO;2.

Draxler, R. R., 2003: Evaluation of an Ensemble Dispersion Calculation. *J. Appl. Meteorol.*, **42**, 308–317, doi:10.1175/1520-0450(2003)042<0308:EOAEDC>2.0.CO;2.

Drumond, A., R. Nieto, L. Gimeno, and T. Ambrizzi, 2008: A Lagrangian identification of major sources of moisture over Central Brazil and la Plata Basin. *J. Geophys. Res. Atmos.*, **113**, 1–9, doi:10.1029/2007JD009547.

Duan, Y., A. M. Wilson, and A. P. Barros, 2015: Scoping a field experiment: Error diagnostics of TRMM precipitation radar estimates in complex terrain as a basis for IPHEx2014. *Hydrol. Earth Syst. Sci.*, **19**, 1501–1520, doi:10.5194/hess-19-1501-2015.

Durkee, J. D., L. Campbell, K. Berry, D. Jordan, G. Goodrich, R. Mahmood, and S. Foster, 2012: A synoptic perspective of the record 1-2 May 2010 mid-south heavy precipitation event. *Bull. Am. Meteorol. Soc.*, **93**, 611–620, doi:10.1175/BAMS-D-11-00076.1.

Ek, M. B., 2005: Interactions of the land-surface with the atmospheric boundary layer. Ph. D. Thesis, Wageningen University, Wageningen, Gelderland, The Netherlands, 210 pp.

——, and A. A. M. Holtslag, 2004: Influence of Soil Moisture on Boundary Layer Cloud Development. *J. Hydrometeorol.*, **5**, 86–99, doi:10.1175/1525-7541(2004)005<0086:IOSMOB>2.0.CO;2.

——, K. E. Mitchell, Y. Lin, E. Rogers, P. Grunmann, V. Koren, G. Gayno, and J. D. Tarpley, 2003: Implementation of Noah land surface model advances in the National Centers for Environmental Prediction operational mesoscale Eta model. *J. Geophys. Res. Atmos.*, **108**(D22), 8851, doi:10.1029/2002JD003296.

——, and L. Mahrt, 1991: OSU 1-D PBL model user's guide. Version 1.04, 120 pp. [Available from Department of Atmospheric Sciences, Oregon State University, Corvallis, OR 97331-2209.].

——, and ——, 1994: Daytime Evolution of Relative Humidity at the Boundary Layer Top. *Mon. Weather Rev.*, **122**, 2709–2721, doi:10.1175/1520-0493(1994)122<2709:DEORHA>2.0.CO;2.

Erlingis, J. M., and A. P. Barros, 2014: A Study of the Role of Daytime Land–Atmosphere Interactions on Nocturnal Convective Activity in the Southern Great Plains during CLASIC. *J. Hydrometeorol.*, **15**, 1932–1953, doi:10.1175/JHM-D-14-0016.1.

Findell, K. L., and E. A. B. Eltahir, 2003: Atmospheric Controls on Soil Moisture–Boundary Layer Interactions. Part I: Framework Development. *J. Hydrometeorol.*, **4**, 552–569, doi:10.1175/1525-7541(2003)004<0552:ACOSML>2.0.CO;2.

Friedrich, K., E. a. Kalina, J. Aikins, D. Gochis, and R. Rasmussen, 2015: Precipitation and cloud structures of intense rain during the 2013 Great Colorado Flood. *J. Hydrometeorol.*, 150408113718006, doi:10.1175/JHM-D-14-0157.1. http://journals.ametsoc.org/doi/abs/10.1175/JHM-D-14-0157.1.

Friedrich, K., E. a. Kalina, J. Aikins, M. Steiner, D. Gochis, P. a. Kucera, K. Ikeda, and J. Sun, 2015: Raindrop size distribution and rain characteristics during the 2013 Great Colorado Flood. *J. Hydrometeorol.*, 150526130654002, doi:10.1175/JHM-D-14-0184.1.

Fuhrmann, C. M., and C. E. Konrad, 2013: A Trajectory Approach to Analyzing the Ingredients Associated with Heavy Winter Storms in Central North Carolina. *Weather Forecast.*, **28**, 647–667, doi:10.1175/WAF-D-12-00079.1.

Galewsky, J., A. Sobel, and I. Held, 2005: Diagnosis of Subtropical Humidity Dynamics Using Tracers of Last Saturation. *J. Atmos. Sci.*, **62**, 3353–3367, doi:10.1175/JAS3533.1.

Gaume, E., and Coauthors, 2009: A compilation of data on European flash floods. *J. Hydrol.*, **367**, 70–78, doi:10.1016/j.jhydrol.2008.12.028.

Gleason, K. L., J. H. Lawrimore, D. H. Levinson, T. R. Karl, and D. J. Karoly, 2008: A revised U.S. Climate Extremes Index. *J. Clim.*, **21**, 2124–2137, doi:10.1175/2007JCLI1883.1.

Gochis, D., and Coauthors, 2015: The great Colorado flood of September 2013. *Bull. Am. Meteorol. Soc.*, **96**, 1461–1487, doi:10.1175/BAMS-D-13-00241.1.

Gourley, J. J., J. M. Erlingis, Y. Hong, and E. B. Wells, 2012: Evaluation of Tools Used for Monitoring and Forecasting Flash Floods in the United States. *Weather Forecast.*, **27**, 158–173, doi:10.1175/WAF-D-10-05043.1. http://journals.ametsoc.org/doi/abs/10.1175/WAF-D-10-05043.1.

——, and Coauthors, 2013: A unified flash flood database across the United States. *Bull. Am. Meteorol. Soc.*, **94**, 799–805, doi:10.1175/BAMS-D-12-00198.1.

Grams, H. M., J. Zhang, and K. L. Elmore, 2014: Automated Identification of Enhanced Rainfall Rates Using the Near-Storm Environment for Radar Precipitation Estimates. *J. Hydrometeorol.*, **15**, 1238–1254, doi:10.1175/JHM-D-13-042.1.

Groisman, P. Y., and Coauthors, 2005: Contemporary Changes of the Hydrological Cycle over the Contiguous United States: Trends Derived from In Situ Observations. *J. Hydrometeorol.*, **5**, 64–85, doi:10.1175/1525-7541(2004)005<0064:CCOTHC>2.0.CO;2.

Groisman, P. Y., R. W. Knight, and T. R. Karl, 2012: Changes in Intense Precipitation over the Central United States. *J. Hydrometeorol.*, **13**, 47–66, doi:10.1175/JHM-D-11-039.1. https://doi.org/10.1175/JHM-D-11-039.1.

Hanks, R. J., and G. L. Ashcroft, 1986: Applied Soil Physics. Springer-Verlag, 159 pp.

Hardy, J., J. J. Gourley, P. E. Kirstetter, Y. Hong, F. Kong, and Z. L. Flamig, 2016: A method for probabilistic flash flood forecasting. *J. Hydrol.*, **541**, 480–494, doi:10.1016/j.jhydrol.2016.04.007.

Hardy, S., D. M. Schultz, and G. Vaughan, 2017: Early Evolution of the 23–26 September 2012 U.K. Floods: Tropical Storm Nadine and Diabatic Heating due to Cloud Microphysics. *Mon. Weather Rev.*, **145**, 543–563, doi:10.1175/MWR-D-16-0200.1.

Helmus, J. J., and S. M. Collis, 2016: The Python ARM Radar Toolkit (Py-ART), a Library for Working with Weather Radar Data in the Python Programming Language. **4**, e25.

Hicks, N. S., J. A. Smith, A. J. Miller, and P. A. Nelson, 2005: Catastrophic flooding from an orographic thunderstorm in the central Appalachians. *Water Resour. Res.*, **41**, 1–17, doi:10.1029/2005WR004129.

Higgins, R. W., Y. Yao, and X. L. Wang, 1997: Influence of the North American monsoon system on the U.S. summer precipitation regime. *J. Clim.*, **10**, 2600–2622, doi:10.1175/1520-0442(1997)010<2600:IOTNAM>2.0.CO;2.

Hillel, D., 1982: *Introduction to Soil Physics*. Academic Press, 392 pp.

Hou, A. Y., and Coauthors, 2014: The global precipitation measurement mission. *Bull. Am. Meteorol. Soc.*, **95**, 701–722, doi:10.1175/BAMS-D-13-00164.1.

Illingworth, A. J., and T. M. Blackman, 2001: The need to represent raindrop size spectra as normalized gamma distributions for the interpretation of polarimetric radar observations. *J. Appl. Meteorol.*, **41**, 286–297, doi:10.1175/1520-0450(2003)042<1184:COTNTR>2.0.CO;2.

Kalogiros, J., M. N. Anagnostou, E. N. Anagnostou, M. Montopoli, E. Picciotti, and F. S. Marzano, 2013: Correction of polarimetric radar reflectivity measurements and rainfall estimates for apparent vertical profile in stratiform rain. *J. Appl. Meteorol. Climatol.*, **52**, 1170–1186, doi:10.1175/JAMC-D-12-0140.1.

——, M.N. Anagnostou, E.N. Anagnostou, M. Montopoli, E. Picciotti, and F.S. Silvio Marzano, 2014: Evaluation of a new polarimetric algorithm for rain-path attenuation correction of X-band radar observations against disdrometer data. *IEEE Geosci. Remote Sens.* **52**, 1369-1380.

Koster, R. D., 2004: Regions of Strong Coupling Between Soil Moisture and Precipitation. *Science (80-.).*, **305**, 1138–1140, doi:10.1126/science.1100217.

Kumjian, M. R., and A. V. Ryzhkov, 2010: The impact of evaporation on polarimetric characteristics of rain: Theoretical model and practical implications. *J. Appl. Meteorol. Climatol.*, **49**, 1247–1267, doi:10.1175/2010JAMC2243.1.

——., and O. P. Prat, 2014: The Impact of Raindrop Collisional Processes on the Polarimetric Radar Variables. *J. Atmos. Sci.*, **71**, 3052–3067, doi:10.1175/JAS-D-13-0357.1. http://journals.ametsoc.org/doi/abs/10.1175/JAS-D-13-0357.1.

——, S. Mishra, S. E. Giangrande, T. Toto, A. V. Ryzhkov, and A. Bansemer, 2016: Polarimetric radar and aircraft observations of saggy bright bands during MC3E. *J. Geophys. Res. Atmos.*, **121**, 3584–3607, doi:10.1002/2015JD024446.

Kustu, M. D., Y. Fan, and M. Rodell, 2011: Possible link between irrigation in the U.S. High Plains and increased summer streamflow in the Midwest. *Water Resour. Res.*, **47**, doi:10.1029/2010WR010046.

Lavers, D. A., and G. Villarini, 2013: Atmospheric rivers and flooding over the central United States. *J. Clim.*, **26**, 7829–7836, doi:10.1175/JCLI-D-13-00212.1.

Li, L., R. W. Schmitt, C. C. Ummenhofer, and K. B. Karnauskas, 2016: Implications of North Atlantic sea surface salinity for summer precipitation over the U.S. Midwest: Mechanisms and predictive value. *J. Clim.*, **29**, 3143–3159, doi:10.1175/JCLI-D-15-0520.1.

Luo, Y., E. H. Berbery, K. E. Mitchell, and A. K. Betts, 2007: Relationships between Land Surface and Near-Surface Atmospheric Variables in the NCEP North American Regional Reanalysis. *J. Hydrometeorol.*, **8**, 1184–1203, doi:10.1175/2007JHM844.1.

Lynn, B. H., W.-K. Tao, and P. J. Wetzel, 1998: A Study of Landscape-Generated Deep Moist Convection. *Mon. Weather Rev.*, **126**, 928–942, doi:10.1175/1520-0493(1998)126<0928:ASOLGD>2.0.CO;2.

Maddox, R. A., C. F. Chappell, and L. R. Hoxit, 1979: Synoptic and Meso-α Scale Aspects of Flash Flood Events. *Bull. Am. Meteorol. Soc.*, **60**, 115–123, doi:10.1175/1520-0477-60.2.115.

——, D. M. McCollum, and K. W. Howard, 1995: Large-Scale Patterns Associated with Severe Summertime Thunderstorms over Central Arizona. *Weather Forecast.*, **10**, 763–778, doi:10.1175/1520-0434(1995)010<0763:LSPAWS>2.0.CO;2.

——, F. Canova, and R. L. Hoxit, 1980: Meteorological Characteristics of Flash Floods Events over the Western United States. *Mon. Wather Rev.*, **108**, 1866–1877, doi:10.1175/1520-0493(1980)108<1866:MCOFFE>2.0.CO;2.

—— L. R. Hoxit, C. F. Chappell, and F. Caracena, 1978: Comparison of Meteorological Aspects of the Big Thompson and Rapid City Flash Floods.

Mon. Weather Rev., **106**, 375–389, doi:10.1175/1520-0493(1978)106<0375:COMAOT>2.0.CO;2.

Mahrt, L., J. Sun, D. Vickers, J. I. Macpherson, J. R. Pederson, and R. L. Desjardins, 1994: Observations of Fluxes and Inland Breezes over a Heterogeneous Surface. *J. Atmos. Sci.*, **51**, 2484–2499, doi:10.1175/1520-0469(1994)051<2484:OOFAIB>2.0.CO;2.

Marquis, J., Y. Richardson, P. Markowski, J. Wurman, K. Kosiba, and P. Robinson, 2016: Analysis of the 5 June 2009 Goshen County, Wyoming, tornadic supercell through EnKF assimilation of mobile mesonet and radar observations. Part II: mesocyclone-scale processes affecting tornado formation, maintenance, and decay. *Mon. Weather Rev.,* **144**, 3441-3463. doi:10.1175/MWR-D-15-0411.1.

Mesinger, F., and Coauthors, 2006: North American regional reanalysis. *Bull. Am. Meteorol. Soc.*, **87**, 343–360, doi:10.1175/BAMS-87-3-343.

Mitchell, D. L., D. Ivanova, and N. Severe, 2002: Gulf of California Sea Surface Temperatures and the North American Monsoon : Mechanistic Implications from Observations. *J. Clim.*, **15**, 2261–2281, doi:10.1175/1520-0442(2002)015<2261:GOCSST>2.0.CO;2.

Mo, K. C., J. N. Paegle, and R. W. Higgins, 1997: Atmospheric processes associated with summer floods and droughts in the central United States. *J. Clim.*, **10**, 3028–3046, doi:10.1175/1520-0442(1997)010<3028:APAWSF>2.0.CO;2.

Moore, B. J., P. J. Neiman, F. M. Ralph, and F. E. Barthold, 2012: Physical Processes Associated with Heavy Flooding Rainfall in Nashville, Tennessee, and Vicinity during 1–2 May 2010: The Role of an Atmospheric River and Mesoscale Convective Systems. *Mon. Weather Rev.*, **140**, 358–378, doi:10.1175/MWR-D-11-00126.1.

NOAA National Centers for Environmental Information (NCEI) U.S. Billion-Dollar Weather and Climate Disasters (2017). Accessed 01 June 2017 [Available online at https://www.ncdc.noaa.gov/billions/]

National Weather Service (NWS), 2009: NWS Glossary. NOAA/NWS. Accessed 22 June 2017. [Available online at http://w1.weather.gov/glossary/.]

NWS, 2009: Service assessment: Central United States Flooding of June 2008. [Available online at https://www.weather.gov/media/publications/assessments/central_flooding09.pdf]

——, 2011: Service Assesment: Record Floods of Greater Nashville: Including Flooding in Middle Tennessee and Western Kentucky, May 1-4,2010. [Available online at https://www.weather.gov/media/publications/assessments/Tenn_Flooding.pdf]

——, 2012: National Weather Service Manual 10-950 Operations and Services Hydrologic Services Program, NWSPD 10-9. [Available online at http://www.nws.noaa.gov/directives/sym/pd01009050curr.pdf.]

Neiman, P. J., F. M. Ralph, G. a. Wick, J. D. Lundquist, and M. D. Dettinger, 2008: Meteorological Characteristics and Overland Precipitation Impacts of Atmospheric Rivers Affecting the West Coast of North America Based on Eight Years of SSM/I Satellite Observations. *J. Hydrometeorol.*, **9**, 22–47, doi:10.1175/2007JHM855.1.

Nemunaitis, K. L., 2014: Observational and Model Analyses of the Oklahoma City Urban Heat Island, Ph. D. Dissertation, School of Meteorology, University of Oklahoma, Norman, 223 pp..

Nielsen, E. R., R. S. Schumacher, and A. M. Keclik, 2016: The Effect of the Balcones Escarpment on Three Cases of Extreme Precipitation in Central Texas. *Mon. Weather Rev.*, **144**, 119–138, doi:10.1175/Mwr-D-15-0156.1.

Nieto, R., L. Gimeno, and R. M. Trigo, 2006: A Lagrangian identification of major sources of Sahel moisture. *Geophys. Res. Lett.*, **33**, 1–6, doi:10.1029/2006GL027232.

Noilhan, J., and S. Planton, 1989: A Simple Parameterization of Land Surface Processes for Meteorological Models. *Mon. Weather Rev.*, **117**, 536–549, doi:10.1175/1520-0493(1989)117<0536:ASPOLS>2.0.CO;2.

Ogden, F. L., H. O. Sharif, S. U. S. Senarath, J. A. Smith, M. L. Baeck, and J. R. Richardson, 2000: Hydrologic analysis of the Fort Collins, Colorado, flash flood of 1997. *J. Hydrol.*, **228**, 82–100, doi:10.1016/S0022-1694(00)00146-3.

Pan, H. L., and L. Mahrt, 1987: Interaction between soil hydrology and boundary-layer development. *Boundary-Layer Meteorol.*, **38**, 185–202, doi:10.1007/BF00121563.

Petersen, W. A., and Coauthors, 1999: Mesoscale and radar observations of the Fort Collins flash flood of 28 July 1997. *Bull. Am. Meteorol. Soc.*, **80**, 191–216, doi:10.1175/1520-0477(1999)080<0191:MAROOT>2.0.CO;2.

Pielke, R. A., 2001: Influence of the spatail distribution of vegetation and soils on the predictions of cumulus convective rainfall. *Rev. Geophys.*, **39**, 151–177, doi:10.1029/1999RG000072.

Pontrelli, M. D., G. Bryan, and J. M. Fritsch, 1999: The Madison County, Virginia, Flash Flood of 27 June 1995. *Weather Forecast.*, **14**, 384–404, doi:10.1175/1520-0434(1999)014<0384:TMCVFF>2.0.CO;2.

Prat, O. P., and A. P. Barros, 2010: Ground observations to characterize the spatial gradients and vertical structure of orographic precipitation - Experiments in the inner region of the Great Smoky Mountains. *J. Hydrol.*, **391**, 141–156, doi:10.1016/j.jhydrol.2010.07.013.

Ralph, F. M., P. J. Neiman, and G. A. Wick, 2004: Satellite and CALJET Aircraft Observations of Atmospheric Rivers over the Eastern North Pacific Ocean during the Winter of 1997/98. *Mon. Weather Rev.*, **132**, 1721–1745, doi:10.1175/1520-0493(2004)132<1721:SACAOO>2.0.CO;2.

——, P. J. Neiman, G. A. Wick, S. I. Gutman, M. D. Dettinger, D. R. Cayan, and A. B. White, 2006: Flooding on California's Russian River: Role of atmospheric rivers. *Geophys. Res. Lett.*, **33**, 3–7, doi:10.1029/2006GL026689.

Rasmusson, E. M., 1967: Atmospheric water vapor transport and the water balance of North America. Part I. Characteristics of the water vapor flux field. *Mon. Weather Rev.*, **95**, 403–426, doi:10.1175/1520-0493(1967)095<0403:AWVTAT>2.3.CO;2.

Roberts, N. M., S. J. Cole, R. M. Forbes, R. J. Moore, and D. Boswellc, 2009: Use of high-resolution NWP rainfall and river flow forecasts for advance warning of the Carlisle flood, north-west England. *Meteorol. Appl.*, **16**, 23–34, doi:10.1002/met.94.

Rogers, E., M. Ek, Y. Lin, K. Mitchell, D. Parrish, and G. DiMego, Changes to the NCEP Meso Eta analysis and forecast system: Assimilation of observed precipitation, upgrades to land-surface physics, modified 3DVAR analysis, Tech. Proc. Bull. 479, Natl. Weather Serv., Natl. Oceanic and Atmos. Admin., Silver Spring, Md., 2001. (Available at http://www.nws.noaa.gov/om/tpb/inddraft.htm)

Saharia, M., P. Kirstetter, H. Vergara, J. J. Gourley, Y. Hong, and M. Giroud, 2017: Mapping Flash Flood Severity in the United States. *J. Hydrometeorol.*, **18**, 397–411, doi:10.1175/JHM-D-16-0082.1.

Schaake, J. C., V. I. Koren, and Q. Y. Duan, 1996: Simple water balance model for estimating runoff at different spatial and temporal scales. *J. Geophys. Res.*, **101**, 7461–7475.

Schroeder, A. J., and Coauthors, 2016a: The development of a flash flood severity index. *J. Hydrol.*, **541**, 523–532, doi:10.1016/j.jhydrol.2016.04.005.

——, J. Basara, J. Marshall Shepherd, and S. Nelson, 2016b: Insights into atmospheric contributors to urban flash flooding across the United States using an analysis of rawinsonde data and associated calculated parameters. *J. Appl. Meteorol. Climatol.*, **55**, 313–323, doi:10.1175/JAMC-D-14-0232.1.

Schumacher, R. S., and R. H. Johnson, 2005: Organization and Environmental Properties of Extreme-Rain-Producing Mesoscale Convective Systems. *Mon. Weather Rev.*, **133**, 961–976, doi:10.1175/MWR2899.1.

—— and ——, 2006: Characteristics of U . S . Extreme Rain Events during 1999 – 2003. *Weather Forecast.*, **21**, 69–85, doi:http://dx.doi.org/10.1175/WAF900.1. http://journals.ametsoc.org/doi/abs/10.1175/WAF900.1.

Segal, M., and R. W. Arritt, 1992: Nonclassical Mesoscale Circulations Caused by Surface Sensible Heat-Flux Gradients. *Bull. Am. Meteorol. Soc.*, **73**, 1593–1604, doi:10.1175/1520-0477(1992)073<1593:NMCCBS>2.0.CO;2.

Skamarock, W. C., and Coauthors, 2008: A description of the Advanced Research WRF version 3. NCAR Tech. Note NCAR/TN-4751STR, 113 pp., doi:10.5065/D68S4MVH.

Slater, T. P., D. M. Schultz, and G. Vaughan, 2015: Acceleration of near-surface strong winds in a dry, idealised extratropical cyclone. *Q. J. R. Meteorol. Soc.*, **141**, 1004–1016, doi:10.1002/qj.2417.

Smart, D. J., and K. A. Browning, 2014: Attribution of strong winds to a cold conveyor belt and sting jet. *Q. J. R. Meteorol. Soc.*, **140**, 595–610, doi:10.1002/qj.2162.

Smith, B. L., S. E. Yuter, P. J. Neiman, and D. E. Kingsmill, 2010: Water Vapor Fluxes and Orographic Precipitation over Northern California Associated with a Landfalling Atmospheric River. *Mon. Weather Rev.*, **138**, 74–100, doi:10.1175/2009MWR2939.1.

Smith, J. A., M. L. Baeck, J. E. Morrison, and P. Sturdevant-Rees, 2000: Catastrophic Rainfall and Flooding in Texas. *J. Hydrometeorol.*, **1**, 5–25, doi:10.1175/1525-7541(2000)001<0005:CRAFIT>2.0.CO;2.

——, ——, G. Villarini, and W. F. Krajewski, 2010: The Hydrology and Hydrometeorology of Flooding in the Delaware River Basin. *J. Hydrometeorol.*, **11**, 841–859, doi:10.1175/2010JHM1236.1.

——, ——, A. A. Ntelekos, G. Villarini, and M. Steiner, 2011: Extreme rainfall and flooding from orographic thunderstorms in the central Appalachians. *Water Resour. Res.*, **47**, 1–24, doi:10.1029/2010WR010190.

Sodemann, H., C. Schwierz, and H. Wernli, 2008: Interannual variability of Greenland winter precipitation sources: Lagrangian moisture diagnostic and North Atlantic Oscillation influence. *J. Geophys. Res. Atmos.*, **113**, 1–17, doi:10.1029/2007JD008503.

Sorí, R., A. Drumond, and R. Nieto, 2015: Moisture contribution of the Atlantic Warm Pool to precipitation: a Lagrangian analysis. *Front. Environ. Sci.*, **3**, 1–11, doi:10.3389/fenvs.2015.00022. http://journal.frontiersin.org/Article/10.3389/fenvs.2015.00022/abstract.

Stein, A. F., R. R. Draxler, G. D. Rolph, B. J. B. Stunder, M. D. Cohen, and F. Ngan, 2015: Noaa's hysplit atmospheric transport and dispersion modeling system. *Bull. Am. Meteorol. Soc.*, **96**, 2059–2077, doi:10.1175/BAMS-D-14-00110.1.

Stensrud, D. J., R. L. Gall, S. L. Mullen, and K. W. Howard, 1995: Model climatology of the Mexican monsoon. *J. Clim.*, **8**, 1775–1794, doi:10.1175/1520-0442(1995)008<1775:MCOTMM>2.0.CO;2.

Stoelinga, M.L., 2009: A users' guide to RIP version 4.5: A program for visualizing mesoscale model output. Accessed 01 July 2014. [Available online at http://www2.mmm.ucar.edu/wrf/users/docs/ripug.htm.]

Stohl, A., 1998: Computation, accuracy and applications of trajectories—A review and bibliography. *Atmos. Environ.*, **32**, 947–966, doi:10.1016/S1352-2310(97)00457-3. http://linkinghub.elsevier.com/retrieve/pii/S1352231097004573.

——, and P. James, 2004: A Lagrangian analysis of the atmospheric branch of the global water cycle: Part 1: Method description, validation, and demonstration for the August 2002 flooding in central Europe. *J. Hydrometeorol.*, **5**, 656–678, doi:10.1175/1525-7541(2004)005<0656:ALAOTA>2.0.CO;2.

——, and ——, 2005: A Lagrangian analysis of the atmospheric branch of the global water cycle. Part II: Moisture transports between earth's ocean basins and river catchments. *J. Hydrometeorol.*, **6**, 961–984, doi:10.1175/JHM470.1.

Sturdevant-Rees, P., J. A. Smith, J. Morrison, and M. L. Baeck, 2001: Tropical storms and the flood hydrology of the central Appalachians. *Water Resour. Res.*, **37**, 2143–2168, doi:10.1029/2000WR900310. http://doi.wiley.com/10.1029/2000WR900310.

Sun, B., and H. Wang, 2014: Moisture sources of semiarid grassland in China using the lagrangian particle model FLEXPART. *J. Clim.*, **27**, 2457–2474, doi:10.1175/JCLI-D-13-00517.1.

Tao, J., and A. P. Barros, 2013: Prospects for flash flood forecasting in mountainous regions - An investigation of Tropical Storm Fay in the Southern Appalachians. *J. Hydrol.*, **506**, 68–89, doi:10.1016/j.jhydrol.2013.02.052.

Testud, J., E. Le Bouar, E. Obligis, and M. Ali-Mehenni, 2000: The rain profiling algorithm applied to polarimetric weather radar. *J. Atmos. Ocean. Technol.*, **17**, 332–356, doi:10.1175/1520-0426(2000)017<0332:TRPAAT>2.0.CO;2.

Tilev-Tanriover, S., and A. Kahraman, 2015: Saharan dust transport by Mediterranean cyclones causing mud rain in Istanbul. *Weather*, **70**, 139–145, doi:10.1002/wea.2347.

Trenberth, K. E., and C. J. Guillemot, 1998: Evaluation of the atmospheric moisture and hydrological cycle in the NCEP/NCAR reanalyses. *Clim. Dyn.*, **14**, 213–231, doi:10.1007/s003820050219.

Vergara, H., P. Kirstetter, J. J. Gourley, Z. L. Flamig, Y. Hong, A. Arthur, and R. Kolar, 2016: Estimating a-priori kinematic wave model parameters based on regionalization for flash flood forecasting in the Conterminous United States. *J. Hydrol.*, **541**, 421–433, doi:10.1016/j.jhydrol.2016.06.011.

Villarini, G., and J. A. Smith, 2010: Flood peak distributions for the eastern United States. *Water Resour. Res.*, **46**, 1–17, doi:10.1029/2009WR008395.

——, R. Goska, J. A. Smith, and G. A. Vecchi, 2014: North atlantic tropical cyclones and U.S. flooding. *Bull. Am. Meteorol. Soc.*, **95**, 1381–1388, doi:10.1175/BAMS-D-13-00060.1.

Vincendon, B., V. Ducrocq, O. Nuissier, and B. Vié, 2011: Perturbation of convection-permitting NWP forecasts for flash-flood ensemble forecasting. *Nat. Hazards Earth Syst. Sci.*, **11**, 1529–1544, doi:10.5194/nhess-11-1529-2011.

Vitale, J. D., and T. Ryan, 2013: Operational Recognition of High Precipitation Efficiency and Low-Echo-Centroid Convection. *J. Oper. Meteorol.*, **1**, 128–143.

Wakimoto, R. M., C. Liu, and H. Cai, 1998: The Garden City, Kansas, Storm during VORTEX 95. Part I: Overview of the Storm's Life Cycle and Mesocyclogenesis. *Mon. Weather Rev.*, **126,** 372–392, doi:10.1175/1520-0493(1998)126<0372:TGCKSD>2.0.CO;2.

Wang, S. Y., and T. C. Chen, 2009: The late-spring maximum of rainfall over the U.S. central plains and the role of the low-level jet. *J. Clim.*, **22**, 4696–4709, doi:10.1175/2009JCLI2719.1.

Wernli, H., M. Paulat, M. Hagen, and C. Frei, 2008: SAL—A Novel Quality Measure for the Verification of Quantitative Precipitation Forecasts. *Mon. Weather Rev.*, **136**, 4470–4487, doi:10.1175/2008MWR2415.1.

Wilson, A. M., and A. P. Barros, 2014: An Investigation of Warm Rainfall Microphysics in the Southern Appalachians: Orographic Enhancement via Low-Level Seeder–Feeder Interactions. *J. Atmos. Sci.*, 140124150725001, doi:10.1175/JAS-D-13-0228.1.

——, and ——, 2015: Landform controls on low level moisture convergence and the diurnal cycle of warm season orographic rainfall in the Southern Appalachians. *J. Hydrol.*, **531**, 475–493, doi:10.1016/j.jhydrol.2015.10.068.

Wooten, R. M., K. A. Gillon, A. C. Witt, R. S. Latham, T. J. Douglas, J. B. Bauer, S. J. Fuemmeler, and L. G. Lee, 2008: Geologic, geomorphic, and meteorological aspects of debris flows triggered by Hurricanes Frances and Ivan during

September 2004 in the Southern Appalachian Mountains of Macon County, North Carolina (southeastern USA). *Landslides*, **5**, 31–44, doi:10.1007/s10346-007-0109-9.

Wei, J. H.R. Knoche, and H. Kunstmann, 2016: Atmospheric residence times from transpiration and evaporation to precipitation: An age-weighted regional evaporation tagging approach. *J. Geophys. Res. Atmos.*, **121**, 6841-6862, doi:10.1002/2015JD024650.

Yuter, S. E., and R. a. Houze, 1995: Three-Dimensional Kinematic and Microphysical Evolution of Florida Cumulonimbus. Part II: Frequency Distributions of Vertical Velocity, Reflectivity, and Differential Reflectivity. *Mon. Weather Rev.*, **123**, 1941–1963, doi:10.1175/1520-0493(1995)123<1941:TDKAME>2.0.CO;2.

Zhu, Y., and R. E. Newell, 1998: A Proposed Algorithm for Moisture Fluxes from Atmospheric Rivers. *Mon. Weather Rev.*, **126**, 725–735, doi:10.1175/1520-0493(1998)126<0725:APAFMF>2.0.CO;2.

Appendix A: Additional Figures

This section includes maps similar to those in Chapter 4 but for regions and seasons that were not discussed (or only briefly discussed) in the text.

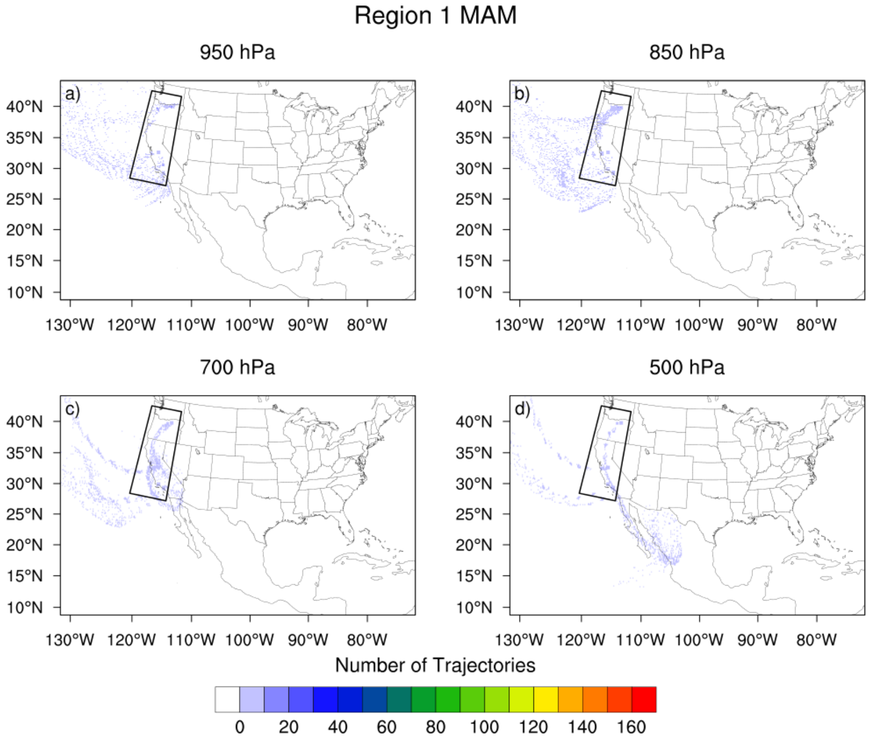

Figure A1. Trajectory density (number of trajectories passing through a grid point) for parcels ending at the approximate pressure level indicated for flash floods occurring in Region 1 (West Coast) during MAM.

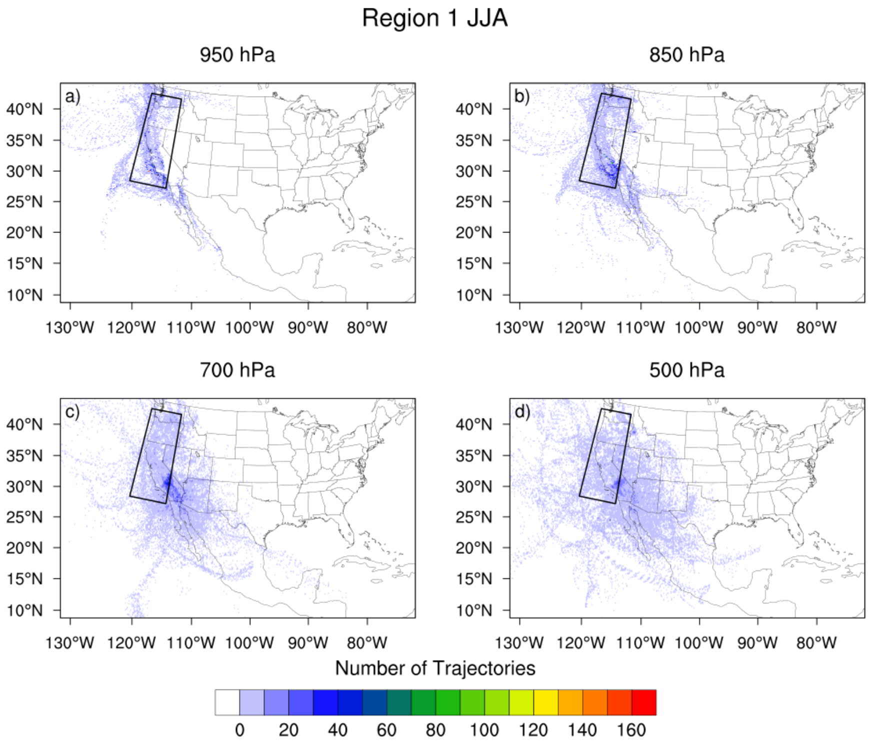

Figure A2. As in Figure A1, but for Region 1 during JJA.

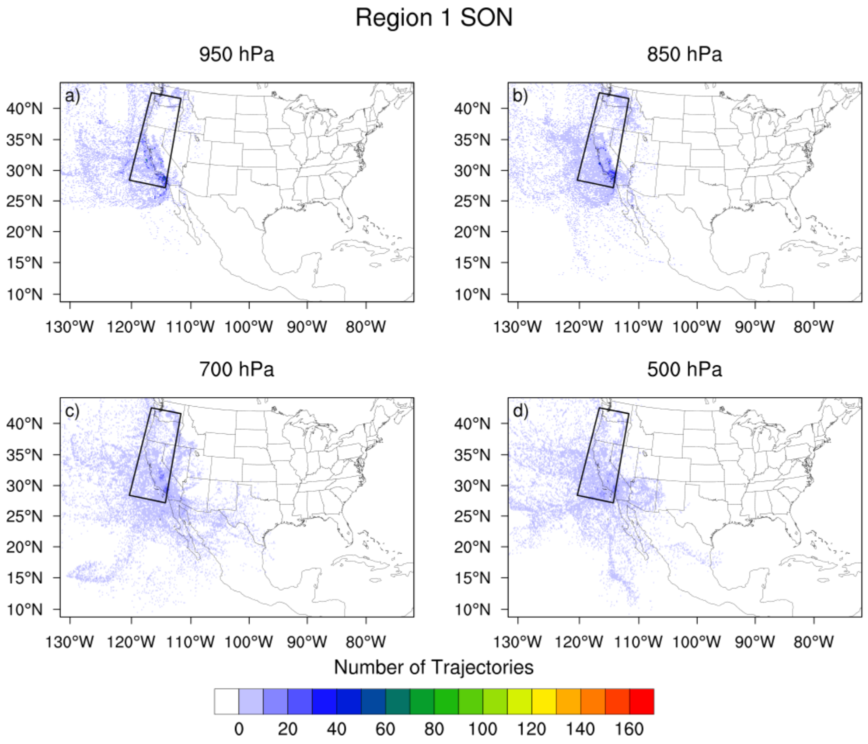

Figure A3. As in Figure A1, but for Region 1 during SON.

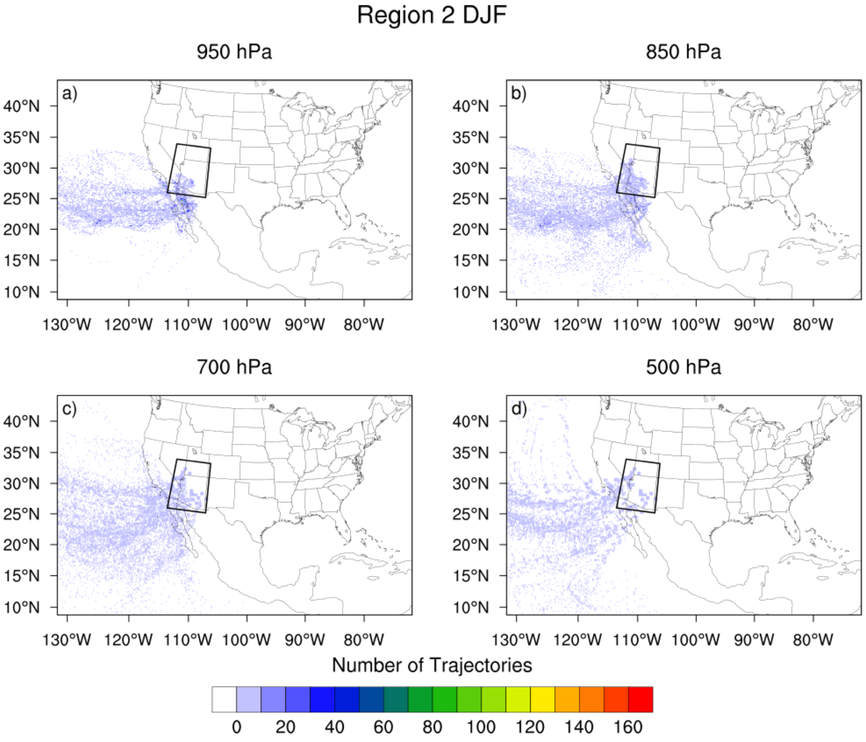

Figure A4. As in Figure A1, but for Region 2 (Arizona) during DJF.

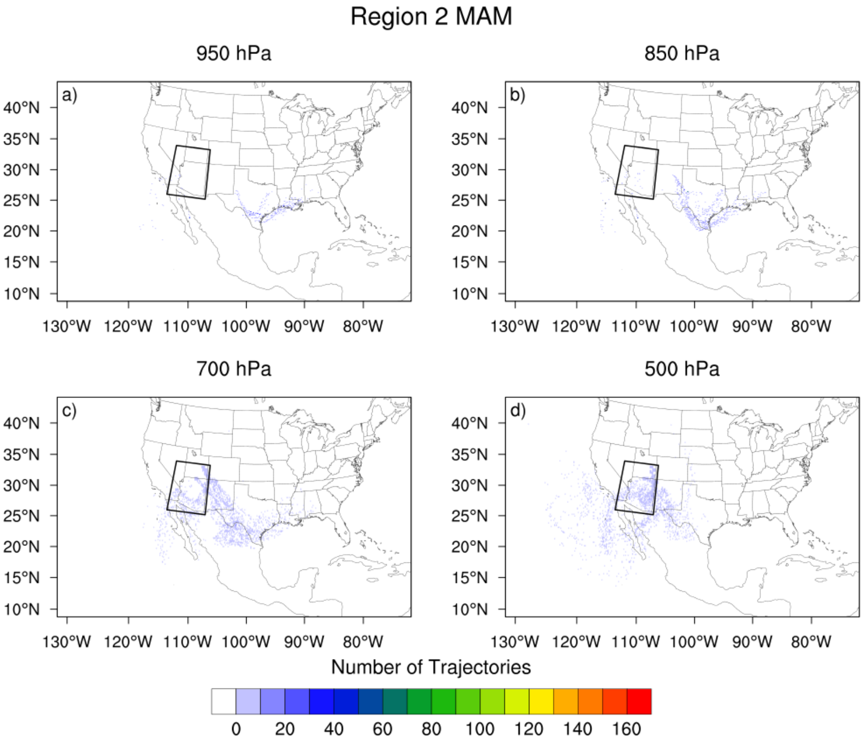

Figure A5. As in Figure A1, but for Region 2 during MAM.

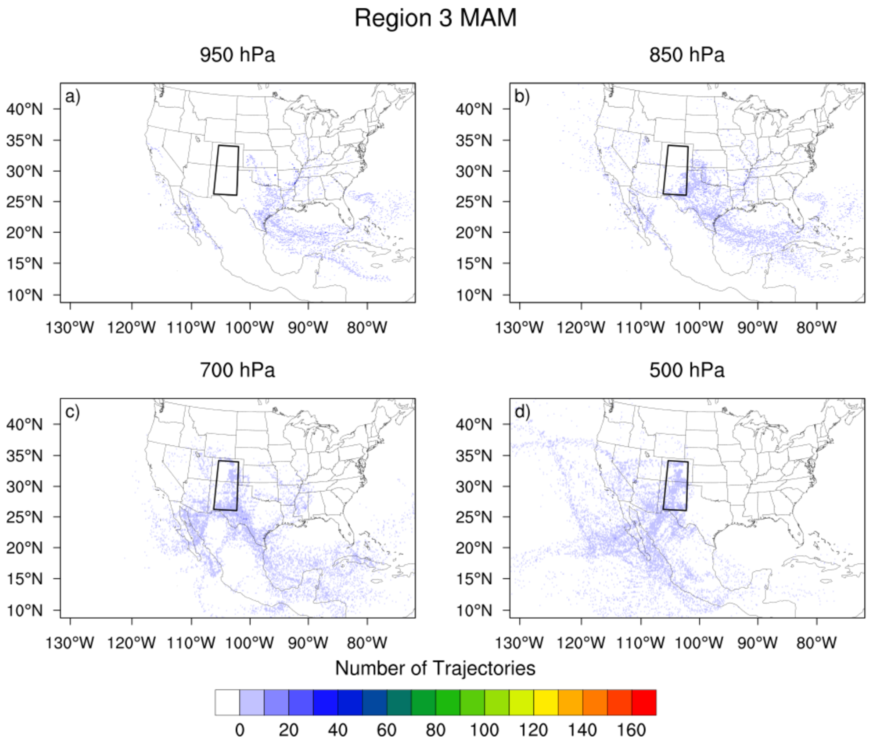

Figure A6. As in Figure A1, but for Region 3 (Front Range) during MAM.

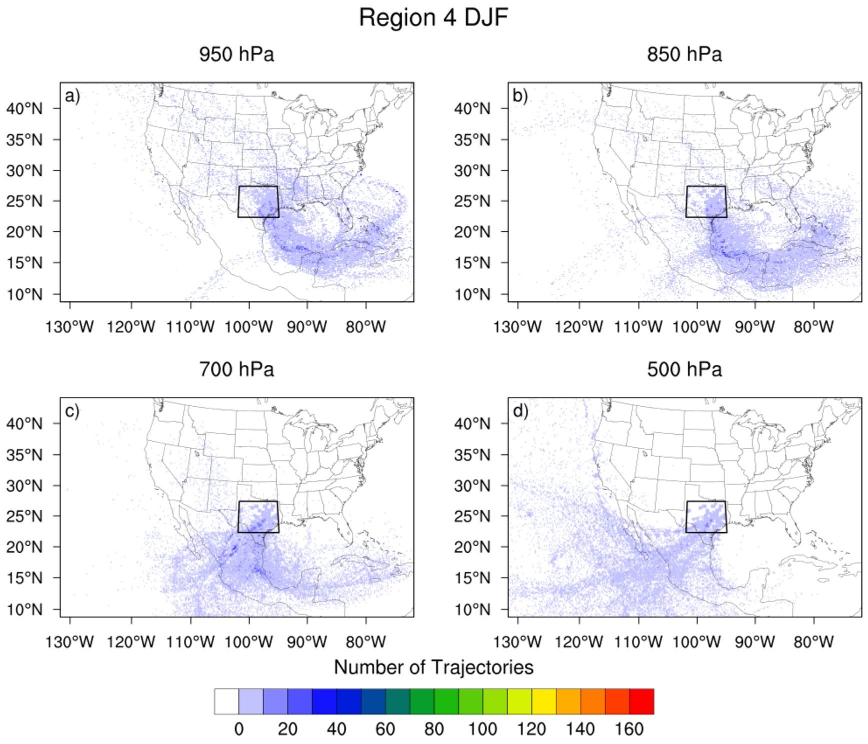

Figure A7. As in Figure A1, but for Region 4 (Flash Flood Alley) during DJF.

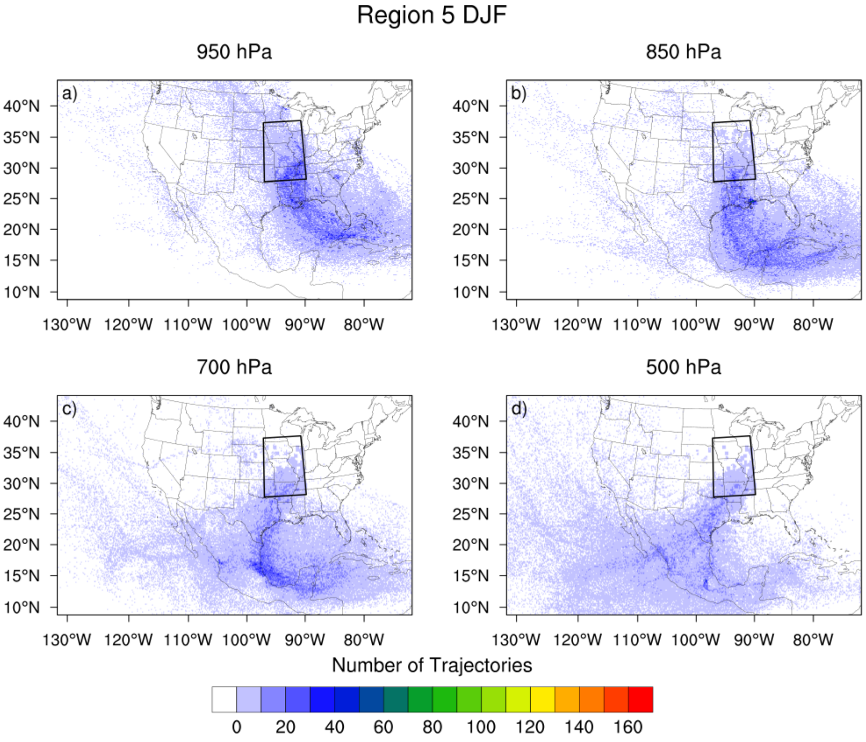

Figure A8. As in Figure A1, but for Region 5 (Missouri Valley) during DJF.

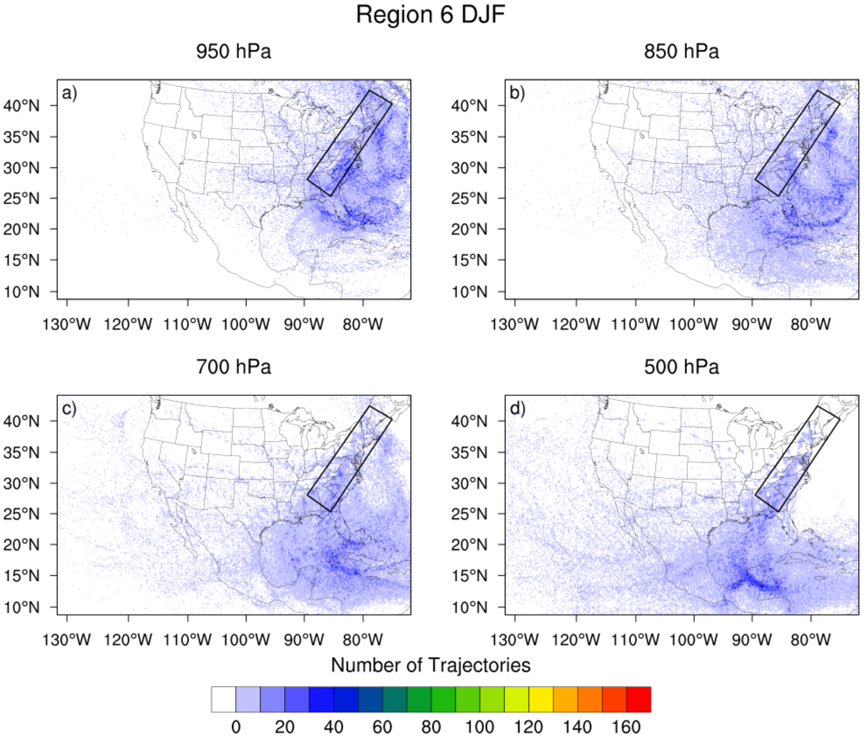

Figure A9. As in Figure A1, but for Region 6 (Appalachians) during DJF.

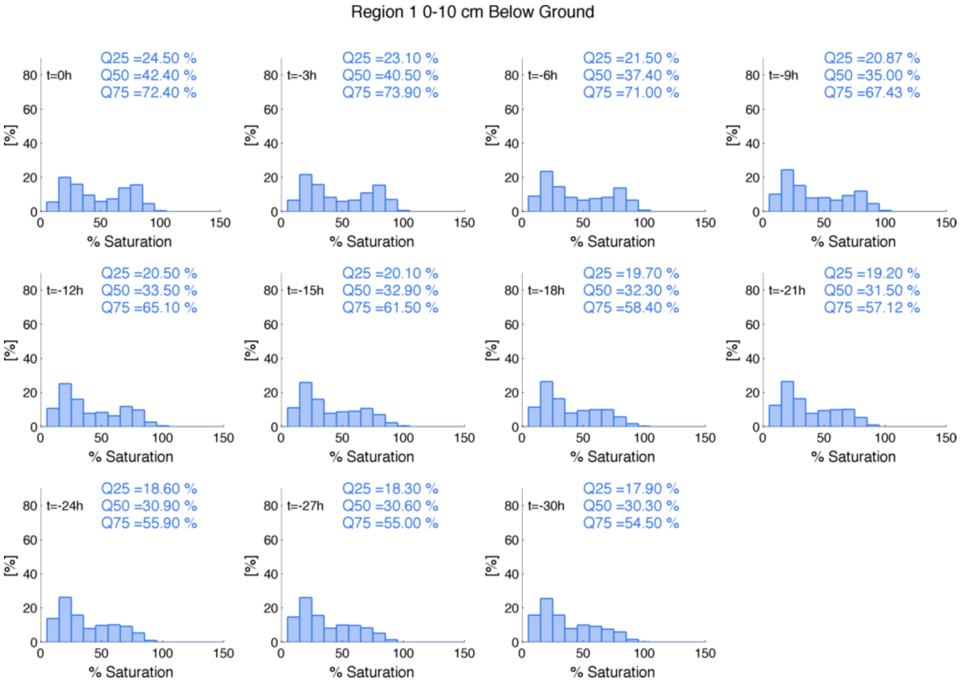

Figure A10. Local soil moisture (saturation) for Region 1 (West Coast) at 3-hour intervals prior to flood time.

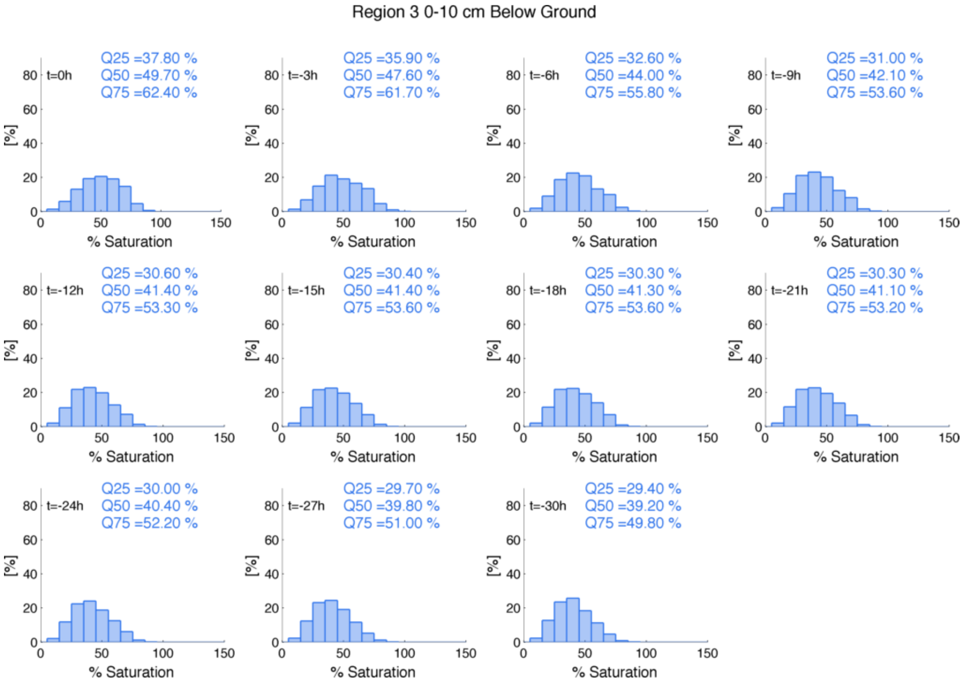

Figure A11. As in Figure A10, but for Region 3 (Front Range).

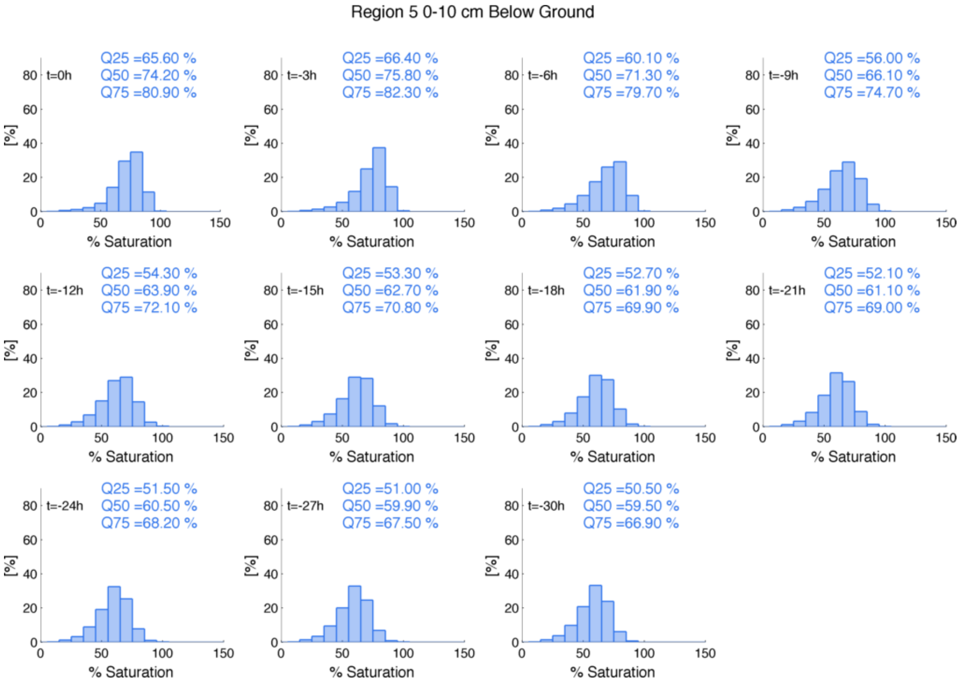

Figure A12. As in Figure A10, but for Region 5 (Missouri Valley).

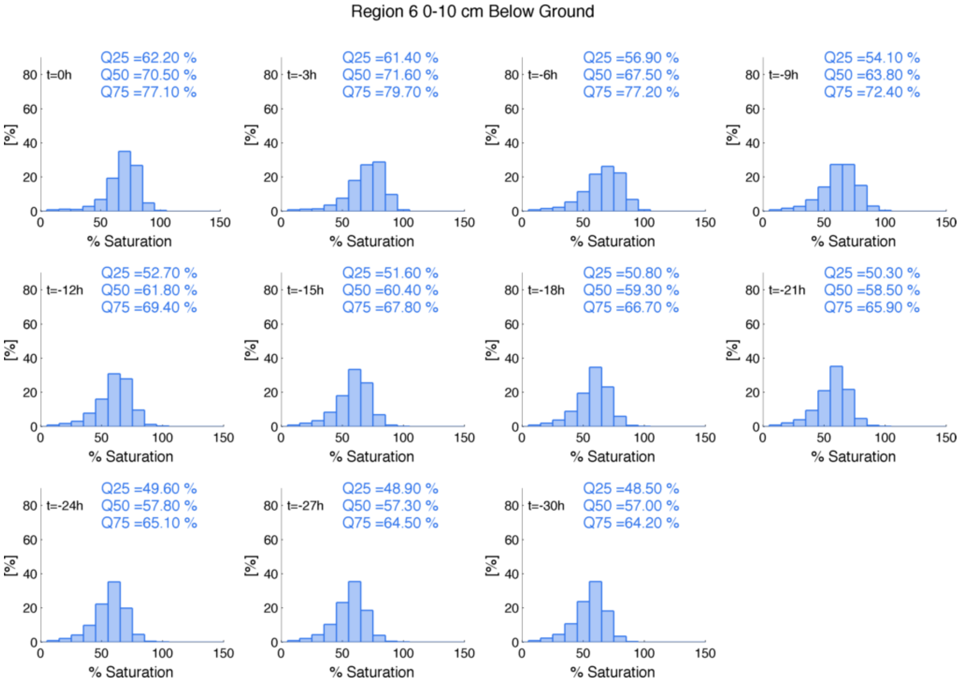

Figure A13. As in Figure A10, but for Region 6 (Appalachians).

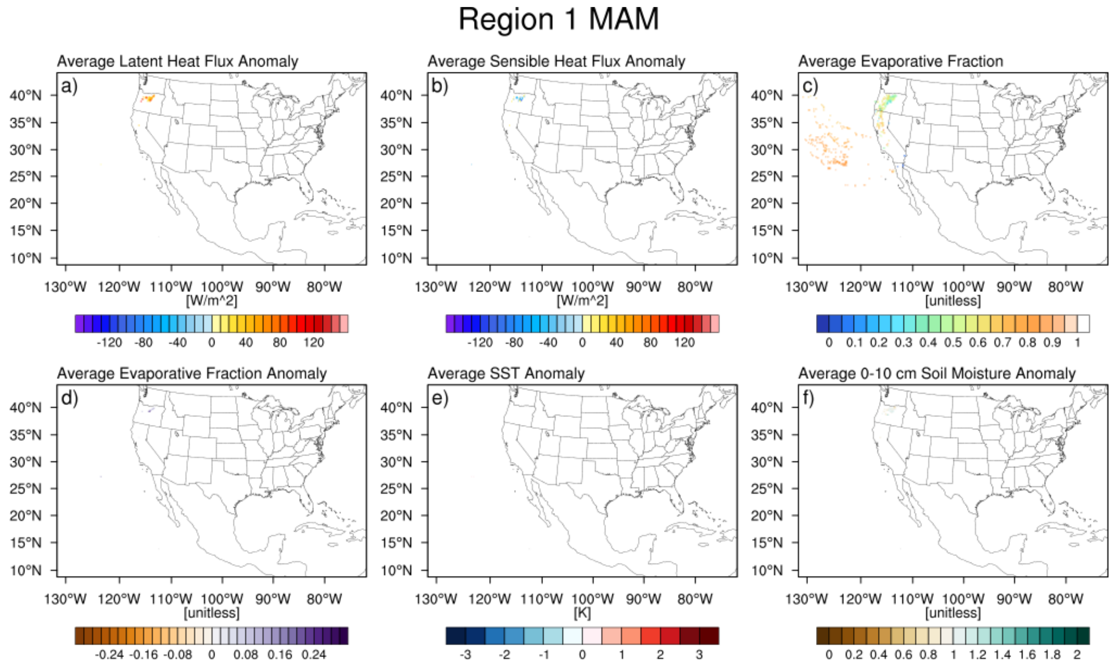

Figure A14. Average a) latent heat flux anomalies [Wm^{-2}] b) sensible heat flux anomalies [Wm^{-2}] c) evaporative fraction d) evaporative fraction anomalies e) SST anomalies and f) top layer (0-10 cm below ground) soil moisture anomalies for boundary layer uptakes for the West Coast (Region 1) in MAM.

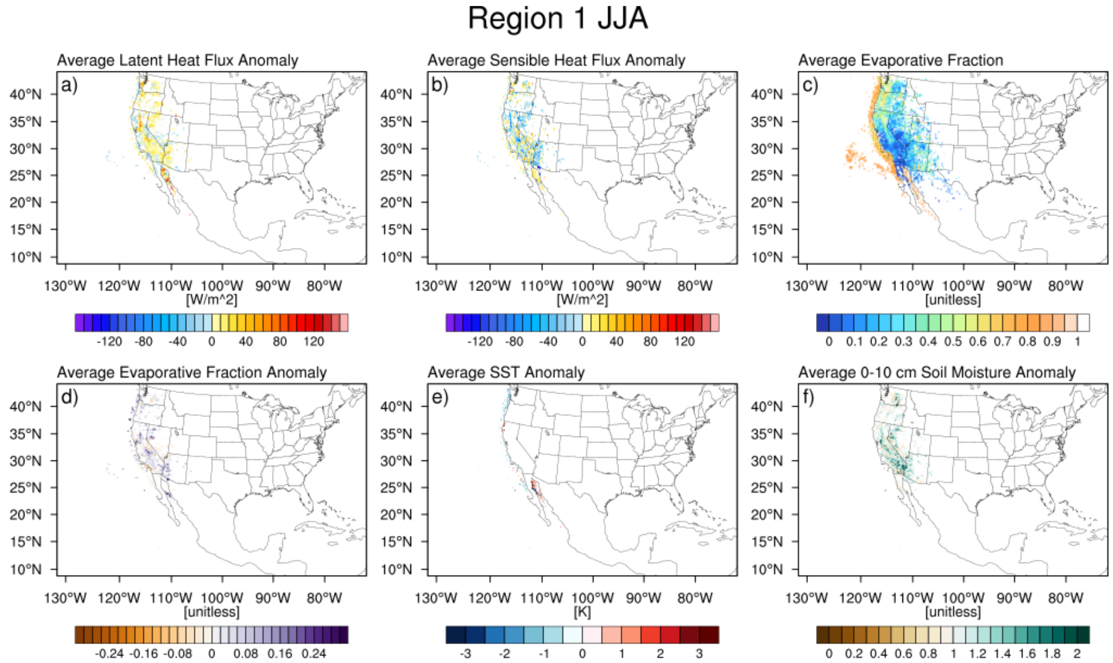

Figure A15. As in Figure A14, but for Region 1 during JJA.

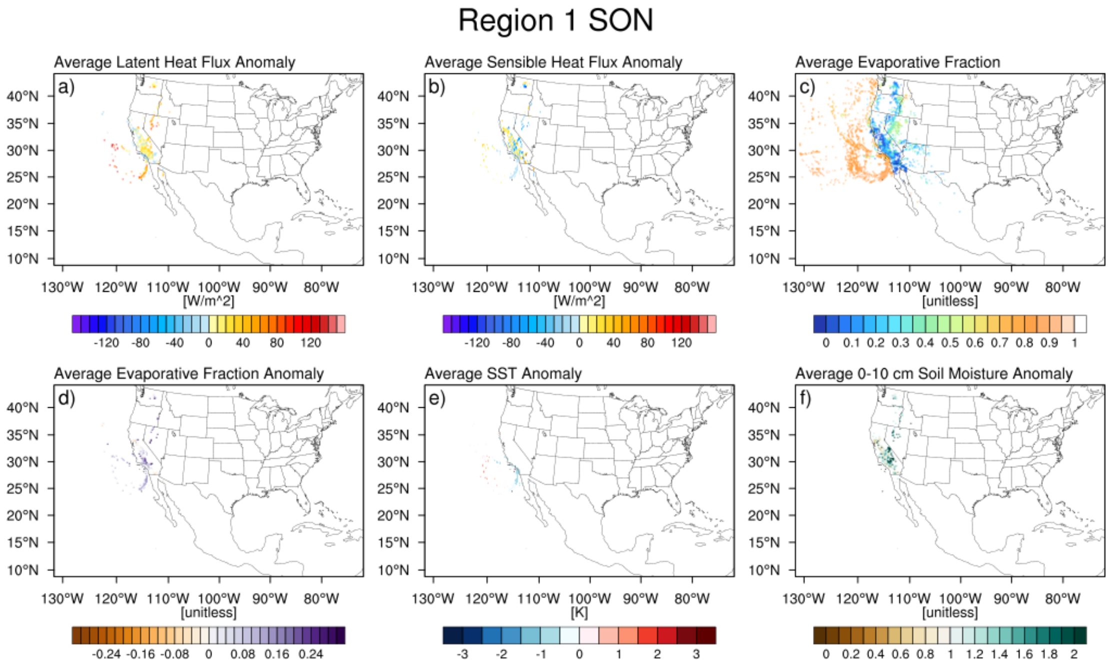

Figure A16. As in Figure A14, but for Region 1 during SON.

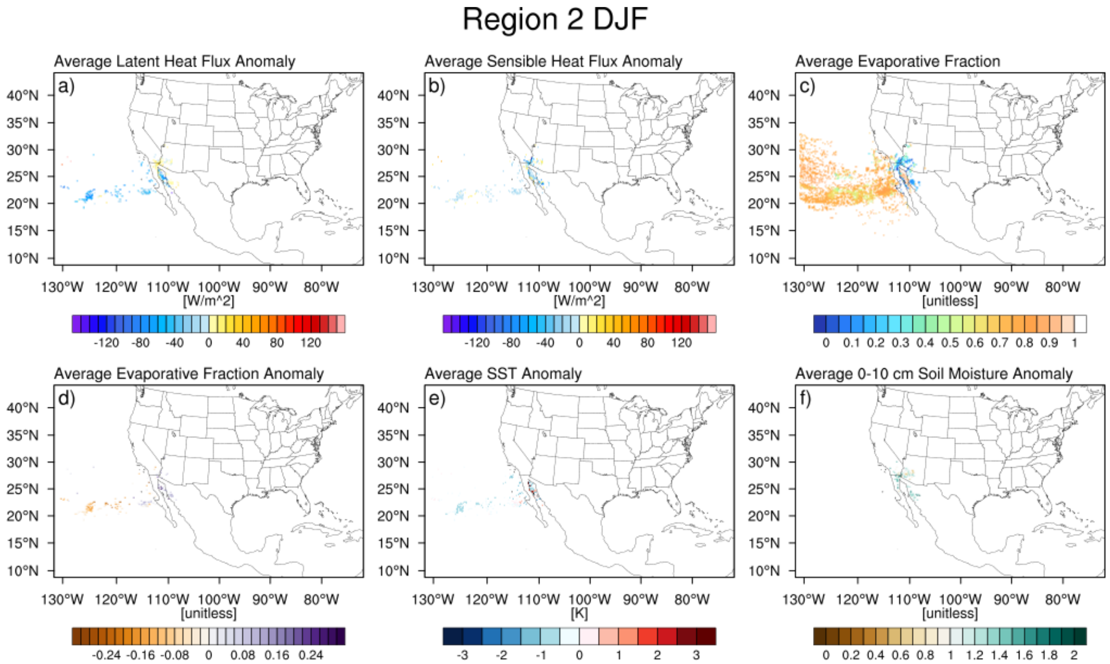

Figure A17. As in Figure A14, but for Region 2 (Arizona) during DJF.

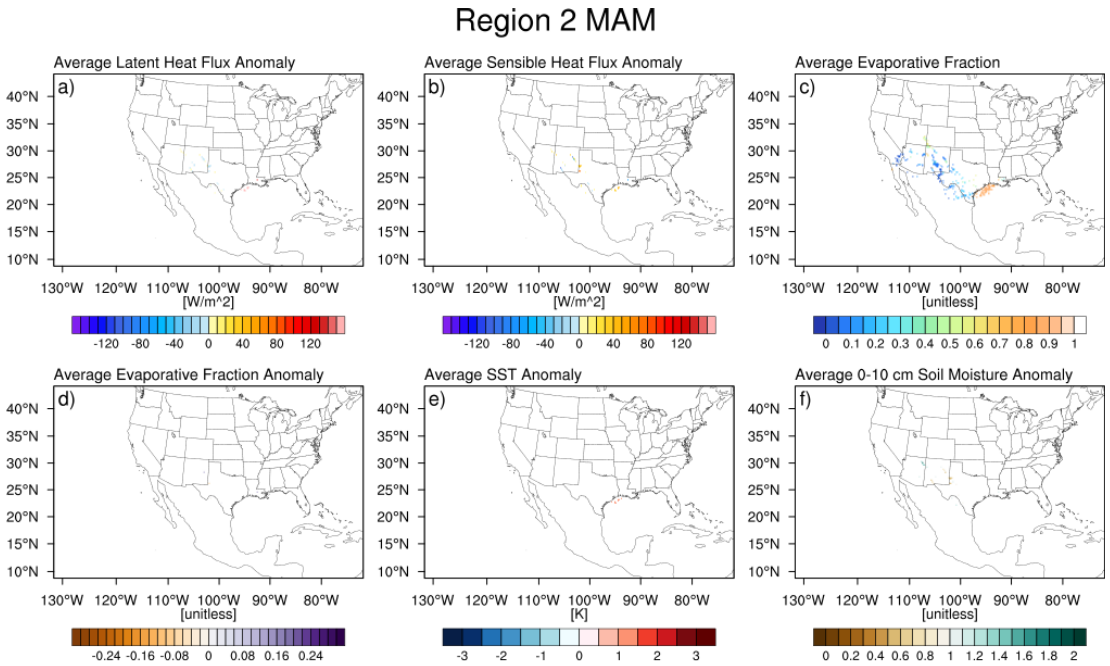

Figure A18. As in Figure A14, but for Region 2 during MAM.

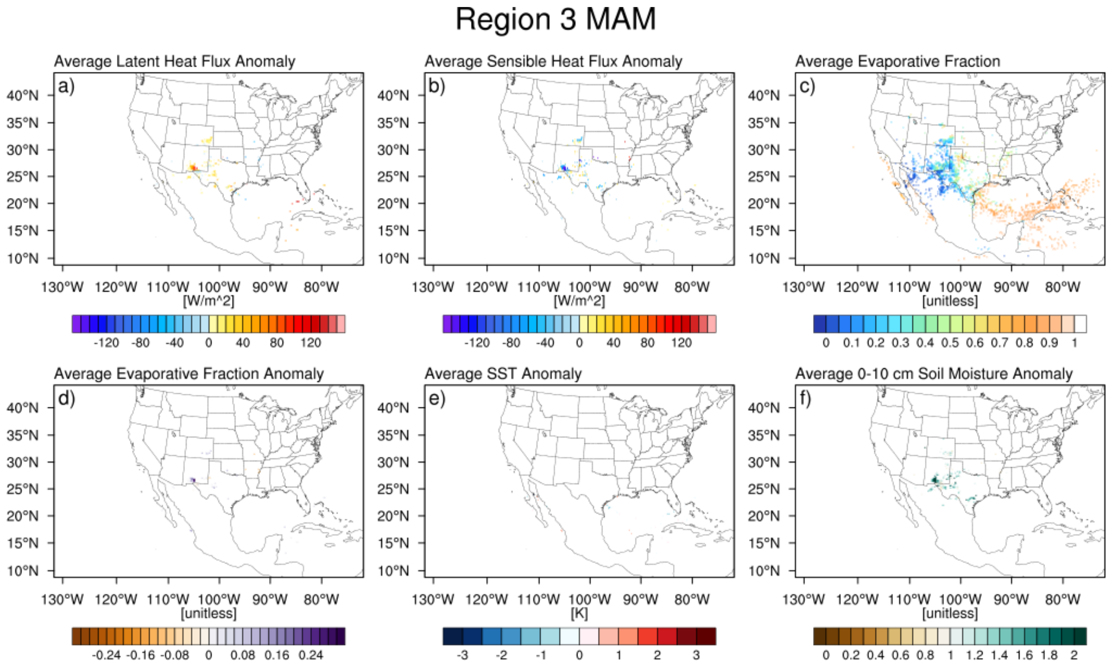

Figure A19. As in Figure A14, but for Region 3 during MAM.

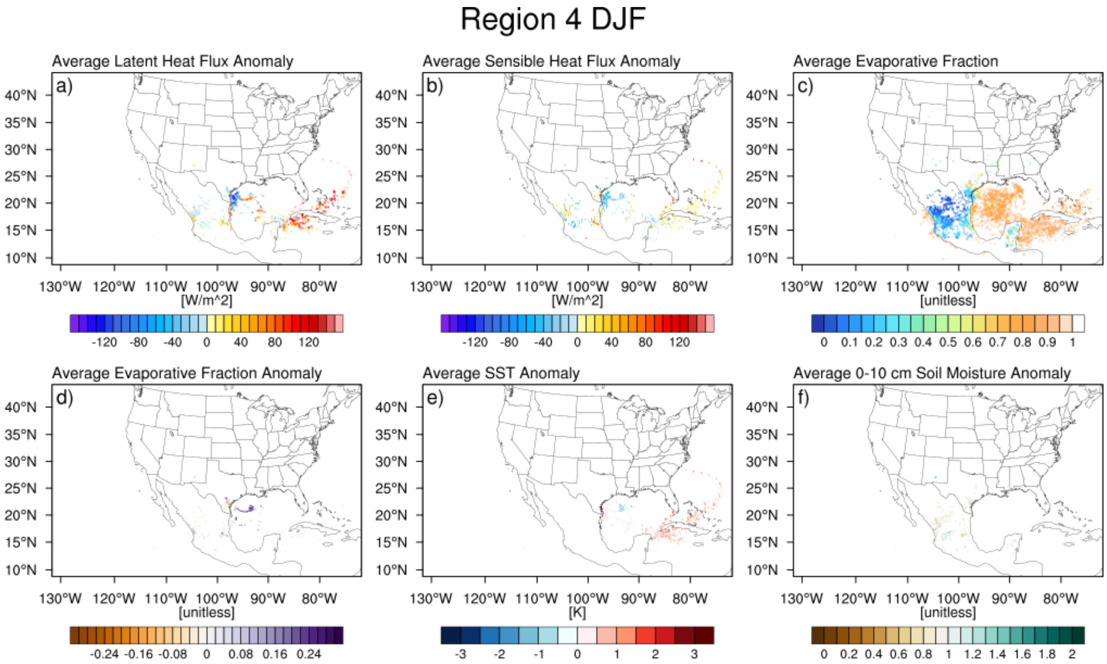

Figure A20. As in Figure A14, but for Region 4 (Flash Flood Alley) during DJF.

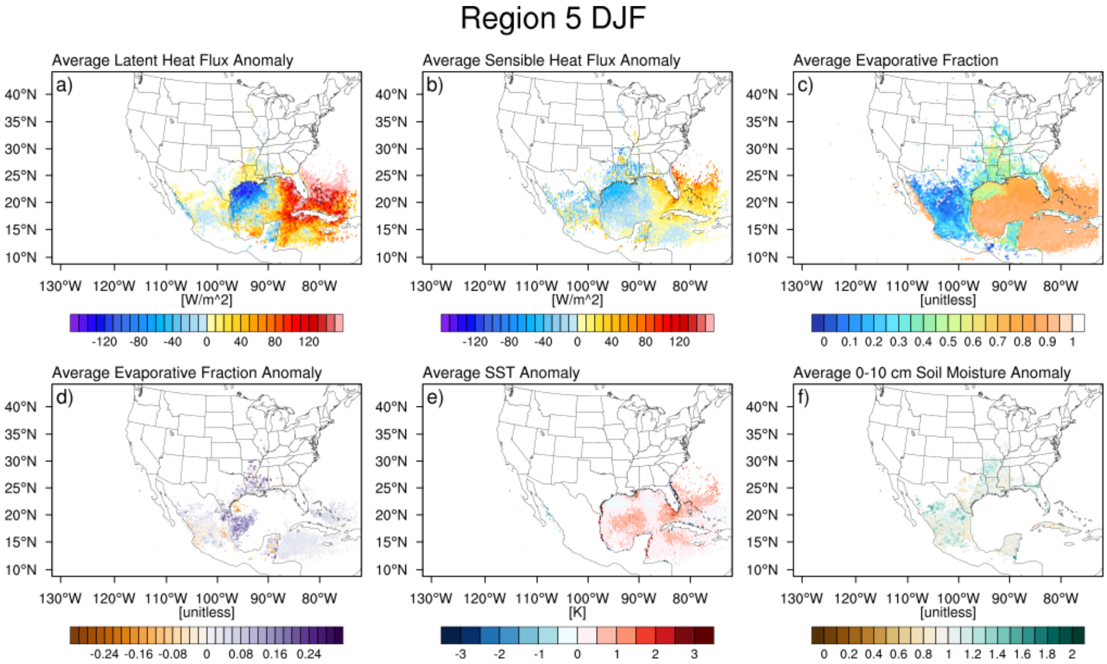

Figure A21. As in Figure A14, but for Region 5 (Missouri Valley) during DJF.

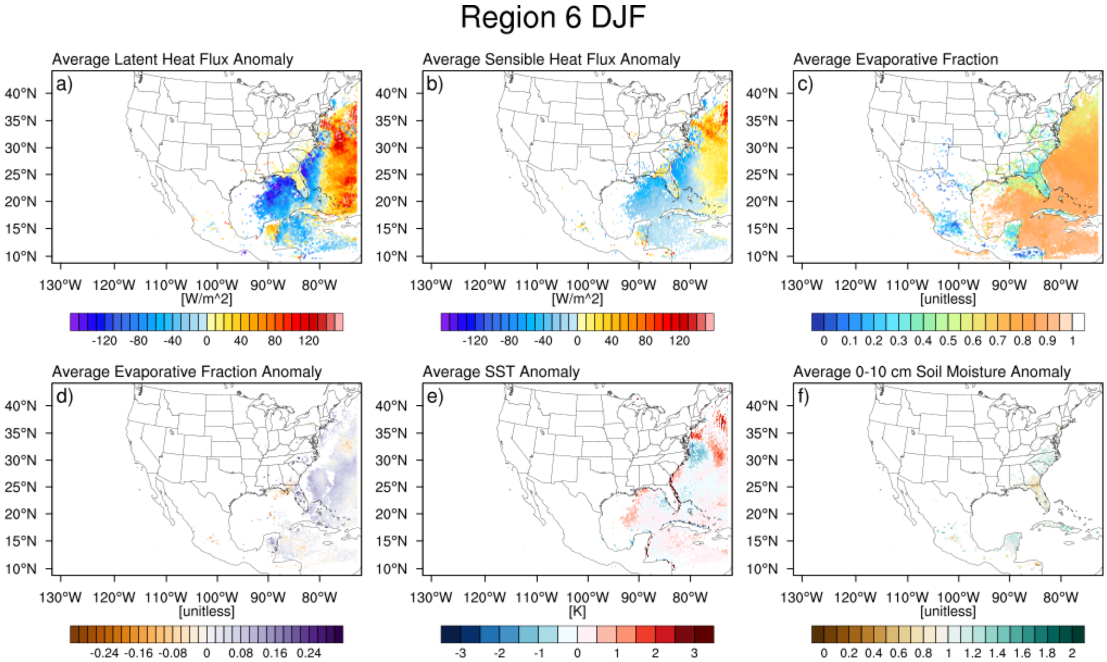

Figure A22. As in Figure A14, but for Region 6 (Appalachians) during DJF.